Exploring Optically Dark and Dim Gamma-Ray Bursts: Instrumentation, Observation and Analysis

by

Melissa C. Nysewander

A dissertation submitted to the faculty of the University of North Carolina at Chapel Hill in partial fulfillment of the requirements for the degree of Doctor of Philosophy in the Department of Physics & Astronomy.

Chapel Hill

2006

Approved by:

Dr. Daniel Reichart, Advisor
Dr. Wayne Christiansen, Reader
Dr. J. Christopher Clemens, Reader
Dr. Charles Evans, Reader
Dr. Jim Rose, Reader

ABSTRACT

MELISSA C. NYSEWANDER: Exploring Optically Dark and Dim Gamma-Ray Bursts: Instrumentation, Observation and Analysis
(Under the Direction of Dr. Daniel Reichart)

For the past decade, after the first afterglows of gamma-ray bursts (GRBs) were observed, astronomers have puzzled over the question of why some bursts have bright optical afterglows, while others have no detected emission at all, despite quick, deep searches. The source of the darkness can reveal specific clues to the nature of the progenitor and its local environment, or hint at global information pertaining to star-formation rates or the early universe itself, for example. Astronomers have identified possible causes of dark afterglows: (1) the burst lies at high redshift, (2) the burst is extinguished by dust in the host galaxy, (3) the burst occurred in a low-density region, or (4) the intrinsic light from the burst is dim due to microphysical parameters of the shock.

We present a two-pronged approach to understand the nature of *dark* and *dim* bursts. First, we detail the results of a large observing campaign designed to seek out and observe the optical and near-infrared afterglows of gamma-ray bursts in order to establish which are dark or dim. Secondly, we present PROMPT (Panchromatic Robotic Optical Monitoring and Polarimetry Telescopes), whose unique design allows it to identify afterglows that are highly reddened due to redshift and dust. PROMPT responds automatically to satellite notification, only tens of seconds after a GRB occurs, and can observe afterglows when they are at their brightest to discover dim afterglows that may have been missed with observations at later time. As proof of concept, I present a first look at the success of PROMPT's first year of operations and the eight rapid-time responses it made.

CONTENTS

LIST OF TABLES

LIST OF FIGURES

Chapter 1

Introduction

1.1 A Short History of Gamma-Ray Bursts

After being discovered in 1969 by a US military satellite designed to detect bright flashes of γ-ray emission coming from nuclear testing by the Soviet Union (Klebesadel et al. 1973), γ-ray bursts (GRBs) remained an enigma for nearly three decades. The only information astronomers had about GRBs were from the very short time scale (0.1 – 100 seconds) high-energy radiation (15 – 300 keV). Numerous theories were introduced to explain them, from the very large and distant, i.e. the collapse of supermassive bodies in the cores of quasars (Prilutskii & Usov 1975), to the very small and nearby, i.e. colliding comets (White 1993). Few clues to the true nature of the progenitors of gamma-ray bursts could be gleaned from the original data, so theorists could fit any number of physical models. At one point, in 1994, it was noted that there were in fact more theories about the explanation of gamma-ray bursts than there had been detected gamma-ray bursts themselves (Nemiroff 1994).

In 1991, NASA's *Compton Gamma-Ray Observatory* (*CGRO*) was launched and with it went the Burst and Transient Source Experiment (BATSE), which was designed to observe and localize the rapid flashes of high-energy emission from gamma-ray bursts. In its nine years of service, BATSE recorded informa-

tion from over 2700 gamma-ray bursts (Pačiesas 2004), which was a large enough sample for astronomers to make conclusions about the nature of GRBs. First, it was found that the bursts are divided into two populations based on their duration and peak energy (Kouveliotou et al. 1993). One population has durations of approximately 0.1 to 2 seconds, with high energy *hard* peaks, while the other has longer durations of 2 to 100 seconds with lower energy *soft* emission. These two populations are thus aptly named "short/hard" and "long/soft". The second important piece of information that BATSE discovered is that GRBs are distributed isotropically across the sky (Meegan et al. 1992; Briggs et al. 1996). This indicates that the observed phenomena come from a spherical distribution of progenitors, and to the surprise of many, did not match the distribution of any known Galactic populations. The most likely cause of the isotropy is that the bursts are originating at cosmic distances (Mao & Paczynski 1992), but the observations did not rule out closer populations. If the bursts were originating at cosmic distances, this would imply GRBs to be the most energetic explosions ever observed, which, for some, made this hypothesis unlikely. Astronomers explored other spherical distributions as the hosts of GRBs such as the Galactic halo (Brainerd 1992), the local stellar neighborhood (Hartmann et al. 1995) or the Kuiper Belt (White 1993).

During the 1990's, observers attempted to follow up the BATSE GRB localizations with ground-based optical, near-infrared and radio observations, but because of large error boxes and a long lag in distribution time, no afterglow emission was ever observed. This changed with the launch of the Dutch-Italian *BeppoSax* x-ray satellite, which included an instrument designed to detect gamma-ray bursts and produce localizations to 5 arcminutes. On February 28^{th}, 1997, *BeppoSax* observed the gamma-ray burst GRB 970228. The x-ray telescope on the satellite observed the field eight hours after the burst and found a rapidly fading afterglow (Costa et al. 1997). Coordinates of the afterglow were quickly disseminated to a Dutch observing team that discovered the first optical after-

glow of a GRB at 21 hours after the burst (van Paradijs et al. 1997). A search at radio wavelengths yielded no detections between 1 and 300 days after the burst (Frail et al. 1998). Astronomers excitedly jumped on the data to test various models of the emission mechanism, but a much larger breakthrough came on May 8^{th} 1997, when *BeppoSax* localized GRB 970508. An optical afterglow was found four hours after the trigger, and astronomers with the Keck Telescope measured a redshift of z = 0.835 ± 0.001 (Metzger et al. 1997; Djorgovski et al. 1997), which unequivocally placed the long/soft population of gamma-ray bursts at cosmological distances.

1.2 Long-Duration GRB Progenitors

Now theorists had strong data on which to base models of the progenitor and mechanism causing the bright, energetic emission. Gamma-ray bursts at cosmological distances meant extremely high-energy phenomena. The first to predict this was Paczynski (1986) who explored the idea that gamma-ray bursts are produced by supernovae-like progenitors at cosmological distances. The initial clues linking GRBs to supernovae were in the light curves of GRB 980325 (Bloom et al. 1999) and GRB 970228 (Reichart 1999). In both afterglows, red bumps arose after a few weeks and were best described as emission arising from core-collapse supernovae. GRB 980425 was a unique, under-luminous and nearby (z = 0.0085) burst, and no afterglow was discovered, but two weeks after the GRB, a bright Type Ic supernova arose in the *BeppoSax* error circle (Galama et al. 1998). The confirmation of the GRB-SN connection came in the spectrum of the bright GRB 030329, which although was found nearly two hours after the trigger, was still at 13^{th} magnitude. The unparalleled brightness allowed for precise photometry and high-resolution spectroscopy of the afterglow for weeks after the burst. This spectroscopy confirmed the relation by revealing a clear Type Ic SN, similar to GRB 980425, that slowly outshone the GRB afterglow (Stanek et al.

2003; Hjorth et al. 2003). Note that the supernova model only applies to the long/soft GRB population, the short/hard GRBs are likely due to the merger of compact binaries.

This GRB-SN connection confirmed the *collapsar* model, proposed by Woosley (1993) (see also Woosley et al. 2001). In this model, a high mass star (35-40 $M_{\odot}$; Fryer 1999) collapses to form a black hole, and in the process, creates the GRB. A rapidly rotating accretion disk is formed at the center of the star, which is composed of the infall of stellar material. The shock that would normally explode the star in a typical core-collapse supernova only partly occurs, and the black hole begins to rapidly accrete matter from the disk at about 0.001 - 0.1 $M_{\odot}$ s^{-1}. Two jets, either hydrodynamic or magnetically driven, emerge from the star's rotational poles at extreme relativistic velocities ($\Gamma \sim 100$) to produce shocks which emit the GRB and afterglow. The jet produces lateral shock waves which create the observed peculiar Type Ic supernova light curve and spectrum observed in GRB afterglows. There are a number of uncertainties in the progenitor properties – including metallicity, rotation, mass loss, and convection – hence only a fraction of high-mass stars end with a GRB.

1.3 The Standard Model

Meszaros & Rees (1993) explored emission mechanisms of cosmological GRBs, and presented the "fireball model," which is now commonly accepted as the standard model. In this model, the burst of high-energy γ-rays is produced by the relativistic fireball shocking from material in the interior of the star. The afterglow, composed of synchrotron radiation, is produced when the fireball then impacts upon the external medium. Because the afterglow forms as a result of this impact, its behavior is highly dependent on the local environment. Meszaros & Rees (1993) suggested that the fireball is formed as a result of the coalescence of compact binaries, but this is the model now widely accepted as the explana-

tion for short/hard GRBs (Gehrels et al. 2005; Hjorth et al. 2005; Berger et al. 2005c; Barthelmy et al. 2005), not long/soft core-collapse SN-driven bursts. The physics driving the emission mechanism are universal though - they apply to both the compact merger and the massive stellar collapse. The fireball model has found success in predicting the general broad-band spectra and light curves of afterglows.

Sari et al. (1998) calculated afterglow temporal and spectral properties within the framework of the "standard model," which allows observers to easily compare observations to the theory. The calculations are based upon a power-law distribution of electrons of index p, which are cut off at a low frequency, and produce synchrotron radiation in a relativistic shock expanding into a constant density medium. They solve the shock conditions for both the fully radiative and adiabatic cases, and present light curves and spectra of a model afterglow. The spectrum of the afterglow can be described as a series of power-law segments joined at specific frequencies: (1) ν_m, the synchrotron frequency corresponding to the minimum of the electron power-law distribution, (2) ν_c, the frequency above which the timescale of cooling is roughly equal to that of the dynamical timescale of the system, and (3) ν_a, the frequency below which self-absorption is important (Katz 1994; Waxman 1997; Katz & Piran 1997). Chevalier & Li (2000) reproduce this work for the case of the shock expanding into a wind-swept environment ($\rho \propto R^{-2}$). Because the progenitors of long-duration gamma-ray bursts are massive stars, we expect the conditions to be described by the wind-swept environment in which they live, although their immediate surroundings may in reality have more complex structure. Granot & Sari (2002) give a complete, detailed description of the temporal behavior of these spectral breaks and their dependence on environmental parameters for both cases (see also Panaitescu & Kumar 2000).

Soon after afterglows were first observed, evidence for jets were found from breaks in their light curves, the first of which was GRB 980519 (Halpern et al.

1999). Theorists had expected GRB emission to be collimated, but no evidence of this had yet been seen. After a GRB jet slows down and begins to spread laterally, a break in the light curve is expected, after which the slope will steepen dramatically: in the case of GRB 980519, $\alpha = -2.05 \pm 0.04$. Sari et al. (1999) determined the post-break relations between α, β and p within the framework of the standard model. The basic behavior of the temporal [F(t) $\propto t^{\alpha}$] and spectral [F(ν) $\propto \nu^{\beta}$] slopes are given in Table 1.1 for all three cases: ISM, wind-swept and post-jet break. Here we have defined the slopes as being inherently negative, i.e. a typical afterglow temporal slope is defined as being $\alpha \approx -1.0$.

Table 1.1: Temporal and Spectral Indices of GRB Afterglows

	$\nu_c < \nu$		$\nu_c > \nu$	
Environment	α	β	α	β
ISM (ρ = constant)	-(3p - 2)/4	-p/2	-3(p - 1)/4	-(p - 1)/2
Wind ($\rho \propto R^{-2}$)	-(3p - 2)/4	-p/2	-(3p - 1)/4	-(p - 1)/2
Post-Jet Break	-p	-p/2	-p	-(p - 1)/2

α, $\beta := F(\nu, t) \propto \nu^{\beta} t^{\alpha}$ (Sari et al. 1998; Chevalier & Li 2000).

1.4 Optically Dark Gamma-Ray Bursts

Although there were many successful detections of optical afterglows, there were, however, many notable non-detections. These bursts without an optical afterglow are commonly called *dark* gamma-ray bursts. These bursts do not follow the predicted behavior of the standard model, instead, the observed optical brightnesses vary over a wide range of magnitudes. Nevertheless, most early GRBs did not have detected optical afterglows because observers did not image quickly or deeply enough. In the very early days, error boxes were large, and the small angular coverage of large-aperture telescopes did not allow many to efficiently chase afterglows. Answering the question of whether or not the non-

detection of an afterglow is significant is difficult with small sample sizes, but there were clear early examples of dark gamma-ray bursts.

Examples

GRB 970828 was the first burst for which observers were genuinely puzzled over the lack of a detectable optical afterglow. No emission was found despite deep, quick searches down to a magnitude of $R \approx 24.5$ (Odewahn et al. 1997; Groot et al. 1998a). An x-ray afterglow was found using ROSAT, and Djorgovski et al. (2001) discovered a radio flare within the tight $10''$ x-ray localization that was determined to be related to the GRB. This localized the progenitor to a host galaxy at a redshift of z = 0.9578. The second clearly dark burst was GRB 000210, which was localized to $1''$ by the discovery of a fading x-ray afterglow. Observers searched down to $R \approx 23.5$ for an optical afterglow, but only found a stable host galaxy with redshift of z = 0.842 (Piro et al. 2002). Even among today's standards both limits are impressively quick and deep. Both cases for darkness are strengthened by the clearly fading x-ray afterglow and discovery of a host galaxy. These were not merely cases of a lack of efficiency in observations.

1.4.1 Causes of Optical Suppression

1. High Redshift

If the host of a gamma-ray burst lies at high redshift, then the Lyman α forest will be shifted beyond optical wavelengths. Emission from sources beyond a redshift of 5 – 6 will not be detected by most optical cameras. Neither of the two canonical dark bursts, GRB 970828 nor GRB 000210, had redshifts that would interfere with the R-band optical limits, but afterglows are commonly detected out to redshifts of 3 – 4, and have been detected out past a redshift of 6 (GRB 050904: §4). Any reported limit must take into account the effect of redshift; hence red optical limits are inherently more constraining than blue

ones. Only through near-infrared observations are the highest redshift GRBs discovered (see §4). Figure 1.1 gives the current redshift distribution of all long-duration cosmological gamma-ray bursts.

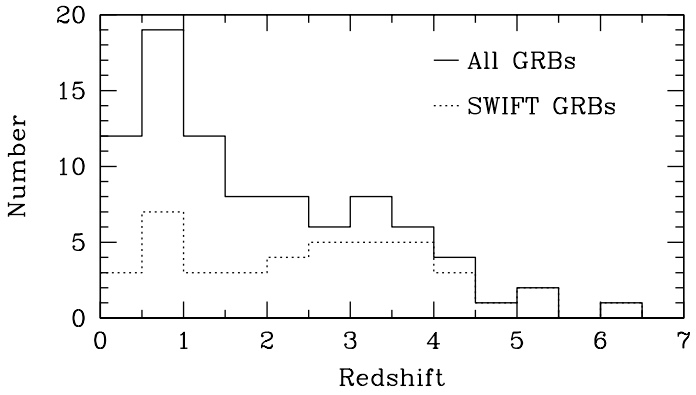

Figure 1.1: The total and post-*Swift* redshift distribution of long-duration GRBs. Questionable redshifts are not included. Figure is current as of September 21^{st} 2006.

2. Extinction

Extinction from circumburst dust in the host galaxy is thought to be a major contributor to the optical darkness of some gamma-ray bursts. Groot et al. (1998a) first proposed this scenario to explain the lack of an afterglow of the canonical dark burst, GRB 970828. Taylor et al. (1998) cited this as a possibility for the lack of optical emission from GRB 980329 because of the implications of the behavior of its millimeter and radio afterglow. GRBs are produced by the deaths of the highest mass stars, and because of their short lifetime, their

demise should occur in the same high-density molecular clouds in which they were conceived. X-ray measurements of N_H have supported this scenario and found values typical of giant molecular clouds (Galama & Wijers 2001; Reichart & Price 2002; De Pasquale et al. 2003; Stratta et al. 2004).

Dust absorbs blue light preferentially, which causes a curved shape to be imposed on the underlying power-law synchrotron spectrum. Because of this, it is important to obtain observations in less obscured near-infrared filters to serve as an *anchor* to determine the host extinction. This phenomenon is continuous: some bursts have very little extinction, while others have moderate amounts (GRB 030115 & GRB 050408: §3), and still others may suffer from extreme extinction (GRB 060306 & GRB 051022: §5). The continuum is not only a natural result of the filling factor and the geometry of the source within the molecular cloud, but also depends on how the dust is destroyed by the energy of the jet (Waxman & Draine 2000; Fruchter et al. 2001; Perna et al. 2003).

3. Low Density Environment

A high-density environment can cause a lack of optical afterglow through extinction, but a low-density can also produce a dark GRB. From the standard model we understand that internal shocks produce the high-energy γ-ray emission, but the afterglow is a result of external shocks produced from the interaction of the jet with its environment. In a low density environment we expect a very rapid decay of the afterglow, along with a dim initial flash ($F_m \propto \sqrt{n_o}$). From observations of the radio afterglow that imply that $\alpha_{opt} < -2.0$, Taylor et al. (2000) find this to be the most likely scenario for the darkness of GRB 990506. Similarly, although GRB 980326 was not dark, it had a very steep temporal slope of $\alpha = -2.10 \pm 0.13$, which was attributed to the low energy associated with a low density environment (Groot et al. 1998b).

4. Intrinsic Physics of Outflow

GRB 021024 (Berger et al. 2002) faded rapidly with $\alpha = -1.60 \pm 0.04$, which contributed to the *dimness*, but the main cause of its low optical emission was due to the intrinsic faintness of the afterglow. For this burst, no large extinction was needed to model the spectrum, nor was any redshift effect seen. The moderately steep slope would imply a lower density environment, but also, this burst showed that there is a diversity of intrinsic afterglow brightnesses. Fynbo et al. (2001) come to a similar conclusion for the very faint burst GRB 000630, that bursts vary with a wide range of intrinsic brightnesses. Granot & Sari (2002) discuss the various microphysical parameters that are inherent to the progenitor: the index of the electron energy distribution, p, the fraction of energy in electrons, ϵ_e, and the fraction of energy in the magnetic field, ϵ_B, and the large-scale isotropic equivalent total energy of the burst, E_{52}, and opening angle, Θ. These parameters, along with the density, n_o, or density profile, A_o, in a constant or wind-swept environment, govern the total fluxes and behavior of the synchrotron afterglow spectrum. Changing any of these parameters may cause an inherently lower afterglow flux (see GRB 021211: §2).

1.4.2 Statistical Implications

Reichart & Yost (2001), Reichart (2001a) and Reichart & Price (2002) find in general that the population of bursts without detected optical afterglows is indeed dimmer than the detected afterglow population and that all dark GRBs were not merely missed due to a lack of observation, but more likely due to absorption in the circumburst medium. Lazzati et al. (2002a) find a similar statistical conclusion, but deduce that there may be an intrinsic difference between the dark and bright burst population beyond the effects of extinction. From observations of the dim GRB 000630, Fynbo et al. (2001) find that 75% of GRB afterglows are consistent with those of this burst and suggest that the popula-

tion of afterglows is merely fainter than expected. From studies of the *BeppoSax* x-ray afterglows, De Pasquale et al. (2003) also find that the fraction of dark bursts is likely no more than 25%, and that most GRBs are simply faint. Lamb et al. (2004) find that 93% of GRBs localized by *HETE-2*'s SXC camera have optical afterglows, although this likely has as much to do with the selection bias of bright bursts as it does the tight, rapidly disseminated localizations.

Swift, the newest satellite launched to detect GRBs, is helping astronomers understand the confusion of the early studies. *Swift* has a detection rate and precision unparalleled by previous missions; it detects a burst on average twice a week, and it able to report positions to arcsecond accuracy, usually only seconds after a burst. Also, with higher sensitivity, it can detect fainter GRBs. The early sample of afterglows probed the brightest of bursts; the true population of afterglows was fainter still. With *Swift*, approximately 32% of all GRB afterglows have no detected optical component; this can be compared to 65% in the *BeppoSax* population of bursts with detected x-ray afterglows (Berger et al. 2005b). The *Swift* R magnitudes for detected bursts are on average two magnitudes fainter than the previous sample.

1.4.3 Defining *Dark*

Since the late 1990's in early days of GRB follow up, the number and quality of afterglow follow-up observations has improved greatly. The average response time for a GRB now is on the order of minutes instead of days, and the medium and large-aperture telescopes astronomers use are able to reach very deep limiting magnitudes. What was once considered deep, constraining limits are now commonplace. A significant fraction of afterglows have rapid-time follow-up to catch early emission, and less and less are being missed as dark.

There is no simple way to define a dark gamma-ray burst. Each GRB has a unique fluence, unique properties and follow-up efforts are diverse. If, though, there is a detected x-ray afterglow, as is the case with most recent GRBs due

to *Swift*'s X-Ray Telescope (XRT), then we can relate the optical to x-ray flux to create a definition. Jakobsson et al. (2004) have proposed a logical, quick way to define a dark GRB that relies on the assumption of the detection of an x-ray afterglow: the optical to x-ray spectral slope is greater than -0.5. Theories suggest and observations confirm that the most common values for the electron index, p, are greater than 2. Using Table 1.1, we see that for values of $p > 2$, $\beta < -0.5$. Hence, if the slope is greater than -0.5, there is extra suppression in the optical portion of the spectrum. β of -0.5 is a conservative estimate for this index; p generally ranges from 2.0 to 2.5. This also does not take into account the possible presence of the cooling break ν_c between the optical and x-ray.

Using this definition and the sample of events up to that time (July 2004), Jakobsson et al. (2004) find only 5 bursts that they are able to define as dark: GRB 970828, GRB 990506, GRB 990704, GRB 001025A, and GRB 001109. Rol et al. (2005) use a similar measure of spectral slope, but carefully fit a blast-wave model to each individual afterglow. In a smaller sample, they find that GRB 970828, GRB 000210 and 001025A should be considered dark bursts, but disagree with the Jakobsson et al. (2004) classification of GRB 990704 and GRB 001109 as dark. They also find that GRB 020322 and GRB 030115 (see §3.2) have suppressed optical emission and could be considered dark, even though they have detected afterglows. This reinforced the idea that dark and bright bursts form a continuum of afterglow brightnesses, and that we ought to also expect *dim* bursts as well.

Figure 1.2 presents the full sample of long-duration gamma-ray bursts with unambiguously detected and reported x-ray afterglows. Clearly, the *Swift* sample includes many more dark bursts than in the previous population that can be attributed to the success of *Swift* and the greater follow-up efficiency of the GRB community. The fluxes are measured in the optical R filter and at 3 keV. R is the most common filter used for measuring GRB afterglows, and is insensitive to redshift to approximately $z \approx 5$. 3 keV is mostly insensitive to absorption

(Jakobsson et al. 2004). This table is merely a quick diagnostic; to scale the data to a common time and frequency, we made assumptions about the typical optical temporal slope for each afterglow ($\alpha = -1.0$) and typical spectral index ($\beta = -0.6$) for when deeper limiting observations were cited in a filter other than R. These assumptions are not true for every case, so any bursts that show evidence of being dark or dimmed should be studied individually to confirm their nature.

Using this diagnostic, from the beginning of *Swift* operations to October 1^{st}, 2006, 111 *Swift* GRBs match the criteria. Of these, 29 have $\beta > -0.5$, which yields a lower limit on the dark burst fraction of 26%. Out of these 29 bursts, 4 limits have been derived from *White*, unfiltered UVOT observations that is unlikely to detect bursts at z $>$ 4 due to the quantum efficiency of the CCD. Fifteen of the dark bursts can be considered *dim*, as they have detected optical afterglows.

In order to understand the causes of the truly dark bursts, we must study the bursts along this continuum: those bursts that are dimmed beyond the prediction of the standard model. Here we present the results of large observing campaigns designed to seek out long-duration dark and dim gamma-ray bursts. The work presented here is the product of FUN GRB Collaboration and UNC's own resources. In Chapter 2, I describe GRB 021211, which appears to be intrinsically faint due to a combination of factors, the most significant of which are a low fraction of energy in relativistic electrons and a low circumburst density. Two bursts that are dim due to extinction, GRB 030115 and GRB 050408, are discussed in Chapter 3. In Chapter 4, I detail the discovery and determination of the photometric redshift of the high-z dark burst GRB 050904. GRB 051022 and GRB 060306 are two "truly dark bursts" that are discussed in Chapter 5. The exact cause of their darkness is unknown, but I explore the possibility that they are dark due to extinction. In Chapter 6, I discuss PROMPT (the Panchromatic Robotic Optical Monitoring and Polarimetry Telescopes), which

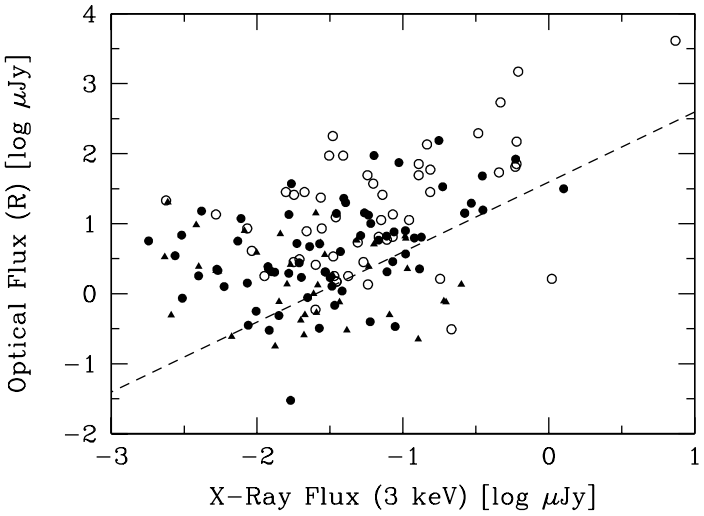

Figure 1.2: The optical and x-ray afterglow flux transformed to 11 hours after the burst. The dashed line indicates an x-ray to optical slope of -0.5. Bursts that fall below this line are defined as dark bursts. Open circles are taken from the pre-*Swift* sample of Jakobsson et al. (2004), closed circles are detections and triangles are upper limits taken in part from the early *Swift* analysis of Berger et al. (2005b), but mostly are gathered from the GCN archive.

was designed specifically to produce multi-color light curves of the early afterglows of gamma-ray bursts in order to rapidly find those that are faint due to extinction or high-redshift, as well as produce other science. In Chapter 7, I present a first look at the successes of PROMPT over a year of operations and the eight early-time afterglows it has chased.

Chapter 2

The Faintness of the Afterglow of GRB 021211

2.1 Introduction

The Follow-Up Network for Gamma-Ray Bursts (FUN GRB) Collaboration observed the optical afterglow of GRB 021211 made between 143 seconds and 102 days after the burst. Our unique data set includes the earliest filtered detections and color information for an afterglow in the pre-*Swift* era. We find that the afterglow is best described by (1) propagation through a wind-swept medium, (2) a cooling break that is blueward of the observed optical frequencies, and (3) a hard electron energy distribution. We constrain physical parameters that describe the afterglow and surrounding medium for a variety of scenarios and find that GRB 021211's afterglow is faint for a combination of 3 – 4 reasons: (1) a low fraction of energy in relativistic electrons, (2) a low density for the wind-swept medium, implying either a low mass-loss rate and/or a high wind velocity for the progenitor, (3) a wide opening/viewing angle for the jet, and possibly (4) moderate source-frame extinction. The jet appears to be significantly far from equipartition and magnetically dominated. More extreme versions of this might explain the darkness of many afterglows in the *Swift* era.

Observationally, GRB 021211 distinguishes itself in two ways: (1) It is the second GRB for which an optical afterglow was observed within minutes of the burst, thanks to rapid responses by the *HETE-2* satellite (Crew et al. 2002, 2003) and three robotic telescopes – RAPTOR (Wozniak et al. 2002), KAIT (Li et al. 2002, 2003), and Super-LOTIS (Park et al. 2002, this paper); and (2) It is the first GRB for which filtered detections (beginning 143 seconds after the burst) and color information (beginning 38 minutes after the burst) were obtained at early times.

In addition to observations presented in GRB Coordinates Network (GCN) Circulars, many groups have presented their observations in peer-reviewed journals: Li et al. (2003) present an unfiltered light curve beginning 105 seconds after the burst; Fox et al. (2003a) present an unfiltered light curve beginning 21 minutes after the burst and filtered optical, NIR, and radio observations beginning 2.0 hours after the burst; Pandey et al. (2003) present filtered optical observations beginning 6.8 hours after the burst; Holland et al. (2004) present filtered optical and NIR observations of both the afterglow and host galaxy beginning 17 hours after the burst and measure the spectral flux distribution of the afterglow around 21 hours after the burst; and Smith et al. (2005b) present submillimeter observations around 25 hours and 10 days after the burst. Finally, Della Valle et al. (2003) present photometric and spectral evidence for an associated supernova at late times.

As in the case of GRB 990123 (Akerlof et al. 1999), the optical afterglow faded more rapidly at first, presumably due to a reverse shock (Wei 2003; Fox et al. 2003a; Li et al. 2003; Holland et al. 2004). However, these afterglows differ in that GRB 021211 was 3 – 4 mag fainter, despite a lower redshift [$z = 1.004$ for GRB 021211 (Vreeswijk et al. 2003; Della Valle et al. 2003) vs. $z = 1.600$ for GRB 990123 (Hjorth et al. 1999)] (Fox et al. 2003a; Li et al. 2003; Pandey et al. 2003; Crew et al. 2003). If it were not for the rapid response of the GRB community, GRB 021211 might have been called a "dark burst": It faded from

$R \approx 14$ mag at ≈90 sec after the burst (Wozniak et al. 2002) to $R > 21$ mag about three hours later. Many bursts that would have been called "dark" in the *BeppoSAX* era are being and will be called "dim" in the *HETE-2*, *Integral*, and *Swift* era due to faster responses.

Some authors have modeled GRB 021211 with an emphasis on its environment. Kumar & Panaitescu (2003) argue that the GRB and afterglow were produced by the same shock and within this framework constrain physical parameters for both constant-density and wind-swept media. Panaitescu & Kumar (2004) consider the early-time afterglows of both GRB 021211 and GRB 990123 in the context of reverse-forward shock (for both constant-density and wind-swept media) and wind-bubble scenarios and find that the reverse-forward shock scenario is preferred. Chevalier et al. (2004) argue for a wind-swept medium with the cooling break redward of the R band and within this framework find wind densities that are low compared to Galactic Wolf-Rayet stars (see also Panaitescu & Kumar 2004). Finally, Dado et al. (2003) model GRB 021211 within the framework of their cannonball model.

In §2.2, we present FUN GRB Collaboration observations of GRB 021211, which include the earliest filtered detections and color information for an afterglow in the pre-*Swift* era. In §2.3, we fit standard afterglow and extinction curve models to these and other groups' data to the "standard model". In §2.4, we compare our results to previous modeling results and constrain physical parameters that describe the afterglow and surrounding medium for a variety of scenarios and discuss why GRB 021211's afterglow is so faint. We draw conclusions in §2.5.

2.2 Observations

The long-duration, X-ray rich GRB 021211 was detected by *HETE-2*'s FREGATE, WXM, and SXC instruments on December 11, 2002 at 11:18:34 UT

(Crew et al. 2003). The initial satellite localization was 14 arcminutes in radius and reported only 22 seconds after the burst. Ground analysis of the WXM and SXC data, reported 131 minutes after the burst, improved the localization to 2 arcminutes in radius and was consistent with the initial localization.

Fox & Price (2002) announced the discovery of an $R \approx 18$ mag and fading, stationary point source in the error circle 53 minutes after the burst. While the pair labored, the robotic telescopes of three groups had already responded to the alert. For only the second time in the afterglow era, robotic telescopes extended the light curve of an afterglow back to within tens of seconds of the burst (Wozniak et al. 2002; Li et al. 2002, 2003; Park et al. 2002, this work).

The dim and quickly fading afterglow soon grew too faint for small telescopes, and a host galaxy was detected. VLT spectroscopy of the host measured a redshift of $z = 1.004 \pm 0.002$ (Vreeswijk et al. 2003; Valle et al. 2003). Late-time observations indicate both a re-brightening at the time expected for a supernova at $z \approx 1$, and a spectrum that resembles that of Type Ic SN 1994I (Fruchter et al. 2002; Della Valle et al. 2003).

FUN GRB Collaboration Observations

Table 1 summarizes the FUN GRB Collaboration observations of GRB 021211. We have calibrated all of our measurements using the field calibration of Henden (2002). Each set of observations was reduced using IRAF's CCDRED package and photometered using IRAF's DAOPHOT package.

Super-LOTIS imaged the entire GRB 021211 field in two sixty-second R band exposures beginning 143 and 309 seconds after the burst (Park et al. 2002). Observations began automatically after receiving the *HETE-2* alert via a socket connection to the GCN. The mean times listed in Table 1 are flux weighted using an iterated power-law index of $\alpha = -1.37$, since the exposure time is comparable to the age of the burst, at least for the first exposure. This results in small shifts of 2.4 and 1.2 seconds in the mean times of these observations.

The 0.81-meter Tenegra II telescope imaged the GRB 021211 field beginning 37 minutes after the burst. We obtained four sets of four images, each set in a 2×2 arrangement to cover the initial 28 arcminute-diameter localization and each in a different filter ($BVRI$). We then re-pointed to the candidate afterglow of Fox & Price (2002) and cycled through R & I thrice more. Of these, we combined the first two R and I images to optimize signal to noise, but the final two images were not usable due to the onset of morning. This resulted in three detections in VRI, a limit in B, and two more detections in R & I.

We imaged the central 11 arcminute $\times$ 11 arcminute of the initial 28 arcminute-diameter localization in R band beginning 85 minutes after the burst from Gunma Astronomical Observatory, located in Agatsuma, Gunma, Japan (Kinugasa et al. 2002). We obtained a total of 28 images, all of which we combined to optimize signal to noise.

We reacquired the field with the 1.34-meter diameter Tautenburg Schmidt telescope 11.7 hours after the burst and imaged in R and I bands for the next 1.1 hours (Klose et al. 2002), however, we did not detect the afterglow.

We began observations with the 3.5-meter diameter Astrophysics Research Consortium (ARC) telescope at Apache Point Observatory 22.0 hours after the burst, and returned to the field on December 28 and March 23, 17 and 102 days after the burst (Lamb et al. 2002a,b). Three i band 2000-second images were taken on the first night, and seven 1200-second images were taken on each of the following nights in the same filter.

Finally, we re-observed the field on December 13 with the 1.0-meter diameter telescope at the U.S. Naval Observatory's Flagstaff Station for purposes of calibration (Henden 2002). $BVRI$ images were taken with a 20 48 $\times$ 2048 back-illuminated SITe/Tektronix CCD under 2.2 arcsecond seeing conditions. Upon inspection of the images, the afterglow was still marginally visible in the 8-minute V-band image.

Table 2.1: FUN GRB Observations of the Afterglow of GRB 021211

Mean Time (UT)	Mean Δt	Filter	Magnitude	Source
Dec 11.4732[b]	2.84 min	R	15.24 $\pm$ 0.07	Super-LOTIS
Dec 11.4751[b]	5.63 min	R	16.26 $\pm$ 0.12	Super-LOTIS
Dec 11.4986	39.4 min	I_c	18.60 $\pm$ 0.11	Tenagra II
Dec 11.5114	57.9 min	R_c	19.52 $\pm$ 0.13	Tenagra II
Dec 11.5239	75.9 min	V	20.06 $\pm$ 0.41	Tenagra II
Dec 11.5366	94.1 min	B	>19.8	Tenagra II
Dec 11.5479	1.84 hr	I_c	19.99 $\pm$ 0.24	Tenagra II
Dec 11.5525	1.95 hr	R_c	20.74 $\pm$ 0.42	Tenagra II
Dec 11.5566	2.05 hr	R_c	20.70 $\pm$ 0.16	Gunma
Dec 11.9583	11.7 hr	R_c	>22.0	Tautenburg
Dec 11.9744	12.1 hr	I_c	>20.7	Tautenburg
Dec 12.3883	22.0 hr	i	23.02 $\pm$ 0.12	ARC
Dec 13.4680	47.9 hr	V	23.0 $\pm$ 0.5	USNO 1.0m
Dec 28.4283	17.0 day	i	24.41 $\pm$ 0.22	ARC
Mar 23.1335	102 day	i	24.51 $\pm$ 0.29	ARC

[a]Upper limits are 3σ. [b]Flux weighted using an iterated power-law index of $\alpha = -1.37$

2.3 Analysis

We fit the standard afterglow and extinction curve models to these and other groups' data and also explore show that within the first few hours after the burst the significance of one and possibly two chromatic variations which may be superimposed on this "standard model" behvaior. The data that we include in this analysis are plotted in Figure 2.1 and Figure 2.2 and consist of FUN GRB Collaboration data (§2.1), data previously published in peer-reviewed journals (Pandey et al. 2003; Fox et al. 2003a; Li et al. 2003; Holland et al. 2004), and data from the GCN archive (McLeod et al. 2002). These data span the first $\approx$2.5 days after the burst, after which the host galaxy and supernova become contaminants.

All magnitudes have been converted to spectral fluxes as prescribed by Bessell (1979) and Bessell & Brett (1988).

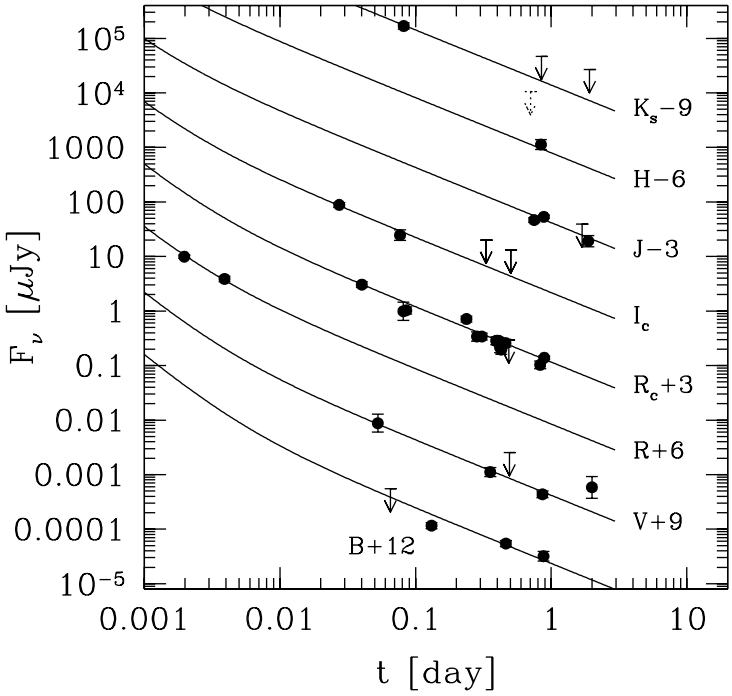

Figure 2.1: The $BVRIJHK_s$ light curves of GRB 021211 from 2.8 minutes to 2 days after the burst and the best-fit wind $\nu_c > \nu_{opt}$ fit. The dotted K_s upper limit is not included in the model.

To better investigate possible variations that occurred during the unfiltered KAIT and NEAT observations (see §3.2), we have recalibrated these measurements from the R band to broad bands given by the spectral responses of their respective CCDs (Pravdo et al. 1999; Li et al. 2003): W. Li (private communication) and P. Price (private communication) kindly provided us with their calibration stars. Using the BVRI magnitudes of these stars from Henden (2002), we fitted extinguished blackbody functions to each of these stars and then integrated these fitted functions against the appropriate spectral response curve. This resulted in small, 0.05 and 0.03 magnitude offsets in the calibration of the KAIT and NEAT measurements, respectively.

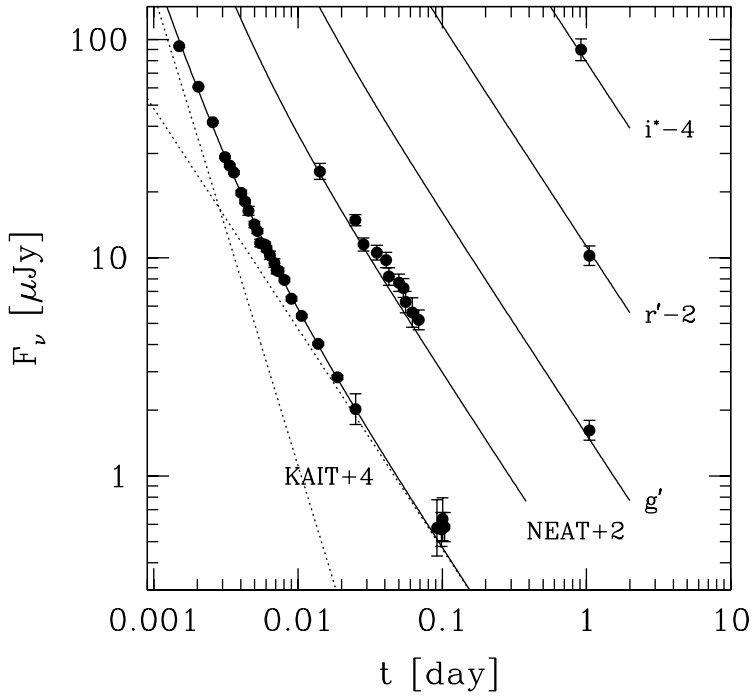

Figure 2.2: The *gri* and unfiltered light curves of GRB 021211 from 9.2 minutes to 1 day after the burst and the best fit wind $\nu_c > \nu_{opt}$ fit. The dotted lines are the separate reverse and forward shock components for the KAIT light curve.

Model

We now model these data and constrain model parameters. We model the afterglow with two components, corresponding to a reverse and forward shock. Each component has a power-law light curve and a power-law spectrum, and the spectrum is extinguished by dust in the source frame and in our Galaxy and absorbed by hydrogen in the source frame and the Lyα forest:

$$F_\nu(t) = e^{-\tau_\nu^{MW}} e^{-\tau_{\nu(1+z)}^{Ly\alpha}} e^{-\tau_{\nu(1+z)}^{source}} F_0 \left[\left(\frac{t}{t_0}\right)^{\alpha_{rs}} \left(\frac{\nu}{\nu_R}\right)^{\beta_{rs}} + \left(\frac{t}{t_0}\right)^{\alpha_{fs}} \left(\frac{\nu}{\nu_R}\right)^{\beta_{fs}} \right], \tag{2.1}$$

where τ_ν^{MW} is the Galactic extinction curve model of Cardelli et al. (1989), $\tau_{\nu(1+z)}^{Ly\alpha}$ is the Lyα forest absorption model of Reichart (2001a), $\tau_{\nu(1+z)}^{source}$ is the source-frame extinction curve and Lyman limit absorption model of Reichart (2001a), α_{rs} and

α_{fs} are the temporal indices of the two components, β_{rs} and β_{fs} are the spectral indices of the two components, ν_R is the effective frequency of the R band, t_0 is the time when these two components are of equal brightness at this frequency, and F_0 is thi s brightness. Since the extinction and absorption models have features that are narrower than most photometric bands, we integrate this equation against the appropriate filter transmissivity curve (or CCD spectral response curve for the unfiltered measurements) before fitting it to the data.

We fit this model to the data using Bayesian inference (e.g. Reichart 2001a; Lee et al. 2001; Galama et al. 2003): The posterior probability distribution is equal to the product of the prior probability distribution and the likelihood function. The likelihood function is given by:

$$\mathcal{L} = \prod_{i=1}^{N} \frac{1}{\sqrt{2\pi(\sigma_i^2 + \sigma^2)}} \exp\left\{-\frac{1}{2}\frac{[y(\nu_i, t_i) - y_i]^2}{\sigma_i^2 + \sigma^2}\right\}, \tag{2.2}$$

where N is the number of measurements, $y(\nu_i, t_i)$ is the above described integration of Equation 1 against the spectral curve of the ith measurement at the time of the ith measurement; y_i is the ith measurement in units of log spectral flux; σ_i is the uncertainty in the ith measurement in the sam e units, and σ is a parameter, sometimes called the slop parameter, that models the small systematic errors that are unavoidably introduced when data are collected from many sources, and other small sources of error (Reichart 2001a). Ignoring this parameter can lead to erroneous fits and significantly underestimated uncertainties in the fitted parameter values when the scatter of the measurements about the fitted model exceeds that which can be accounted for by the measurement uncertainties alone.

Many of the parameters of the source-frame extinction curve model and all of the parameters of the Lyα forest absorption and Galactic extinction curve models can be constrained a priori. The source-frame extinction curve model of Reichart (2001a) is a function of eight parameters: the source-frame V-band extinction magnitude A_V, $R_V = A_V/E(B-V)$, the intercept c_1 and s lope c_2 of

the linear component of the source-frame UV extinction curve, the strength c_3, width γ and center x_0 of the UV bump component of the extinction curve, and the strength c_4 of the FUV excess component of the extinction curve. The Lyα forest absorption model of Reichart (2001a) is a function of a single parameter, D_A, the flux deficit. Reichart (2001a) determines prior probability distributions for R_V, c_1, γ, x_0, and D_A, which me ans that the values of these parameters can be weighted by fairly narrow distributions, the description of which sometimes depends on other parameters (c_2 and z), a priori. We adopt these priors here, which can be thought of as increasing the degrees of freedom by five. Also, the Galactic extinction curve model of Cardelli et al. (1989) is a function of $E(\mathrm{B-V}) = 0.028$ mag for this line of sight (Schlegel et al. 1998) and a single parameter, R_V^{MW}. We adopt a prior for this parameter that is log normally distributed with mean $\log 3.1$ and width 0.1, which closely approximates the distribution of values of this parameter along random lines of sight through the Galaxy (e.g. Reichart 2001a; Lee et al. 2001; Galama et al. 2003).

Fits

We fit our model to the data for each of the four standard cases of Sari et al. (1998) and Chevalier & Li (2000), which relate α_{fs} t o β_{fs} assuming (1) propagation through either a constant-density (ISM) or wind-swept (WIND) medium, and (2) a cooling break that is either redward (RED) or blueward (BLUE) of the observed optical and NIR frequencies: For the ISM-RED and WIND-RED cases, $\alpha_{fs} = (3\beta_{fs} + 1)/2 = -(3p - 2)/4$; for the ISM-BLUE case, $\alpha_{fs} = 3\beta_{fs}/2 = -3(p - 1)/4$; and for the WIND-BLUE case, $\alpha_{fs} = (3\beta_{fs} - 1)/2 = -(3p - 1)/4$, where p is the power-law index of the electron-energy distribution. Since the temporal index is well constrained by the data, these additional constraints can be powerful tools for separating the intrinsic spectrum from extinction effects. For purposes of comparison, we also fit our model to the data free of constraints on α_{fs} and β_{fs}.

Best fits are found by maximizing the posterior. Compared to the WIND-BLUE case, we can rule out the ISM-RED and WIND-RED cases at the 7.3σ credible level, and the ISM-BLUE case is disfavored at the 3.1σ credible level. Furthermore, the WIND-BLUE fit is consistent with the constraint-free fit, differing from it at only the 0.6σ credible level. The primary difference between these cases is that the WIND-BLUE case requests a shallow intrinsic spectrum, $\beta_{fs} = -0.34^{+0.01}_{-0.01}$, and a small amount of extinction, $A_V = 0.18^{+0.25}_{-0.12}$ mag, where the other cases request steeper intrinsic spectra and would fit better if $A_V < 0$ mag were possible (see §4). For the WIND- BLUE case, we find that $\log F_0[\mu Jy] = 2.98^{+0.12}_{-0.12}$, $\log t_0[day] = -2.56^{+0.07}_{-0.07}$, $\alpha_{rs} = -2.16^{+0.09}_{-0.10}$, $\beta_{rs} = 1.1^{+0.7}_{-0.8}$, $\alpha_{fs} = -1.01^{+0.02}_{-0.01}$, $\beta_{fs} = -0.34^{+0.01}_{-0.01}$, $A_V = 0.18^{+0.25}_{-0.12}$ mag, $c_2 < 4.3$ (1σ), and $\sigma = 0.038^{+0.010}_{-0.008}$ mag. The parameters c_3 and c_4 could not be constrained by the data. We plot best-fit light curves for 13 spectral bands in Figure 2.1 and Figure 2.2 and best-fit spectral flux distributions for six epochs in Figure 2.3.

2.4 Discussion

Our finding that the data are best described by the WIND-BLUE case differs from the findings of others. Fox et al. (2003a) discount this case in favor of the ISM-BLUE case, arguing that if the early-time emission is due to a reverse shock, in a wind-swept medium it is expected to fade quickly and they measure a slower fading: $\alpha_{rs} = -1.63 \pm 0.13$. However, Chevalier et al. (2004) point out that this measurement depends sensitively on how one subtracts out (or models) the forward-shock component, arguing that the value is closer to $\alpha_{rs} = -2.2$. Using final instead of GCN data, we find that $\alpha_{rs} = -2.16^{+0.09}_{-0.10}$. However, we point out that emission from the reverse shock is not necessarily expected to fade quickly in a wind-swept medium if A_* and other physical parameters are lower than expected, which appears to be the case for this GRB.

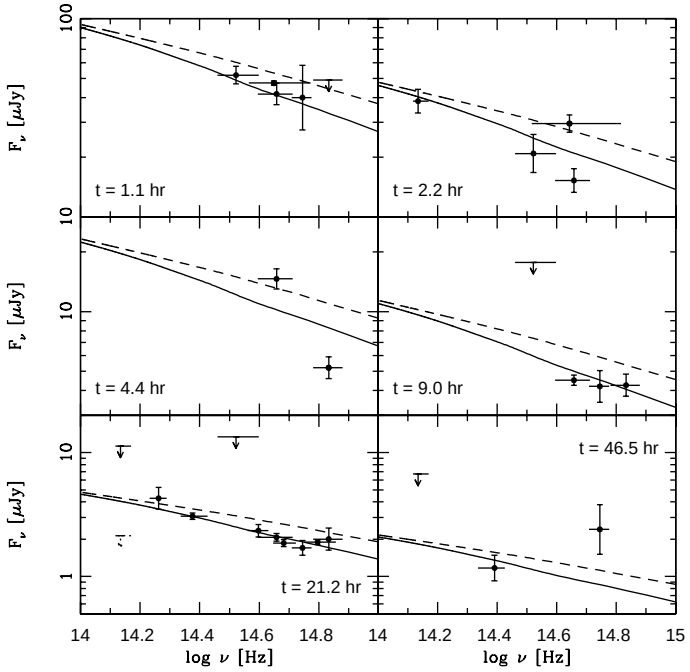

Figure 2.3: The spectral flux distribution of GRB 021211 at six epochs. Data were scaled using the best fit light curve presented in §2.3. The curves are the WIND-BLUE model both extinguished (solid line) and unextinguished (dashed line).

Holland et al. (2004) also adopt the ISM-BLUE case. The primary difference between their fit and ours is that we permit source-frame extinction. When we fit the ISM-BLUE case, we find that $\beta_{fs} = -0.67$ with $A_V = 0$ mag, which is very similar to their fit in a time slice around 0.88 days after the burst: $\beta_{fs} = -0.69 \pm 0.14$ with A_V assumed to be zero. However, if source-frame extinction is permitted and one fits to all of the data, we find that the WIND-BLUE case with a small to moderate amount of source-frame extinction, $A_V = 0.18^{+0.25}_{-0.12}$ mag is preferred at the 3.1σ credible level. Figure 4e can be directly compared to Figure 3 of Holland et al. (2004).

Finally, Chevalier et al. (2004) adopt the WIND-RED case, guided by sparse color information that was available at the time, including the two points of

Figure 4c, which we have already identified as discrepant, possibly due to excess red light at this time (§3.2). Permitting source-frame extinction and fitting to all of the data, we rule this case out at the 7.3σ credible level.

The WIND-BLUE case, however, requires a relatively hard electron energy distribution – $p = 1.68^{+0.01}_{-0.03}$ – so a break at higher energies is required. Bhattacharya (2001) determines the effect of $p < 2$ on the standard equations: By introducing a cut-off frequency γ_u such that $\gamma_m < \gamma_e < \gamma_u$ and assuming that γ_u evolves directly with the bulk Lorentz factor of the shock, they find results similar to the standard prescriptions. Galama et al. (2003) found a similar hard electron energy index for GRB 010222, though other ideas, such as a continuous injection of energy (Björnsson et al. 2002) or an early transition to non-relativistic motion (in't Zand et al. 2001; Masetti et al. 2001), have been proposed.

Physical Parameters

Following the analysis of Chevalier et al. (2004), but for the WIND-BLUE case, and using the analytic expressions of Granot & Sari (2002), we now constrain physical parameters that describe the afterglow and surrounding medium for a variety of scenarios. The first constraint comes from the expression of Granot & Sari (2002) for the brightness of the afterglow in the frequency range of our observations, which for the WIND-BLUE case is $\max\{\nu_{sa},\nu_m\} < \nu < \nu_c$, where ν_{sa} is the self-absorption frequency, ν_m is the typical synchrotron frequency, and ν_c is the electron cooling frequency. This corresponds to segment G in their Figure 1. For $p = 1.68$, a luminosity distance of $d_L = 2.06 \times 10^{28}$ cm (assuming that $\Omega_m = 0.3$, $\Omega_\Lambda = 0.7$, and $H_0 = 70$ km s^{-1} Mpc^{-1}), and an extinction-corrected $F_R = 19$ μJy at 0.1 days after the burst, we find:

$$\overline{\epsilon}_e^{0.68} \epsilon_B^{0.67} A_* E_{52}^{0.67} = 1.02 \times 10^{-5}, \tag{2.3}$$

where $\overline{\epsilon}_e$ is the electron energy fraction when $p < 2$, ϵ_B is the magnetic field energy fraction, A_* measures the density of the wind-swept medium, and $E = E_{52} \times 10^{52}$

erg is the total energy of the shock, if spherical. The second constraint comes from the expression of Granot & Sari (2002) for $\nu_c(t)$ and the fact that the data are well described by the WIND-BLUE case even at early times (see §4.3). Taking $\nu_c > \nu_R$ prior to 3.9 minutes after the burst – the time when the forward shock first outshines the reverse shock in the R band – yields:

$$\epsilon_B^{3/2} A_*^2 E_{52}^{-1/2} = 6.52 \times 10^{-6} \left(\frac{t_{c,R}}{3.9\,\mathrm{min}} \right)^{1/2}, \tag{2.4}$$

where $t_{c,R}$ is the time that ν_c passes above the R band. The third constraint is similar to the second in that we take $\nu_m < \nu_R$ prior to 3.9 minutes after the burst, else the light curve would have faded much more slowly at this time, as $F_\nu \approx t^{-1/4}$ citepcl00; clf04:

$$E_{52}^{1/2} \overline{\epsilon}_e^{-2} \epsilon_B^{1/2} = 1.18 \times 10^{-5} \left(\frac{t_{m,R}}{3.9\,\mathrm{min}} \right)^{3/2}, \tag{2.5}$$

where $t_{m,R}$ is the time that ν_m passes below the R band. The final constraint comes from the expression of citetgs02 for the brightness of the afterglow at 8.5 GHz, given that $F_{8.5} < 35$ μJy at a mean time of 13 days after the burst (Fox et al. 2003a). Here we consider four scenarios: (A) $\nu_{sa} < 8.5$ GHz $< \nu_m$, (B) 8.5 GHz $< \min\{\nu_{sa},\nu_m\}$, (C) $\max\{\nu_{sa},\nu_m\} < 8.5$ GHz, and (D) $\nu_m < 8.5$ GHz $< \nu_{sa}$.

For scenario A, using the expression of Granot & Sari (2002) that corresponds to their segment D, we find:

$$\overline{\epsilon}_e^{-2/3} \epsilon_B^{1/3} A_* E_{52}^{1/3} = 3.76 \times 10^{-2} \left(\frac{F_{8.5}}{35\,\mu\mathrm{Jy}} \right). \tag{2.6}$$

Combining Equations 3, 4, 5, and 6 yields:

$$\overline{\epsilon}_e = 6.53 \times 10^{-4} E_{52}^{-1} \left(\frac{t_{c,R}}{3.9\,\mathrm{min}} \right)^{-0.25} \left(\frac{t_{m,R}}{3.9\,\mathrm{min}} \right)^{0.24}, \tag{2.7}$$

$$\epsilon_B = 765 E_{52}^{3} \left(\frac{t_{c,R}}{3.9\,\mathrm{min}} \right) \left(\frac{t_{m,R}}{3.9\,\mathrm{min}} \right)^{2.04}, \tag{2.8}$$

$$A_* = 1.75 \times 10^{-5} E_{52}^{-2} \left(\frac{t_{c,R}}{3.9\,\mathrm{min}} \right)^{-0.5} \left(\frac{t_{m,R}}{3.9\,\mathrm{min}} \right)^{-1.53}, \tag{2.9}$$

$$F_{8.5} = 20 \left(\frac{t_{m,R}}{3.9\,\mathrm{min}} \right)^{-1.01} \mu\mathrm{Jy}. \tag{2.10}$$

If we additionally require that $\nu_{sa} < 8.5$ GHz $< \nu_m$ at 13 days after the burst, using the expressions of Granot & Sari (2002) for ν_{sa} and ν_m, we find that $F_{8.5} < 6$ μJy and $E_{52} > 3.50 \times 10^{-3} (F_{8.5}/35\,\mu\mathrm{Jy})^{1.38}$. Since the former of these constraints contradicts Equation 10 for any value of $t_{m,R} < 3.9$ min, we rule out this scenario.

For scenario B, using the expression of Granot & Sari (2002) that corresponds to their segment B, we find:

$$\overline{\epsilon}_e A_*^{-1} E_{52} = 1.70 \times 10^{-4} \left(\frac{F_{8.5}}{35\,\mu\mathrm{Jy}} \right). \tag{2.11}$$

Combining Equations 3, 4, 5, and 11 yields:

$$\overline{\epsilon}_e = 0.306 \left(\frac{t_{c,R}}{3.9\,\mathrm{min}} \right)^{-0.125} \left(\frac{t_{m,R}}{3.9\,\mathrm{min}} \right)^{1.125} \left(\frac{F_{8.5}}{35\,\mu\mathrm{Jy}} \right)^{-0.5}, \tag{2.12}$$

$$\epsilon_B = 7.45 \times 10^{-6} \left(\frac{t_{c,R}}{3.9\,\mathrm{min}} \right)^{0.625} \left(\frac{t_{m,R}}{3.9\,\mathrm{min}} \right)^{-0.615} \left(\frac{F_{8.5}}{35\,\mu\mathrm{Jy}} \right)^{1.5}, \tag{2.13}$$

$$A_* = 3.85 \left(\frac{t_{c,R}}{3.9\,\mathrm{min}} \right)^{-0.25} \left(\frac{t_{m,R}}{3.9\,\mathrm{min}} \right)^{0.24} \left(\frac{F_{8.5}}{35\,\mu\mathrm{Jy}} \right)^{-1}, \tag{2.14}$$

$$E_{52} = 2.14 \times 10^{-3} \left(\frac{t_{c,R}}{3.9\,\mathrm{min}} \right)^{-0.125} \left(\frac{t_{m,R}}{3.9\,\mathrm{min}} \right)^{-0.885} \left(\frac{F_{8.5}}{35\,\mu\mathrm{Jy}} \right)^{0.5}. \tag{2.15}$$

If we additionally require that 8.5 GHz $< \min\{\nu_{sa}, \nu_m\}$ at 13 days after the burst, we find that $t_{m,R} > 2.9$ min, which is technically consistent with $t_{m,R} < 3.9$ min, and $F_{8.5} > 27$ μJy, which is technically consistent with $F_{8.5} < 35$ μJy. However, this constrains these parameters' values to narrow ranges and by Equation 15 implies a value for E_{52} that is much too low, given that the isotropic-equivalent energy in gamma rays alone was $(1.0 \pm 0.1) \times 10^{52}$ erg (Holland et al. 2004) or $1.68^{+0.32}_{-0.27} \times 10^{52}$ erg (Lamb et al. 2004). Assuming that the efficiency at which energy is converted to gamma rays is $\sim$20% (e.g., Beloborodov 2000), then $E_{52} \approx$ many. Consequently, we rule out this scenario as well.

For scenario C, using the expression of Granot & Sari (2002) that corresponds to their segment G, we find:

$$\overline{\epsilon}_e^{0.68} \epsilon_B^{0.67} A_* E_{52}^{0.67} = 6.26 \times 10^{-5} \left(\frac{F_{8.5}}{35\,\mu\mathrm{Jy}} \right). \tag{2.16}$$

Combining Equations 3, 4, 5 and 16 yields:

$$\overline{\epsilon}_e = 6.53 \times 10^{-4} E_{52}^{-1} \left(\frac{t_{c,R}}{3.9\,\mathrm{min}} \right)^{-0.25} \left(\frac{t_{m,R}}{3.9\,\mathrm{min}} \right)^{0.24}, \tag{2.17}$$

$$\epsilon_B = 765 E_{52}^{3} \left(\frac{t_{c,R}}{3.9\,\mathrm{min}} \right) \left(\frac{t_{m,R}}{3.9\,\mathrm{min}} \right)^{2.04}, \tag{2.18}$$

$$A_* = 1.75 \times 10^{-5} E_{52}^{-2} \left(\frac{t_{c,R}}{3.9\,\mathrm{min}} \right)^{-0.5} \left(\frac{t_{m,R}}{3.9\,\mathrm{min}} \right)^{-1.53}, \tag{2.19}$$

$$F_{8.5} = 6\,\mu\mathrm{Jy}. \tag{2.20}$$

If we additionally require that $\max\{\nu_{sa},\nu_m\} < 8.5$ GHz at 13 daysafter the burst, we find that $t_{m,R} < 13$ minutes and $E_{52} > 1.27 \times 10^{-3}$, neither of which are problematic. Taking E_{52} to be as low as 4 and $t_{c,R}$ and $t_{m,R}$ to be as low as the duration of the burst ($T_{90} = 2.41 \pm 0.15$ sec in the 30 – 85 keV band, in which νF_ν peaks; (Crew et al. 2003), yields $\epsilon_B \approx 0.04$. In this case, $\epsilon_e \approx 0.0002$ and $A_* \approx 0.01$. However, for ϵ_B to be this low requires considerable fine tuning: If E_{52} is as high as 11, $t_{c,R}$ is as high as 54 sec, $t_{m,R}$ is as high as 11 sec, or lesser combinations of these three, $\epsilon_B \approx 1$. Consequently, ϵ_B is likely considerably more than 0.04, in which case ϵ_e can be no more than a factor of three greater and is likely less and A_* can only be less.

Finally, for scenario D, using the expression of Granot & Sari (2002) that corresponds to their segment A, we find:

$$\epsilon_B^{-1/4} A_*^{-1} E_{52}^{3/4} = 8.60 \times 10^{-2} \left(\frac{F_{8.5}}{35\,\mu\mathrm{Jy}} \right). \tag{2.21}$$

Combining Equations 3, 4, 5 and 21 yields:

$$\overline{\epsilon}_e = 0.232 \left(\frac{t_{c,R}}{3.9\,\mathrm{min}} \right)^{-0.125} \left(\frac{t_{m,R}}{3.9\,\mathrm{min}} \right)^{0.75} \left(\frac{F_{8.5}}{35\,\mu\mathrm{Jy}} \right)^{-0.5}, \tag{2.22}$$

$$\epsilon_B = 1.71 \times 10^{-5} \left(\frac{t_{c,R}}{3.9\,\mathrm{min}} \right)^{0.625} \left(\frac{t_{m,R}}{3.9\,\mathrm{min}} \right)^{0.51} \left(\frac{F_{8.5}}{35\,\mu\mathrm{Jy}} \right)^{1.5}, \tag{2.23}$$

$$A_* = 2.21 \left(\frac{t_{c,R}}{3.9\,\mathrm{min}} \right)^{-0.25} \left(\frac{t_{m,R}}{3.9\,\mathrm{min}} \right)^{-0.51} \left(\frac{F_{8.5}}{35\,\mu\mathrm{Jy}} \right)^{-1}, \tag{2.24}$$

$$E_{52} = 2.82 \times 10^{-3} \left(\frac{t_{c,R}}{3.9\,\mathrm{min}} \right)^{-0.125} \left(\frac{t_{m,R}}{3.9\,\mathrm{min}} \right)^{-0.51} \left(\frac{F_{8.5}}{35\,\mu\mathrm{Jy}} \right)^{0.5}, \tag{2.25}$$

If we additionally require that $\nu_m < 8.5$ GHz $< \nu_{sa}$ at 13 days after the burst, we find that $t_{m,R} > 2.9$ min, which is technically consistent with $t_{m,R} < 3.9$ min, and $F_{8.5} > 7$ μJy, which is consistent with $F_{8.5} < 35$ μJy. Once again, this constrains these parameters' values to relatively narrow ranges and by Equation 25 implies a value for E_{52} that is much too low. Consequently, we rule out this scenario as well.

Consequently, we find that $\nu_m < \nu_R < \nu_c$ after <3.9 minutes after the burst and $\max\{\nu_{sa},\nu_m\} < 8.5$ GHz around 13 days after the burst. In this scenario, $\overline{\epsilon}_e$ and A_* are considerably lower than canonical values. Since $F_R \propto \overline{\epsilon}_e^{0.68} \epsilon_B^{0.67} A_* E_{52}^{0.67}$ (Equation 3), both of these contribute to the faintness of the afterglow (§1).

If we allow ourselves to be guided by the standard-energy result (Frail et al. 2001; Bloom et al. 2003), E_{52} is also lower than what one might expect: For wind-swept media, the total energy released in gamma rays is typically measured to be many $\times 10^{50}$ erg (Bloom et al. 2003). Given that the isotropic-equivalent energy in gamma rays for GRB 021211 was $(1.0 \pm 0.1) \times 10^{52}$ erg (Holland et al. 2004) or $1.68^{+0.32}_{-0.27} \times 10^{52}$ erg (Lamb et al. 2004), this implies a jet opening/viewing angle of $\approx 20°$, which is about three times the canonical value. Hence, E_{52} is probably about an order of magnitude less than what one might have expected. Consequently, we find that GRB 021211's afterglow is faint for a combination of 3 – 4 reasons: (1) a low fraction of energy in relativistic electrons, (2) a low density for the wind-swept medium, implying either a low mass-loss rate and/or a high wind velocity for the progenitor, (3) a wide opening/viewing angle for the jet, and possibly (4) moderate source-frame extinction (§3.2).

Equipartition between the energy in the electrons and magnetic field ($\epsilon_B \approx \epsilon_e \approx 0.1$) has been typically assumed for GRB afterglow shocks in the standard model, although Weibel shock theory find that $\epsilon_e \propto \sqrt{\epsilon}_B$ (Medvedev 2006). Furthermore, with $\epsilon_B/\overline{\epsilon}_e > 200$ and ϵ_B likely much greater than 0.04 the jet appears to be significantly far from equipartition and magnetically dominated. This is similar to SN 1993J, for which the magnetic field energy density is $\sim 10^4$

times the relativistic particle energy density (Chandra et al. 2004), but dissimilar to SN 1998bw (Kulkarni et al. 1998) and SN 2002ap (Björnsson & Fransson 2004), which appear to be near equipartition.

These findings are supported by the existence of the bright reverse shock: Fox et al. (2003a) dismiss the possibility of a wind-swept medium because for canonical values of $\overline{\epsilon}_e^{rs}$, ϵ_B^{rs}, A_*, and E_{52}, ν_c^{rs} is expected to be significantly less than ν_m^{rs}, in which case the reverse shock is expected to fade away quickly and not be bright (Chevalier & Li 2000). However, this is not the case when $\overline{\epsilon}_e^{rs}$, ϵ_B^{rs}, and/or A_* are sufficiently low. Taking $\overline{\epsilon}_e^{rs} \approx \overline{\epsilon}_e$ and $\epsilon_B^{rs} \approx \epsilon_B$ and substituting Equations 17, 18, and 19 into Equations 45 and 47 of Chevalier & Li (2000), we find:

$$\nu_c^{rs}/\nu_m^{rs} = 5.56 \times 10^4 E_{52}^3 \left(\frac{t_{m,R}}{3.9\,\mathrm{min}}\right)^{0.03} \left(\frac{t}{1\,\mathrm{min}}\right)^2, \tag{2.26}$$

for $X = 0.75$, $\Delta_{10} = 3$, and $\gamma_3 = 0.3$. For $t = 1$ minute after the burst, corresponding to the beginning of the first detection of the reverse shock (Wozniak et al. 2002), E_{52} need only be greater than $\approx$0.03 for $\nu_c^{rs} \approx \nu_m^{rs}$.

2.5 Conclusions

GRB 021211 is one of only a handful of GRBs for which processes other than the forward shock have been identified at optical wavelengths, which has made it one of the most studied GRBs. Here we present additional, multi-band observations of this event, ranging from minutes to months after the burst, which in combination with all previously published observations have allowed us to deeply probe the physics of this GRB and properties of its circum-progenitor environment.

Coupling the standard afterglow model with a general-purpose extinction curve model, we find that the afterglow is best described by propagation through a wind-swept medium, which implies a massive-star progenitor (e.g., Price et al. 2002). The jet itself appears to be significantly far from equipartition and mag-

netically dominated. Indeed, the low fraction of energy in relativistic electrons appears to be the primary reason that this afterglow is so faint. This, combined with a low-density medium, a wide jet opening/viewing angle, and possibly moderate extinction might be important clues as to why many afterglows are dark/dim in the $Swift$ era, even at early times after the burst. These findings are supported by the existence of the bright reverse shock – in a wind-swept medium this should only be possible if A_* is low and/or the jet is significantly far from equipartition, meaning that either $\overline{\epsilon}_e^{rs}$ or ϵ_B^{rs} is low as well.

Chapter 3

Dark Due to Extinction: GRB 030115 & GRB 050408

The very first significantly dark afterglow, GRB 970828, was attributed to extinction (Groot et al. 1998a). With the clear association between the most massive stars and GRBs (Stanek et al. 2003; Hjorth et al. 2003), we expect for the progenitors to lie within the molecular clouds in which they were formed. A molecular cloud environment is strengthened by the observations of large ($\sim 10^{22}$ cm^{-2}) column densities of neutral hydrogen found in the x-ray afterglows (Galama & Wijers 2001; Reichart & Price 2002; De Pasquale et al. 2003; Stratta et al. 2004). With small localizations, even without the presence of an optical afterglow, observers have found dusty, luminous star-forming galaxies that are the likely hosts (Pellizza et al. 2006; Nakagawa et al. 2006).

The jets of a burst are powerful and depending on the geometry and circumburst density can pierce the cloud surrounding the progenitor and destroy line of sight dust to even further distances. If, as the results of Frail et al. (2001) suggest, the jets contain a roughly standard amount of energy, then the narrower jets will be able to destroy intervening dust more efficiently than wide jets, whose energy is spread out over a larger solid angle (Reichart & Yost 2001). Figure 1.2 presents a rough outline of this idea. Brighter x-ray jets are more highly

collimated, and hence less likely to have extinguished optical afterglows, while dim x-ray afterglows will have a continuum of dim or dark optical afterglows depending on the amount of dust destruction in the surrounding medium.

Extinction Curve Model

Modeling the afterglows of gamma-ray bursts not only requires an understanding of the underlying model, but also line-of-sight effects on the traveling photons. It is necessary to accurately determine the effects and amount of extinction along the travel path of the light in order to recreate the underlying synchrotron spectrum characteristics. The extinction model described here and used for the modeling effort was presented in Reichart (2001a) and is based on Fitzpatrick & Massa (1988) in the ultraviolet and Cardelli et al. (1989) in the optical and near-infrared. It has a number of free parameters and necessary priors that are observationally based on Galactic and Magellanic Cloud sources. Because measuring extinction curves requires a point-source of light, extinction curves have not been regularly measured outside of the local group, which adds a small but additional level of uncertainty to some of the assumed priors. Also, less well-studied portions of the source frame FUV extinction curve are redshifted into observed optical wavelengths, which adds further ambiguity. Reichart (2001a) describes the Bayesian inference formalism in detail.

The extinction curve model depends on eight parameters, many of which are related and constrained by prior probability distributions. The two extinction functions, optical/NIR and UV, are fitted together using a weighted average between 300 and 550 nm. The two parameters that govern the optical and near-infrared are A_V and R_V. A_V is the amount of extinction in the V filter that normalizes the extinction curve. $R_V = A_V \; / \; E(B-V)$, so it is a measure of the slope of the extinction curve between the V and B filters. The typical Galactic value of R_V is 3.1, but for dense clouds, it can range as high as $R_V \approx 4 - 5$. The

extinction curve is given as:

$$\frac{A_\lambda}{A_V} = a(\lambda) + \frac{b(\lambda)}{R_V} \tag{3.1}$$

where a and b are functions that depend on the inverse of the wavelength.

The FUV extinction curve of Fitzpatrick & Massa (1988) is defined as:

$$\frac{E(\lambda - V)}{E(B - V)} = c_1 + c_2 x + c_3 D(x; \gamma, x_o) + c_4 F(x) \tag{3.2}$$

c_1 and c_2 are the zero-point and slope of the linear portion of the overall UV fit from 100 nm $< \lambda <$ 300 nm. c_3 is the strength of the FUV bump, D(x; γ, x_o), and c_4 is a measure of the nonlinearity in the FUV. The linear component is governed by the distribution of grain sizes in the obscuring dust. Large grains will extinguish at longer and shorter wavelengths, but small grains only at short, hence the slope of the line, c_2 is a measure of the properties of the intervening dust. For typical interstellar dust, values of c_2 range from 0.5 to 1, but dense, young clouds such as the Orion Nebula will have larger grains with c_2 closer to 0 (i.e. grey dust; Fitzpatrick & Massa 1988). Older star-forming regions that have undergone multiple supernova shocks, such as 30 Doradus, can have $1 < c_2 <$ 2.5 (Calzetti et al. 1994; Gordon & Clayton 1998; Misselt et al. 1999).

Physical processes, such as stellar radiation, shocks or evaporation of grains in the progenitor environment can modify the ratio of grain sizes. The GRB jet itself can also change the properties of the intervening dust through sublimation and fragmentation. The bright optical flash will sublimate small particles through thermal heating out to $\approx$ 1 parsec, and large particles out to $\approx$ 10 parsecs. Fragmentation due to photoionization by x-rays will affect large grains to tens of parsecs and small grains out to hundreds of parsecs (Waxman & Draine 2000; Fruchter et al. 2001). Eventually, with a large sample size of afterglows with measured extinction curves we can observationally test these hypotheses. This chapter presents two examples of measuring extinction in a gamma-ray burst afterglow, GRB 030115 and GRB 050408.

3.1 GRB 030115

The very red and dim afterglow of GRB 030115 was first discovered by Levan et al. (2003) at near-infrared wavelengths, and then only later confirmed to be visible in the optical (Masetti et al. 2003a). No x-ray afterglow was observed, so we cannot use Jakobsson et al. (2004)'s definition of *dark* and find the optical to x-ray spectral slope for this burst, but it is certainly one of the dimmest GRBs observed, and without the results of early-time near-infrared observations would likely have been missed in a standard afterglow search. We have modeled the afterglow observations made by the FUN GRB Collaboration and found that the burst is dark because it suffers from relatively high extinction: $1.35^{+1.06}_{-0.79} < \mathrm{A}_V < 1.5^{+0.87}_{-0.71}$ mag.

Levan et al. (2006) performed a similar analysis of the spectral flux distribution of the afterglow of GRB 030115, but also made deep observations of the host galaxy and surrounding field. They find that the burst arose in an extremely red galaxy ($R - K = 5$) that is part of a larger cluster of star-forming galaxies near $z \approx 2.5$. Their simple extinction model gives only unphysical solutions, but they do note that the ($R - K = 5.7$) color of the afterglow is atypical of standard afterglows ($R - K \approx 2.9$) and is the result of high extinction in the host galaxy.

3.1.1 Observations

The *HETE-2* FREGATE, WXM and SXC instruments triggered to GRB 030115 at 03:22:34.28 UT on January 15^{th}, 2003 and through ground analysis, localized it to a large $10''$ radius circle 1.2 hours post-burst, then a smaller $2''$ error circle at 1.4 hours. The long burst ($t_{90} \approx 20$ seconds at 4 – 40 keV) was also observed by two other satellites, *INTEGRAL* and *Ulysses*, but no search was made for an x-ray afterglow.

A number of teams rapidly observed the error circle at optical wavelengths, but they were not able to identify a clearly fading afterglow to the limit of the

Digitized Sky Survey archived field images (Flaccomio et al. 2003; Castro-Tirado et al. 2003; Blake et al. 2003; Atteia et al. 2003; Masetti et al. 2003b). These observations placed a limit on the early optical emission of the burst to $R \approx 21$ at 2 hours. A possible near-infrared JHK afterglow was announced by Levan et al. (2003) and confirmed by Vrba et al. (2003) to be fading. Upon reanalysis of their images, Masetti et al. (2003a) found that the afterglow was detected in their R images at $R \approx 21.5$.

Early radio observations were made with the VLA (Berger & Frail 2003) at 8.46 GHz that only resulted in an upper limit, but later observations (Frail & Berger 2003) made at 2 days discovered a 94 ± 22 μJy source coincident with the NIR afterglow. Rol & Wijers (2003) used the Westerbork Synthesis Radio Telescope to observe the field at 4.9 GHz at three epochs between 1.5 and 12 days, and detected the source at 0.06 ± 0.01 mJy. Observations were made at 850 μm with Sub-millimetre Common-User Bolometer Array (SCUBA) on the James Clerk Maxwell Telescope at around 3 days, but at this time, the afterglow was too faint to produce significant constraints on the underlying emission (Smith et al. 2005b). Upper limits at 1 and 3 days were also found at with the Max-Planck Millimeter Bolometer (MAMBO) array at the 30-m IRAM Telescope at 1.2 mm.

FUN GRB Observations

We began observations with the 3.5-m ARC (Astrophysical Research Consortium) Telescope at Apache Point Observatory of the field of GRB 030115 at 07:01 UT, only 3.6 hours after the GRB, and 2.4 hours after the GCN localization in ri. An initial comparison with the Digitized Sky Survey (limiting magnitude of $R \approx 21$) found no bright, fading optical transient. This did not, however, exclude the possibility of an afterglow fainter than this limit. After discovery of the NIR afterglow (Levan et al. 2003), we reanalyzed the optical images and found a faint afterglow in both filters.

At 8.7 hours post-burst we began observations with the NIR camera AstroCam on the U.S. Naval Observatory 1.55-m telescope in JH and with the 1.0-m telescope in BV. We did not obtain constraining limiting magnitudes in the optical filters but we detected the afterglow in J on the first night, and in H over three nights.

Table 3.1 presents all FUN GRB observations along with those of Kato et al. (2003). Optical observations are calibrated with respect to the field calibration of Vrba et al. (2003). All images were reduced and psf-photometered using IRAF's CCDPROC and DAOPHOT package. The conversions of Smith et al. (2002) are used to convert Johnson/Cousins $UBVRI$ to ri. The NIR observations are calibrated relative to standards taken on subsequent nights.

Table 3.1: FUN GRB Observations of the Afterglow of GRB 030115

Date (UT)	Mean Δt	Filter	Magnitude[a]	Telescope
Jan 15.322	4.35 hr	i	22.14 $\pm$ 0.05	3.5m ARC
Jan 15.334	4.64 hr	r	23.40 $\pm$ 0.11	3.5m ARC
Jan 15.371	5.53 hr	J	19.78 $\pm$ 0.20	1.55m USNO
Jan 15.372	5.55 hr	H	18.28 $\pm$ 0.13	1.55m USNO
Jan 15.418	6.66 hr	B	$>$21.4	1.0m USNO
Jan 15.418	6.66 hr	H	18.46 $\pm$ 0.11	1.55m USNO
Jan 15.436	7.09 hr	V	$>$21.2	1.0m USNO
Jan 16.0	20.6 hr	J	20.4 $\pm$ 0.2	1.4m IRSF
Jan 16.0	20.6 hr	H	19.9 $\pm$ 0.3	1.4m IRSF
Jan 16.0	20.6 hr	$K_{\rm s}$	18.5 $\pm$ 0.2	1.4m IRSF
Jan 16.468	1.33 day	H	19.69 $\pm$ 0.26	1.55m USNO
Jan 17.1	2.0 day	J	21.5 $\pm$ 0.5	1.4m IRSF
Jan 17.1	2.0 day	H	20.4 $\pm$ 0.4	1.4m IRSF
Jan 17.1	2.0 day	$K_{\rm s}$	19.1 $\pm$ 0.2	1.4m IRSF
Jan 17.414	2.27 day	H	20.55 $\pm$ 0.19	1.55m USNO

[a]Upper limits are 3σ.

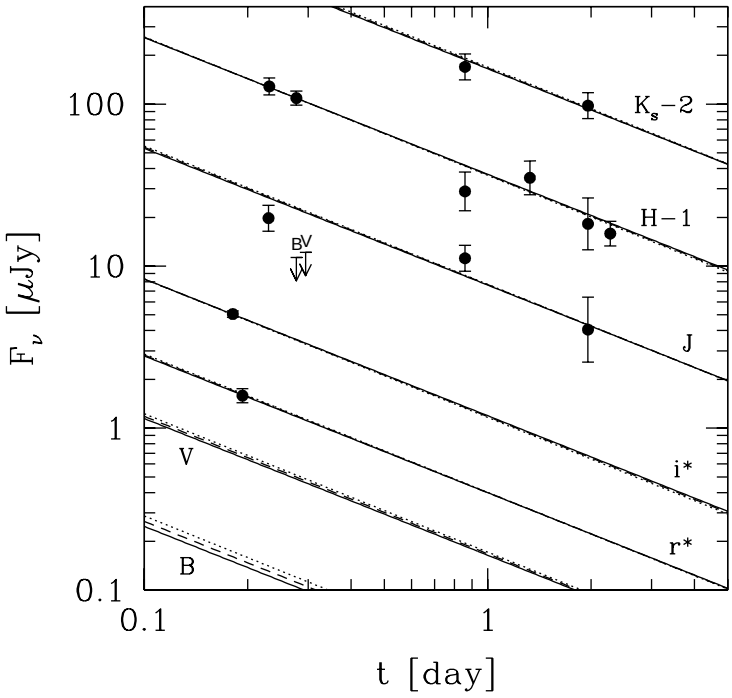

Figure 3.1: The highly reddened afterglow of GRB 030115. Solid lines are fit for a wind-swept environment with $\nu_c > \nu_{opt}$, dashed are for a constant density medium with $\nu_c > \nu_{opt}$, and dotted are for both the wind & constant density medium with $\nu_c < \nu_{opt}$. Although the afterglow is not highly-sampled, it is clearly very red.

3.1.2 Analysis

We fit our model to all data that are listed in Table 3.1, which includes $BVriJHK_{\rm s}$ FUN GRB Collaboration data beginning at 3.6 hours and lasting until 2 days along with data distributed through the GCN Circulars (Kato et al. 2003). Although the light curve is not well-sampled, we do not see significant deviations from a simple power-law decline. All magnitudes are converted to fluxes as prescribed by Bessell (1979), Bessell & Brett (1988), and Fukugita et al. (1995).

We model the afterglow as a single power law light curve with a power law

spectrum of the form:

$$F_\nu(t) = e^{-\tau_\nu^{MW}} e^{-\tau_{\nu(1+z)}^{Ly\alpha}} e^{-\tau_{\nu(1+z)}^{source}} F_0 \left(\frac{t}{t_0}\right)^\alpha \left(\frac{\nu}{\nu_J}\right)^\beta. \quad (3.3)$$

τ_ν^{MW} is the Galactic extinction curve model of Cardelli et al. (1989), $\tau_{\nu(1+z)}^{Ly\alpha}$ is the Lyα forest absorption model of Reichart (2001a), and $\tau_{\nu(1+z)}^{source}$ is the source-frame extinction curve and Lyman limit absorption model of Reichart (2001a). α is the temporal index of the light curve and β is the spectral index. F_0 is the flux normalization, and t_0 = 20.6 hours and ν_J [log GHz] = 14.391 are arbitrary normalization constants. The model is integrated against the appropriate filter transmissivity curve before being fit to the data.

The model is fit using Bayesian analysis and the genetic fitting code described in detail in §2.3 (see also §3.1.2, §4.3, §7.7). The Galactic extinction curve model (Cardelli et al. 1989) is a function of $E(B-V)$ = 0.019 magnitudes (Schlegel et al. 1998). The extinction curve parameter c_4 was not constrained by the model. Because the spectroscopic redshift of this burst is unknown, we adopted an additional prior to constrain the fit to use the photometric redshift of z = 2.5 ± 0.18 (Levan 2005, private communication). The redshift is represented as a normal distribution centered around 2.5, with standard deviation of 0.18.

3.1.3 Discussion

We fit the data to each of the standard model scenarios, but were unable to determine which scenario is the most likely; Wind-Blue (ρ^{-2}, $\nu_c > \nu_{opt}$) is preferred at only the 0.4 σ level over ISM-Blue (ρ^0, $\nu_c > \nu_{opt}$), and is preferred 0.7 σ over ISM/Wind-Red (ρ^0, ρ^{-2}, $\nu_c < \nu_{opt}$). Each scenario compensates for a steeper spectral index by increasing the amount of extinction. Details of the model for each case are presented in Table 3.1. Model light curves are plotted in Figure 3.1, and the spectral flux distribution at 5.55 hours is plotted in Figure 3.2.

Even though we are unable to determine which scenario best describes the afterglow, we find that A_V ranges from $1.35^{+1.06}_{-0.79}$ mag for ISM & Wind-Red to

Table 3.2: GRB 030115: Best-Fit Parameter Values and 68.3% Error Bars

Parameter	WIND-BLUE	ISM-BLUE	ISM/WIND-RED
$\log F_0$ [μJy]	$1.93^{+0.33}_{-0.29}$	$1.82^{+0.37}_{-0.30}$	$1.73^{+0.42}_{-0.32}$
α	-0.84 ± 0.06	-0.85 ± 0.06	-0.85 ± 0.06
β^a	-0.23 ± 0.04	-0.57 ± 0.04	-0.90 ± 0.04
p^a	1.46 ± 0.08	2.13 ± 0.08	1.81 ± 0.08
A_V [mag]	$1.50^{+0.87}_{-0.71}$	$1.40^{+0.95}_{-0.74}$	$1.35^{+1.06}_{-0.79}$
c_2	$1.94^{+0.48}_{-0.34}$	$2.11^{+0.62}_{-0.42}$	$2.35^{+0.84}_{-0.54}$
c_3	$0.0^{+1.6}_{-0.0}$	$0.0^{+2.3}_{-0.0}$	$0.0^{+4.1}_{-0.0}$
σ [mag]	$0.00^{+0.06}_{-0.00}$	$0.00^{+0.06}_{-0.00}$	$0.00^{+0.06}_{-0.00}$

[a]Function of α.

$1.50^{+0.87}_{-0.71}$ mag for Wind-Blue. The large error bars are predominantly due to the uncertainty in the redshift, but the model constrains $A_V > 0$ mag at the 8.3 σ for the Wind-Blue scenario (7.8 σ: ISM-Blue; 7.3 σ: ISM & Wind-Red). The values for c_2 ($1.94^{+0.48}_{-0.34}$, $2.11^{+0.62}_{-0.42}$, $2.35^{0.84}_{-0.54}$) resemble an SMC distribution and suggests that the local environment is dominated by small grains.

3.2 GRB 050408

GRB 050408 is an example of a burst that is *dim* due to a moderate amount of extinction in the host galaxy. The FUN GRB Collaboration observed the bright afterglow in $UBVRIZJHK_s$ at 0.5 days in order to obtain a spectral flux distribution and search for evidence of circumburst extinction. The optical afterglow is well-described by a single power-law extending from four hours to five days after the burst and does not show signs of a jet break. We have modeled the afterglow and found (1) $0.53 < A_V < 0.70$ magnitudes and (2) from the broadband spectrum that a break, possibly ν_c, lies between the optical and x-ray at 12 hours.

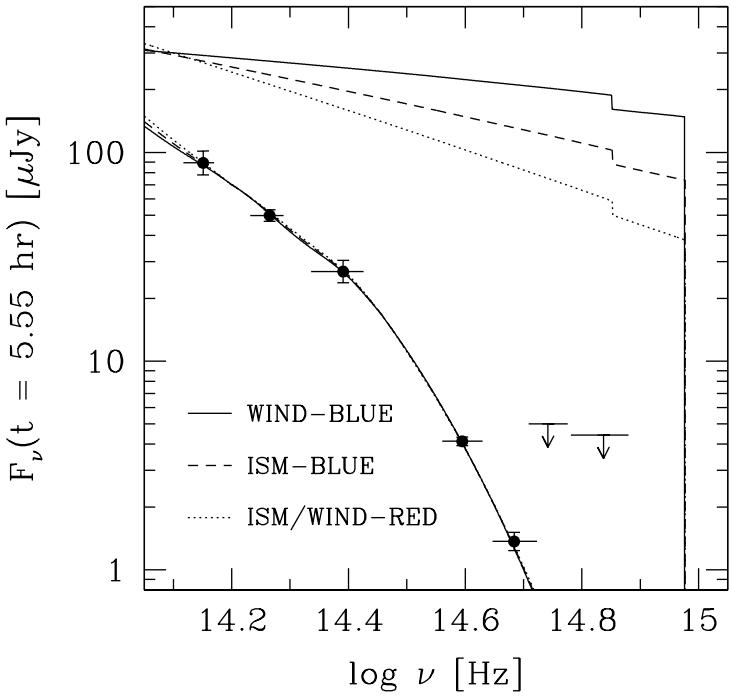

Figure 3.2: The $BVriJHK_s$ spectral flux distribution of GRB 030115. All data are scaled to t = 5.55 hours using the best fit light curve. For bands with more than one point, weighted averages of the scaled data are plotted. Solid lines are fit for a wind-swept environment with $\nu_c > \nu_{opt}$, dashed are for a constant density medium with $\nu_c > \nu_{opt}$, and dotted are for both the wind & constant density medium with $\nu_c < \nu_{opt}$. Both the extinguished model and base unextinguished spectral flux distributions are plotted.

Although the bright, doubly-peaked GRB 050408 was discovered with *HETE-2*, *Swift* was manually triggered to observe the x-ray afterglow of this burst beginning at 42 minutes. The x-ray afterglow of this burst has been well-studied by many groups. Chincarini et al. (2005) analyze seven *Swift* XRT x-ray afterglows with known redshift, and their sample includes GRB 050408. They find an 0.2 – 10 keV spectral index of $\beta_x = -1.14 \pm 0.19$ with a moderate amount of host neutral hydrogen contaminating the spectrum, $N_H = (2.5 \pm 0.5) \times 10^{21}$ cm^{-2} and no evidence for spectral evolution. The x-ray light curve follows closely the same temporal slope as the optical light curve ($\alpha_{opt} \approx \alpha_x \approx -0.6$) until some-

time between 7.3 and 31 hours, when they see a break to $\alpha_x \approx -1.3$. Figure 3.3 presents the *Swift* x-ray light curve at 1 keV (Capalbi et al. 2006) along with R-band observations presented here and also taken from the GCN Circulars.

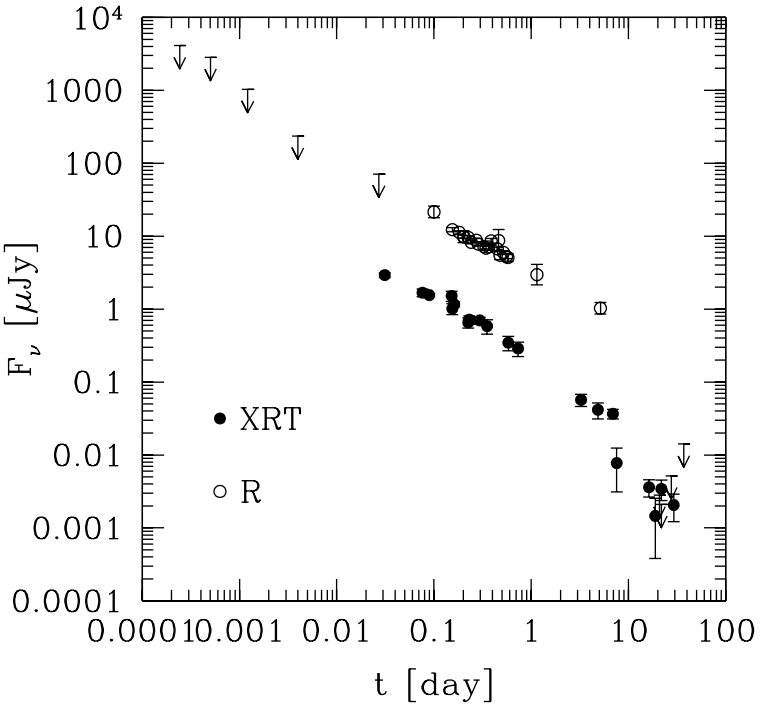

Figure 3.3: The *Swift* x-ray afterglow of GRB 050408 (Capalbi et al. 2006) is plotted alongside the optical R afterglow for comparison. The values in the R-band light curve come from this work along with that of Foley et al. (2006), and from the GCN Circulars: Smith et al. (2005a), Wiersema et al. (2005), Misra et al. (2005), Mizuno et al. (2005), Torii (2005a), Kahharov et al. (2005), Bikmaev et al. (2005).

Panaitescu et al. (2006) analyze nine *Swift* x-ray afterglows, including GRB 050408, to explore their general behavior. GRB 050408 follows the typical XRT afterglow light curve: an extreme steep early slope (t^{-3}), a break to a shallower slope ($t^{-2/3}$), and then a later break to a moderate slope ($t^{-5/3}$). In the case of GRB 050408, x-ray observations began during the second portion ($t^{-2/3}$) of the general afterglow phase. The breaks in the x-ray light curves cannot be simply accounted for by the standard model cases outlined in Sari et al. (1998).

They test the data against several more specific models: (1) spherical outflow, (2) non-spreading jet, (3) sideways spreading jet, and (4) radiative afterglow, for both fully adiabatic ($\nu_x < \nu_c$) and radiative ($\nu_c < \nu_x$) cooling. Using these more complex models, they find that before the break from $\alpha \approx -2/3$ to $\approx -5/3$, the afterglow is best described as spherical (relativistic) outflow with $\nu_x < \nu_c$, while after the break it is best described as non-spreading jet with $\nu_c < \nu_x$. They also find that in order to explain the second phase shallow slope, it is necessary to invoke continuous energy injection into the forward shock or angular structure in the jet. Energy injection from the progenitor itself may produce a shallower slope, although it is difficult to discern the amount of effect it plays on individual afterglows.

Foley et al. (2006) reanalyze the x-ray afterglow data and observe the optical and near-infrared afterglow of GRB 050408. Combining their own observations and those from the GCN Circulars, they obtained a $VRIZJHK$ spectral flux distribution centered at one day and optical spectrum of the afterglow around 14.5 hours that shows z = 1.236. They find that the optical and near-infrared SFD prefers extinction of $A_V = 0.57$ mag, but when considering the relations between the optical and the x-ray light curve, they find A_V may be closer to one. They do not find evidence for a jet break before the fifth day in the optical, which contradicts the results of Panaitescu et al. (2006) and Covino et al. (2005). Similarly, the team performed a new reduction of the x-ray data, which differs from the analysis of Chincarini et al. (2005). They find possible evolution of the spectral index (β_x = -1.31 $\pm$ 0.75 to -0.33 $\pm$ 0.5) and temporal indices that differ slightly from the original reduction. The optical spectrum with which they obtained the redshift shows atypical abundances and large line velocities that cannot easily be explained by the host galaxy; the features are likely due the circumburst environment being shaped by the winds of a massive star.

3.2.1 Observations

HETE-2 detected the x-ray rich gamma-ray burst, GRB 050408, at 16:22:50.9 UT on 8 April 2005 (Sakamoto et al. 2005). At 22 seconds after the burst, the WXM & SXC instruments announced the final flight real-time localization to a 16 square arcminute error circle, and at 74 minutes, ground analysis confined the burst to an 8.4 square arcminute error circle. Responding to a target of opportunity observation, the *Swift* XRT observed the field and found a bright, fading x-ray source (Wells et al. 2005) consistent with the *HETE-2* ground analysis and with positional uncertainty of 6 arcseconds.

The discovery of the optical afterglow (R $\approx$ 20.5 magnitudes) of GRB 050408 was announced by de Ugarte Postigo et al. (2005b) from images taken 3.9 hours after the event, and confirmed to be fading by Huang et al. (2005) shortly thereafter. Subsequent follow-up efforts reported optical and near-infrared magnitudes in the GCN Archive, which followed the dwindling light of the afterglow for over five days. Throughout this time, the temporal decay is fit well with an approximate $\alpha = -0.7$ slope, and at 5.2 days, is R = 23.7 $\pm$ 0.2 magnitudes (Bikmaev et al. 2005). Radio follow-up efforts (Soderberg 2005) resulted in a non-detection 2-sigma upper limit of 74 $\pm$ 29 μJy at the site of the optical afterglow.

Berger et al. (2005a) obtained a spectrum of the optical afterglow with LDSS-3 on the Magellan/Clay telescope and found a redshift of z = 1.236 for the source. This redshift was quickly confirmed by Prochaska et al. (2005), who found z = 1.2357 $\pm$ 0.0002 using GMOS on Gemini. Given the 2 – 400 keV fluence of $\approx$3.3 $\times$ 10^{-6} ergs cm^{-2}, this redshift implies an isotropic equivalent energy of 1.3 $\times$ 10^{52} ergs (Berger et al. 2005a).

FUN GRB Observations

The FUN GRB Collaboration observed this burst with the SOAR 4.1-m (UNC), ARC 3.5-m (U. Chicago), Kuiper 1.5-m (Arizona) and the SARA 0.9-

m (Clemson). The results of the observations are listed in Table 3.3 and are presented in Figure 3.4. The largest strength of this set of observations is the simultaneous $BVRIJHK$ spectrum obtained with SOAR, Kuiper & ARC around 12 hours. Each set of observations was reduced using IRAF's CCDPROC package and photometered using IRAF's DAOPHOT package using a standard two FWHM aperture.

We began observations with the SOAR Optical Imager (2 x 2048 x 4096 E2V CCDs) on the SOAR 4.1-m Telescope at CTIO at 01:40:19 UT on April 9^{th}, 9.3 hours after the burst trigger. The afterglow is well detected in 10 $\times$ 200 second exposures in R, 9 $\times$ 200 second exposures in each of V and B, and we obtained a limiting magnitude for 9 $\times$ 300 seconds in U.

We began observations with the 2K $\times$ 2K CCD imager on the Kuiper 1.54-m Telescope at Mt. Bigelow, AZ at 03:34:14 UT on April 9^{th}, 11.3 hours after the burst trigger. The afterglow is well detected in 11 $\times$ 120 second exposures in each of R and V, and 9 $\times$ 120 second exposures in I. A second series of exposures was initiated upon completion of the first series, at 05:53:45 UT. The second series consisted of 6, 7, 8, 7 $\times$ 300 second exposures in the $BVRI$ filters, respectively. A third series of exposures was initiated at 06:07:25 UT on April 10^{th} 2005. The third series consisted of 4 $\times$ 300 second exposures in the $BVRI$ filters.

Nearly simultaneously, we observed the field with the NIC-FPS NIR Camera on the ARC 3.5-m Telescope located at Apache Point Observatory. Observations began at 04:28:12 UT on April 9^{th}, 12.3 hours after the burst trigger. The afterglow was well-detected in 20 minute median combined images in all four filters, $ZJHK_s$. The NIR Z filter is nearly-equivalent to SDSS z, and the field was calibrated to this filter.

The SARA 0.9-m Telescope at Kitt Peak observed the field of GRB 050408 in I beginning on April 9^{th} 02:58:13 UT. The 20 $\times$ 300 second images were combined to produce a single image with a mean time of 03:47:49 UT. The afterglow was not detected in this final image.

Table 3.3: Observations of the Afterglow of GRB 050408

Mean Time (UT)	Mean Δt (days)	Filter	Magnitude	Source
Apr 9 4:30:26	0.5053	$UVW1$	> 22.30	UVOT
Apr 9 4:48:56	0.5181	$UVM2$	> 22.50	UVOT
Apr 9 4:24:21	0.5010	$UVW2$	> 22.70	UVOT
Apr 9 2:31:05	0.4224	U	> 21.90	UVOT
Apr 9 3:51:13	0.4780	U	23.09 ± 0.18	SAO RAS[a]
Apr 9 5:17:11	0.5377	U	> 22.56	SOAR
Apr 9 2:44:32	0.4317	B	> 22.20	UVOT
Apr 9 4:13:51	0.4938	B	23.00 ± 0.11	SOAR
Apr 9 5:11:27	0.5338	B	22.69 ± 0.11	SOAR
Apr 9 6:07:26	0.5726	B	23.28 ± 0.19	SOAR
Apr 9 8:24:00	0.6675	B	22.37 ± 0.17	Kuiper
Apr 9 2:06:44	0.4055	V	22.12 ± 0.24	PROMPT
Apr 9 2:42:12	0.4301	V	> 21.40	UVOT
Apr 9 4:02:34	0.4859	V	22.37 ± 0.06	SOAR
Apr 9 4:48:00	0.5175	V	22.07 ± 0.17	Kuiper
Apr 9 5:00:28	0.5261	V	22.37 ± 0.07	SOAR
Apr 9 5:50:07	0.5606	V	> 19.40	PROMPT
Apr 9 5:56:49	0.5653	V	22.41 ± 0.09	SOAR
Apr 9 7:40:48	0.6375	V	22.62 ± 0.19	Kuiper
Apr 10 6:57:36	1.6075	V	23.48 ± 0.61	Kuiper
Apr 11 8:08:32	2.6567	V	24.07 ± 0.18	Keck[b]
Apr 8 20:06:03	0.1550	R	21.01 ± 0.07	RTT150[c]
Apr 8 20:45:00	0.1820	R	21.10 ± 0.05	RTT150[c]
Apr 8 21:16:12	0.2037	R	21.25 ± 0.05	RTT150[c]
Apr 8 21:46:12	0.2245	R	21.27 ± 0.05	RTT150[c]
Apr 8 22:10:12	0.2412	R	21.44 ± 0.06	RTT150[c]
Apr 8 22:55:48	0.2729	R	21.37 ± 0.06	RTT150[c]
Apr 8 23:13:48	0.2854	R	21.50 ± 0.06	RTT150[c]

Upper limits are 3σ. [a]de Ugarte Postigo, Private communication; [b]Foley et al. (2006); [c]Bikmaev et al. (2005).

Table 3.3 (continued)

Mean Time (UT)	Mean Δt (days)	Filter	Magnitude	Source
Apr 9 0:12:00	0.3258	R	21.58 $\pm$ 0.10	Magellan[b]
Apr 9 0:37:12	0.3433	R	21.64 $\pm$ 0.07	RTT150[c]
Apr 9 1:07:48	0.3645	R	21.60 $\pm$ 0.07	RTT150[c]
Apr 9 1:40:19	0.3871	R	21.39 $\pm$ 0.08	SOAR
Apr 9 3:29:00	0.4626	R	21.38 $\pm$ 0.38	PROMPT
Apr 9 3:07:04	0.4474	R	21.66 $\pm$ 0.05	SOAR
Apr 9 3:50:24	0.4775	R	21.89 $\pm$ 0.15	Kuiper
Apr 9 4:48:32	0.5178	R	21.79 $\pm$ 0.05	SOAR
Apr 9 5:45:28	0.5574	R	21.93 $\pm$ 0.07	SOAR
Apr 9 6:14:24	0.5775	R	21.96 $\pm$ 0.13	Kuiper
Apr 9 6:46:49	0.6000	R	$>$ 19.50	PROMPT
Apr 13 20:09:39	5.1575	R	23.70 $\pm$ 0.20	RTT150[c]
Apr 9 0:12:00	0.3258	I	21.05 $\pm$ 0.12	Magellan[b]
Apr 9 2:00:00	0.4008	I	$>$ 19.50	PROMPT
Apr 9 3:38:38	0.4693	I	21.47 $\pm$ 0.11	CTIO 1.3m[b]
Apr 9 3:47:49	0.4757	I	$>$ 18.85	SARA
Apr 9 4:19:12	0.4975	I	21.31 $\pm$ 0.20	Kuiper
Apr 9 5:12:54	0.5348	I	$>$ 19.90	PROMPT
Apr 9 6:57:36	0.6075	I	20.69 $\pm$ 0.13	Kuiper
Apr 10 6:14:24	1.5775	I	22.29 $\pm$ 0.39	Kuiper
Apr 9 4:37:51	0.5104	Z	21.80 $\pm$ 0.12	ARC[d]
Apr 9 3:38:00	0.4689	J	20.38 $\pm$ 0.28	CTIO 1.3m[b]
Apr 9 4:37:51	0.5104	J	20.40 $\pm$ 0.08	ARC
Apr 9 6:44:30	0.5984	J	20.59 $\pm$ 0.19	PAIRITEL[b]
Apr 9 4:37:51	0.5104	H	19.60 $\pm$ 0.10	ARC
Apr 9 6:44:30	0.5984	H	19.58 $\pm$ 0.15	PAIRITEL[b]
Apr 9 4:37:51	0.5104	K_s	18.70 $\pm$ 0.08	ARC
Apr 9 6:17:30	0.5796	K_s	18.53 $\pm$ 0.18	PAIRITEL[b]

Upper limits are 3σ. [b]Foley et al. (2006); [c]Bikmaev et al. (2005); [d]Calibrated to SDSS z.

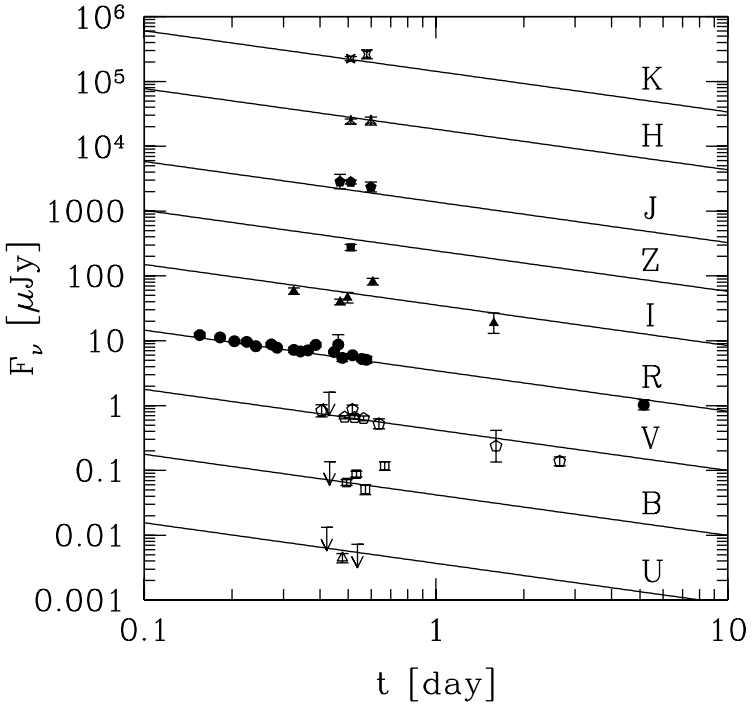

Figure 3.4: The $UBVRIZJHK_{\rm s}$ afterglow of the reddened GRB 050408. The plotted light curve is for the wind-swept scenario with $\nu_c > \nu_{opt}$; the fits were not able to significantly distinguish between the standard cases.

3.2.2 Analysis

We fit our model to all data that are listed in Table 3.3, which includes FUN GRB Collaboration data and data from the GCN archive and Foley et al. (2006). These data begin hours after the event and last to five days. During this time, the afterglow fades as a simple power-law; there is no sign of a host galaxy or break in the light curve. All magnitudes are converted to fluxes as prescribed by Bessell (1979), Bessell & Brett (1988), and Fukugita et al. (1995).

We model the afterglow as a single power law light curve with a power law spectrum of the form:

$$F_\nu(t) = e^{-\tau_\nu^{MW}} e^{-\tau_{\nu(1+z)}^{Ly\alpha}} e^{-\tau_{\nu(1+z)}^{source}} F_0 \left(\frac{t}{t_0}\right)^\alpha \left(\frac{\nu}{\nu_R}\right)^\beta . \tag{3.4}$$

As in previous sections, τ_ν^{MW} is the Galactic extinction curve model of Cardelli

et al. (1989), $\tau^{Ly\alpha}_{\nu(1+z)}$ is the Lyα forest absorption model of Reichart (2001a), and $\tau^{source}_{\nu(1+z)}$ is the source-frame extinction curve and Lyman limit absorption model of Reichart (2001a). α is the temporal index of the light curve and β is the spectral index. F_0 is the flux normalization, and $t_0 = 0.5$ days and ν_R [log GHz] = 14.670 are arbitrary normalization constants. The model is integrated against the appropriate filter transmissivity curve before fitting to the data.

The model is fit using Bayesian analysis as described in detail in §2.3 (see also §3.1.2, §4.3, §7.7). The Galactic extinction curve model (Cardelli et al. 1989) us a function of $E(B-V) = 0.026$ magnitudes (Schlegel et al. 1998). The extinction curve parameters c_3 and c_4 were unconstrained by the model.

Table 3.4: GRB 050408: Best-Fit Parameter Values and 68.3% Error Bars

Parameter	WIND-BLUE	ISM-BLUE	ISM/WIND-RED
$\log F_0$ [μJy]	$1.39^{+0.17}_{-0.12}$	$1.20^{+0.21}_{-0.09}$	$1.05^{+0.14}_{-0.10}$
α	$-0.63^{+0.05}_{-0.05}$	$-0.63^{+0.05}_{-0.05}$	$-0.62^{+0.05}_{-0.06}$
β^a	$-0.08^{+0.03}_{-0.03}$	$-0.42^{+0.03}_{-0.04}$	$-0.75^{+0.03}_{-0.04}$
p^a	$1.17^{+0.07}_{-0.07}$	$1.84^{+0.07}_{-0.07}$	$1.49^{+0.08}_{-0.07}$
A_V [mag]	$0.70^{+0.63}_{-0.29}$	$0.53^{+0.65}_{-0.25}$	$0.40^{+0.37}_{-0.25}$
c_2	$1.59^{+1.31}_{-0.40}$	$2.03^{+1.85}_{-0.51}$	$2.84^{+1.600}_{-0.904}$
σ [mag]	$0.046^{+0.012}_{-0.010}$	$0.045^{+0.011}_{-0.010}$	$0.045^{+0.014}_{-0.012}$

[a]Function of α.

3.2.3 Discussion

Due to the degeneracy between the fitted spectral slope and the amount and type of extinction inferred, we were not able to rule out any of the four scenarios based on the optical and near-infrared data alone. Wind-Blue (wind-swept, $\nu_c > \nu_{opt}$) was preferred only 0.6 σ over ISM-Blue (ISM, $\nu_c > \nu_{opt}$) and 1.3 σ over ISM/Wind Red (ISM & wind-swept, $\nu_c < \nu_{opt}$). Table 3.4 presents

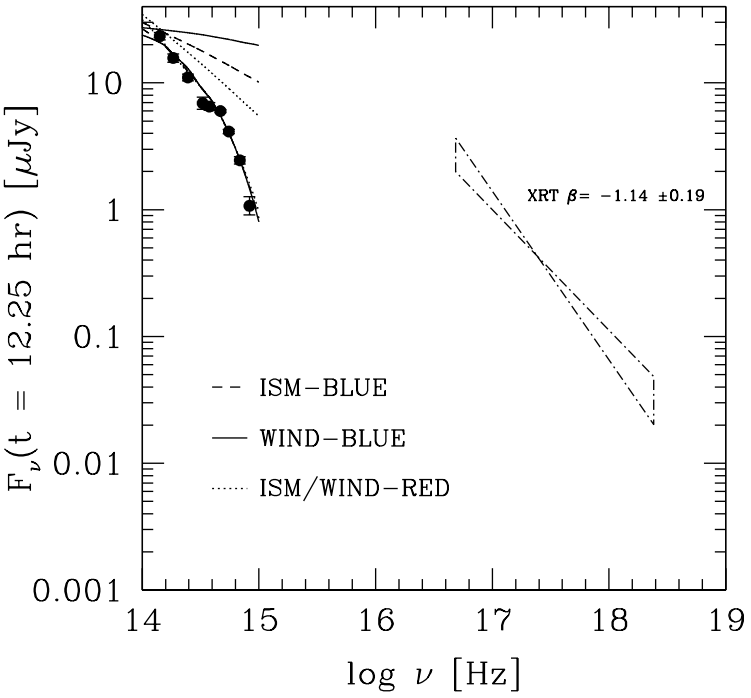

Figure 3.5: The $UBVRIZJHK_{\rm s}$ and 0.5 – 10 keV spectral flux distribution of GRB 050408 scaled to 12.25 hours using the best fit light curve in both the optical and x-ray. For bands with more than one point, weighted averages of the scaled data are plotted. The lines from 10^{14} – 10^{15} Hz represent the optical model fits for the four scenarios. The dotted line at high frequencies is the XRT x-ray spectrum.

the details of each scenario, Figure 3.4 plots the data and model light curves, and Figure 3.5 presents the spectral flux distributions and model spectrum at 12.25 hours. The standard model requires extinction to explain GRB 050408's afterglow: unextinguished, $\alpha = -0.62$ predicts $\beta_{opt} = -0.08$ (Wind Blue), -0.41 (ISM Blue), or -0.75 (ISM/Wind Red), but none of these can account for the observed steep spectral index of $\beta_{opt} = -1.3$.

The XRT 0.5 – 10 keV x-ray light curve has been normalized to the same time in Figure 3.5 (Capalbi et al. 2006) and has been plotted with the measured x-ray spectral index, $\beta_x = -1.14 \pm 0.19$ (Chincarini et al. 2005). This derived spectral index suffers from moderate uncertainty due to large line-of-sight neutral

hydrogen in the host galaxy. From Figure 3.5 it is clear that the extrapolation of the x-ray spectrum to optical frequencies requires a break between the two ranges during the time of the FUN GRB spectral flux distribution.

By attempting to fit these parameters to the standard model relations, we find the most likely scenario is that with $\nu_{opt} < \nu_c < \nu_x$ in a constant density medium. In this scenario, though, the light curve ought to fade more rapidly than the observed $\alpha_{opt} = -0.63$. This may indicate that other processes are affecting the light curve. Continuous energy injection (Panaitescu et al. 2006, §7.7) may artifically inflate the measured temporal slope, or we may be under-sampling a more complex light curve. If we assume that $\alpha_{opt} = -0.63$ is the true unaltered index, then this yields $p = 1.84$ (ISM-Blue), 1.17 (Wind-Red), or 1.51 (ISM/Wind-Red), and hence requires a more complex parameterization of the electron distribution (Bhattacharya 2001; Nysewander et al. 2005b).

The break observed in the x-ray light curve is likely neither due to a jet break, nor to the passage of ν_c. A jet break will produce a break in the light curve at all frequencies, but the optical afterglow does not show this. For our preferred scenario at $t = 12.25$ hours, and with $\nu_c < \nu_x$, the observed x-ray spectral slope, $\beta = -1.14 \pm 0.19$ implies $p = 2.3 \pm 0.4$ and $\alpha_x = -1.21 \pm 0.29$. This predicted value for α_x closely matches the observed post-break α_x which suggests that the break may have occurred before the SFD was measured at 12.25 hours. This break was previously constrained to $7.3 < t_{break} < 31$ hours by Chincarini et al. (2005). However, there is no corresponding observed change in the x-ray spectral slope as one expects from the ν_c break, β_x would change from -0.64 to -1.14, hence this is also unlikely. In the optical, with $\nu_c > \nu_{opt}$, $p = 2.3 \pm 0.4$ implies $\beta_{opt} = -0.64 \pm 0.19$, which agrees with ISM-Blue. p also implies $\alpha_{opt} = -0.96 \pm 0.29$ for an ISM, which agrees somewhat with the observed temporal index ($\alpha_{opt} = -0.63$), but as mentioned above, this index may be modified by other processes.

3.3 Conclusions

GRB 030115 ($A_V \approx 1.4$ mag) and GRB 050408 ($A_V \approx 0.55$ mag) are two clear examples of gamma-ray bursts whose optical afterglows were suppressed due to source frame extinction. Both bursts lie on the continuum consisting of dim bursts; they are not completely extinguished, but they are indeed somewhat obscured. GRB 050408 lies on one side of this continuum; it was considered a typically bright afterglow, but our analysis shows that even these moderately bright bursts suffer from extinction. GRB 030115 lies on the other end, closer to the fraction of bursts that are completely dark. Certainly we can imagine bursts that lie more deeply enshrouded in clouds that would cause even darker afterglows. Chapter 5 presents two completely dark bursts, GRB 051022 and GRB 060306, for which no optical or near-infrared afterglow was found despite rapid observations. We analyze each burst and find that they are likely dark due to extinction.

Chapter 4

Dark Due to Redshift: GRB 050904

Our discovery of the near-infrared afterglow of GRB 050904 (Haislip et al. 2006b) with measured photometric redshift of $z = 6.39^{+0.11}_{-0.12}$, consistent with the spectroscopic redshift of $z = 6.29 \pm 0.01$ (Kawai et al. 2006), confirmed the presence of the highest redshift gamma-ray bursts. These explosions highlight some of the earliest generations of stars and have the potential to reveal vast amounts of information about the early universe. Now that high redshift GRBs with bright optical afterglows have been shown to exist, observing programs such as ours that are designed to capitalize on this science, with multiwavelength, simultaneous UV to NIR coverage, will likely drive a new era of study, using GRBs as probes of the early universe.

4.1 GRBs as Probes of the Early Universe

In 2000, Lamb & Reichart (hereafter referred to as LR00) first predicted that gamma-ray bursts and their afterglows would eventually replace quasars as the preferred probe of elemental abundances and reionization in the early universe. GRBs are thought to occur at high enough rates at high redshifts:

using numerical simulations and semi-analytic models of the early star-formation rate, both LR00 and Bromm & Loeb (2002) find that $\sim$1/2 of GRBs occur at $z > 5$. GRBs must also be detectable at high redshifts: taking a sample of GRBs with measured redshifts and peak photon number fluxes, LR00 find that due to the extremely high implied luminosities, a large fraction of these would be detectable by the *Swift* satellite even if placed at redshifts corresponding to before star formation is likely have begun. When we take into account the sensitivity of *Swift*, LR00 find that $\sim$1/4 of all detected GRBs should have $z > 5$ (although see Daigne et al. 2006). Lastly, GRB afterglows must be bright enough to be observed at large distances: surprisingly, the observed flux of the soft x-ray, infrared and optical afterglows has little dependence on redshift beyond a $z \approx 3$, due to the counterbalancing effects of distance and cosmological time dilation of the early bright afterglow.

Swift has pushed the boundaries of observable GRBs to higher redshifts than previous missions (see Figure 1.1), indicating that we are still in the regime where observational biases play a role in the detection of distant GRBs. However, the increased sensitivity of *Swift* has already allowed a new era of study of the early universe to begin. GRBs can be used as tools to probe the early universe because:

1. GRBs Map The Cosmic SN Rate

With the now-clear association between long duration gamma-ray bursts and supernovae (e.g. Galama et al. 1998; Bloom et al. 1999; Reichart 1999; Price et al. 2002; Stanek et al. 2003), GRBs are known to trace, at least in some proportion, the most massive star formation (Fruchter et al. 2006), and because of their brightness, they reveal star formation back to some of the earliest generations of stars. Models suggest that the first light in the universe likely occurred between $z \approx 15 - 30$ (e.g., Ostriker & Gnedin 1996; Gnedin & Ostriker 1997; Valageas & Silk 1999; Bromm et al. 1999, 2002; Abel et al. 2000, 2002), which is consistent with the findings of WMAP (Spergel et al. 2003).

2. Cosmic Metallicity History

Related to the star formation history, GRBs complement QSOs by probing the cosmic metallicity history of the universe. Quasars typically reveal the metal-poor halo of galaxies, while GRBs reside deep in the metal-rich denser regions of the disk. By sampling a more metal rich area, limits on metal formation will be stricter than measuring an already metal-poor region. GRBs are greater in number at high redshifts and easier to measure than quasars.

3. Probes of Reionization

GRBs will also replace QSOs as probes of the epoch of reionization beyond the furthest known quasar ($z \approx 6.3$: SDSS 1030+0524; Becker et al. 2001) where a larger fraction of neutral hydrogen causes the Gunn-Peterson trough to be difficult to measure. Because of the intrinsic brightness of bursts, observers also do not have to worry about Lyman α emission from the host galaxy that confuses the continuum. Also, the effect of a GRB on its environment is not expected to be as great as that of a QSO, so if a proximity effect is observed it will likely be due to concurrent star formation.

4. Pinpoints High Redshift Galaxies

High redshift GRBs occur in high redshift galaxies, which are dim and difficult to spot in surveys. A GRB-selected high redshift galaxy is free of some of the observational biases of current high-z galaxy samples. Berger et al. (2006) find that because Lyman α is obscured by dust in the host spectrum of GRB 050904, this galaxy would not have been found in high-z Lyman α surveys.

4.2 The Global Observational Effort

Up until now, observational selection effects have biased the discovery of afterglows to lower redshifts. High redshift afterglows require rapid NIR responses from observers, but until the *Swift* era, GRB localizations were often too broad for the small fields of view of NIR instruments. Most often, infrared measurements were made only after the afterglow was already observed at optical wave-

lengths, which inherently limits the redshift to z < 5 – 6, because of Lyman α forest and Lyman limit dropout. With *Swift*'s arcsecond precision, this is no longer an issue, and the discovery of the NIR afterglow of GRB 050904 with the SOAR Telescope is a prime example.

Swift localized the very long duration ($T_{90} \approx 120$ seconds) GRB 050904 at 01:51:44 UT on September 4^{th}, 2005. *Swift*'s XRT telescope quickly disseminated the coordinates of the x-ray afterglow through the GCN system. Both the robotic telescope TAROT and the Palomar 60" telescope produced constraining optical limiting magnitudes at the site of the afterglow (Klotz et al. 2005a; Fox & Cenko 2006). Haislip et al. (2005d) found emission in the near-infrared, though, and based upon the P60 optical limits they were able to constrain the optical to NIR spectral slope to $\beta < -3.35$, which suggested that the burst lay at $5.3 <$ z < 9 (Haislip et al. 2005c). This estimate was later narrowed to $6 <$ z < 8 (Reichart 2005) based upon a closer inspection of the filter widths, and to z $= 6 \pm 1$ (Haislip et al. 2005b) due to SOAR Y-band observations along with the fact that Klotz et al. (2005b) found emission of an early optical flash in their unfiltered images. A number of groups followed the afterglow as it faded over the next few days. Kawai et al. (2005) observed the afterglow approximately 3.5 days after the trigger when the afterglow was very faint, yet they were able to discern a redshift of z $= 6.29 \pm 0.01$ for the burst.

The collaboration observations are given in Table 4.1 and the detections included in the afterglow model are plotted as solid circles in Figure 4.1. The UNC observations include the SOAR discovery observations and optical limits from PROMPT, but the bulk of the data comes from the large global collaboration organized to track the afterglow.

Table 4.1: Observations of the Afterglow of GRB 050904

Sep 4.0795	2.80 min	R	>18.2	0.30-m BOOTES-1B
Sep 4.0821	6.46 min	R	>18.3	0.30-m BOOTES-1B
Sep 4.0868	13.22 min	R	>19.2	0.30-m BOOTES-1B
Sep 4.0956	25.95 min	R	>19.5	0.30-m BOOTES-1B
Sep 4.1151	53.96 min	R	>19.9	0.30-m BOOTES-1B
Sep 4.1535	109.30 min	R	>21.0	3.5-m Calar Alto
Sep 4.206	3.07 hr	J	17.36 ± 0.04	4.1-m SOAR
Sep 4.213	3.25 hr	J	17.35 ± 0.04	4.1-m SOAR
Sep 4.220	3.42 hr	J	17.61 ± 0.04	4.1-m SOAR
Sep 4.248	4.08 hr	z	>18.8	60-inch Palomar
Sep 4.355	6.66 hr	R	>22.3	60-inch Palomar
Sep 4.366	6.91 hr	[b]	>20.1	0.41-m PROMPT-5
Sep 4.390	7.49 hr	J	18.66 ± 0.15	4.1-m SOAR
Sep 4.402	7.78 hr	K_s	16.77 ± 0.07	4.1-m SOAR
Sep 4.416	8.12 hr	i	>21.1	60-inch Palomar
Sep 4.486	9.79 hr	H	18.17 ± 0.06	3.8-m UKIRT
Sep 4.488	9.86 hr	J	19.02 ± 0.06	3.8-m UKIRT
Sep 4.502	10.18 hr	K	17.38 ± 0.06	3.8-m UKIRT
Sep 4.518	10.57 hr	K'	17.55 ± 0.03	3.0-m IRTF
Sep 4.551	11.35 hr	Z	22.08 ± 0.16	3.8-m UKIRT
Sep 4.565	11.69 hr	J	19.25 ± 0.07	3.8-m UKIRT
Sep 5.198	26.90 hr	Y	20.42 ± 0.26	4.1-m SOAR
Sep 5.246	28.03 hr	J	20.16 ± 0.17	4.1-m SOAR
Sep 5.322	29.87 hr	I_c	>20.2	0.41-m PROMPT-3 + 0.41-m PROMPT-5
Sep 6.30	2.22 day	J	20.60 ± 0.23	4.1-m SOAR
Sep 6.35	2.27 day	Y	20.98 ± 0.34	4.1-m SOAR
Sep 7.21	3.13 day	i	>25.4	8.1-m Gemini South
Sep 7.23	3.15 day	r	>26.5	8.1-m Gemini South
Sep 7.24	3.16 day	z	23.36 ± 0.14	8.1-m Gemini South

[a] Upper limits are 3σ. [b] Unfiltered, calibrated to R.

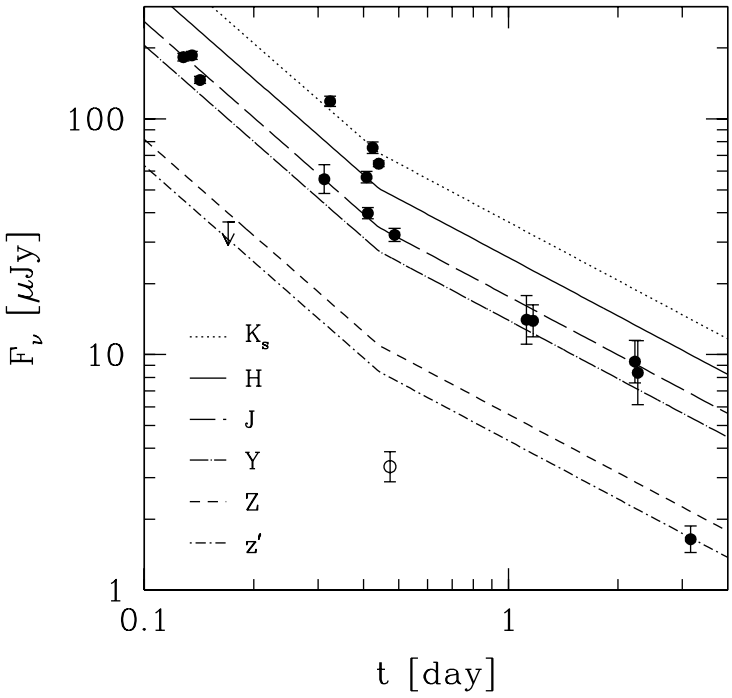

Figure 4.1: All NIR & optical data redward of Lyman α, and our best-fit dual power-law model. The open point is an anomalous Z-band measurement and was not included in the fits. It may be due to absorption of molecular hydrogen in the source frame (Haislip et al. 2006b).

4.3 The Photometric Redshift: $z = 6.39^{+0.12}_{-0.11}$

We fit the standard model to the data in order to constrain the redshift of the afterglow. All magnitudes are converted to fluxes as prescribed by Bessell (1979) and Bessell & Brett (1988). We fit the model to all data in Table 4.1 except for the discrepant UKIRT Z magnitude. This point lies over 3 σ off of the predicted light curve. This filter lies on the edge of the Lyman α break and hence slight inconsistencies between published and real filters and CCD quantum efficiency will affect the predicted light curve for this filter. All model parameters were scrutinized for this filter, though, and the suppression of emission could not be explained. If it is a real feature, it may be evidence for absorption due to

molecular hydrogen in the source frame (Haislip et al. 2006b).

The afterglow is modeled by two components with power-law temporal and spectral slopes α_1, α_2 and β_1, β_2 joined at a time, t_0:

$$F_\nu(t) = e^{-\tau_\nu^{MW}} e^{-\tau_{\nu(1+z)}^{Ly\alpha}} e^{-\tau_{\nu(1+z)}^{source}} F_o \left(\frac{\nu}{\nu_o}\right)^{\beta_n} \left(\frac{t}{t_o}\right)^{\alpha_n}. \quad (4.1)$$

such that for $t < t_o$, n = 1, and $t > t_o$, n = 2. A single power-law fit is ruled out at the 3.7σ credible level. Similar to previous modeling efforts (GRB 021211 §2.3, GRB 030115 §3.1.3, GRB 050408 §3.2.3) F_o is the normalization at t_o, τ_ν^{MW} is the Galactic extinction curve model of Cardelli et al. (1989), $\tau_{\nu(1+z)}^{Ly\alpha}$ is the Lyman α forest absorption model of Reichart (2001a) and $\tau_{\nu(1+z)}^{source}$ is the source frame extinction curve and Lyman limit absorption model of Reichart (2001a). Galactic extinction in this direction is estimated to be $E(B-V) = 0.060$ mag (Schlegel et al. 1998). The data are not able to differentiate between the various scenarios due to degeneracy between the intrinsic spectral slope and extinction, so we set $A_V = 0$ mag for the fits and assume that the observed spectral slope is a combination of both. This equation is integrated against tightly sampled filter transmission tables in order to accurately determine the shape of the spectrum and Lyman α break.

The model is fit using Bayesian inference and a set of prior probability distributions (e.g. Reichart 2001a, Lee et al. 2001, Galama et al. 2003, Nysewander et al. 2005b) and is described in detail in §2.3. We were not able to constrain the early spectral slope from the data, hence we set $\beta_1 = \beta_2$. The values found in the best fit are: $\alpha_1 = -1.36^{+0.07}_{-0.06}$, $\beta_1 = \beta_2 = -1.25^{+0.15}_{-0.14}$, $\alpha_2 = -0.82^{+0.21}_{-0.08}$ and z = $6.39^{+0.12}_{-0.11}$. The light curves of this model are presented in Figure 4.1 and spectral flux distribution is presented in Figure 4.2. Given the steep spectral slope, it is likely that there is source frame extinction present, although we cannot say for certain which of the standard model relations fits best. All scenarios (wind-swept versus ISM, and ν_c above or below ν_{opt}) fit the data equally well, with the only difference being the amount of extinction applied to the spectrum.

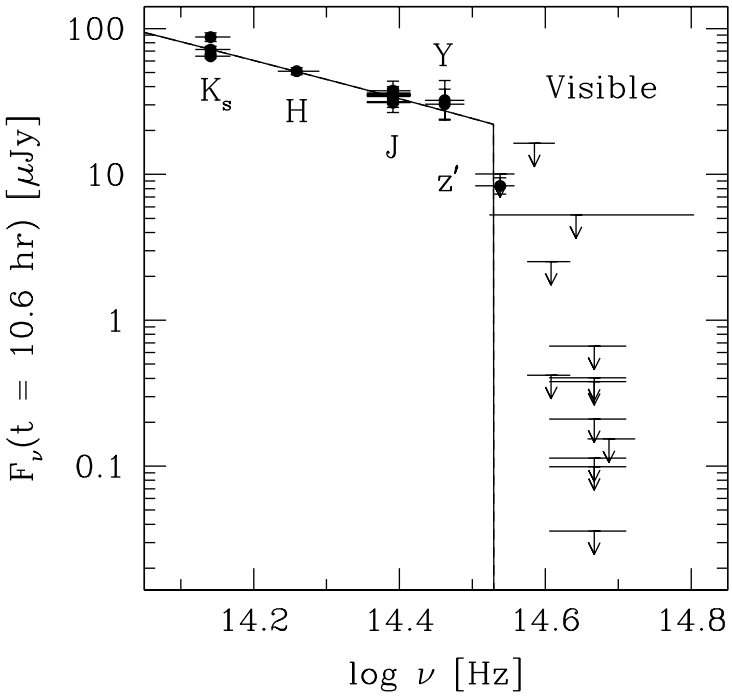

Figure 4.2: The spectral flux distribution of GRB 050904 scaled to 10.6 hours after the burst. The spectrum includes our best fit model where we have set $A_V = 0$ mag and assumed that the observed slope is a combination of intrinsic index along with souce frame extinction. The inclusion of host extinction cannot explain the steep slope blueward of the z filter.

4.4 Conclusions

The discovery of the near-infrared afterglow of GRB 050904 provided clear proof that there is a subset of gamma-ray bursts that lack optical afterglows due to their high redshift. Only with rapid, deep, near-infrared observations are we able to find these elusive bursts, and because of this, the sample of high-z GRBs suffers from extreme observational bias. For years, astronomers have chased GRB afterglows with easily accessed optical telescopes, and only after discovering an afterglow, have performed near-infrared observations. With a problem so difficult to quantify, it is hard to gauge the effect on the distribution of redshifts. The arcsecond localizations provided by *Swift* lessen this bias though, and many more

near-infrared observations are made at early times. We can see this influence in the mean redshifts of the pre and post *Swift* era: $\bar{z} = 1.3$ versus $\bar{z} = 2.6$ (see Table 1.1). Other factors play into this difference though, previous satellites had different high energy responses and lower sensitivity.

Gamma-ray bursts can be some of the brightest events, and their emission can be caught with even small telescopes, although they can lie far across the observable universe. With rapid-time follow-up and identification of afterglows, in the future we can obtain same night, high signal-to-noise spectra of these distant objects and glean information about the early universe. With PROMPT's upcoming near-infrared coverage and data pipeline, it will be able to rapidly identify these high redshift GRBs through Lyman α dropout and alert the GRB community to the important events.

Chapter 5

Two Dark Bursts: GRB 051022 & GRB 060306

By definition, the study of completely dark GRBs is difficult. Without an optical afterglow, we have no means of deducing the true source frame extinction, redshift or physical properties of the environment. This is why we often examine dim bursts when we study the effects that may cause darkness. If an x-ray or radio afterglow is found it can help to constrain the underlying synchrotron spectrum and environmental effects. Precise x-ray or radio localizations can often pinpoint the host galaxies of GRBs, although we must be circumspect with identifications because the possibility always exists of a galaxy coincidentally being within the localization.

The *HETE-2* GRB 051022 and *Swift* GRB 060306 are clear examples of dark bursts. Extrapolating the x-ray afterglow and optical and NIR upper limits to 11 hours (as in Figure 1.2) we find broadband spectral slopes of -0.30 and -0.18 respectively, well above the defined limit of Jakobsson et al. (2004). In the case of GRB 051022, an identified host galaxy and column densities derived from the high-energy spectra show that the burst is likely completely enshrouded by dust in a giant molecular cloud. For GRB 060306, only a handful of bursts have equally constraining limiting magnitudes. The cause for the extreme darkness

is unclear, but it also is likely obscured by many magnitudes of extinction at moderate redshift.

5.1 GRB 051022

GRB 051022 is a unique burst because it shows very clear, extremely high neutral hydrogen column densities of $N_H = 5.0 - 8.8 \times 10^{22}$ cm^{-2} (Rol et al. 2006a; Nakagawa et al. 2006) in its x-ray spectra. These values are among the highest ever observed in GRB spectra. From detections of an x-ray and radio afterglow, a host galaxy was found that was not at high redshift (z = 0.8 Gal-Yam et al. 2005). No optical afterglow was discovered, despite a deep and thorough search in the optical and near-infrared at early times. Based on the definition of Jakobsson et al. (2004), it is clearly a dark burst, with an optical to x-ray spectral index of $\beta > -0.30$. If we infer values for the optical extinction from the column density, then we expect A_V to be between 51 and 71 magnitudes assuming that the burst or afterglow did not destroy most of the line of sight dust.

5.1.1 Observations

HETE-2 detected the extremely bright and long (t $\approx$ 190 seconds) GRB 051022 at 13:07:58 UT on October 22nd, 2005, and after 45 seconds, disseminated the coordinates of a 14 arcminute WXM radius error circle and at 119 seconds distributed SXC coordinates of the smaller 2.5 arcminute radius localization (Tanaka et al. 2005; Hurley et al. 2005; Nakagawa et al. 2006). An early spectral fit to the *HETE-2* WXM & FREGATE data indicated that the burst has extremely high N_H column density: $N_H \approx 2 \times 10^{22}$ cm^{-2} (Doty et al. 2005).

At 3.5 hours after the burst, *Swift*'s XRT observed the localization and found a bright, fading x-ray afterglow that localized the burst to 4 arcseconds (Racusin et al. 2005a). The afterglow faded with $\alpha_x = -1.33 \pm 0.07$, and an analysis of

the XRT spectrum found $N_H \approx 1 \times 10^{22}$ cm^{-2}. At 2.9 days, the XRT afterglow breaks to a steep slope of $\alpha_x = 3.6 \pm 0.4$. If this is the jet break it implies $E_{iso} = 3.5 \times 10^{53}$, the opening angle of the jet, $\theta = 4.3^o$, and $E_\gamma = 1.1 \times 10^{51}$ (Racusin et al. 2005b). *Chandra* also observed the x-ray afterglow and constrained the localization to 0.7 arcseconds (Patel et al. 2005).

A deep and rapid response by the GRB follow-up community did not produce an afterglow optical or NIR afterglow. Four telescopes responded to the GCN alerts within minutes: ART (Torii 2005c), ROTSE-III (Schaefer 2005), the University of Miyazaki 30-inch (Sonoda et al. 2005) and the SSRO 40-inch (Cenko et al. 2005b) but none found any evidence for optical emission. A red, extended galaxy was within the XRT error circle, and Cameron & Frail (2005) discovered a radio afterglow that identified it as the host galaxy. Gal-Yam et al. (2005) found a redshift of z = 0.8 using the Hale telescope at Palomar Observatory.

UNC observed the field with the SOAR telescope in J and K_s beginning 11.2 hours after the burst (Nysewander et al. 2005a). We detected no variability in the host galaxy of GRB 051022 between the beginning and end of our observations (11.2 and 14.4 hours). We reobserved the field the next night, and an image subtraction on the two epochs rules out any variable afterglow to $J = 20.1$ and $K_s = 18.7$. The data were reduced in IRAF and flat field corrected using an image derived from the science data. Aperture photometry was performed using DAOPHOT and was calibrated to magnitudes of stars in the 2MASS catalogue. With Gemini South, our collaboration observed the field at 12.7 and 13.0 hours in R and Z, and an image subtraction in these filters yielded no variability down to $R > 24.0$ and $Z > 22.5$ (Rol et al. 2006a).

5.1.2 Discussion

GRB 051022 is clearly dark. Using the most constraining limiting magnitude of Cenko et al. (2005b), and assuming $\alpha_{opt} = -1.0$ with the measured x-ray flux and temporal slope of Butler et al. (2005a), we find an optical to x-ray spectral

index of $\beta > -0.30$. Figure 5.1 plots the broadband spectrum of GRB 051022. The data are scaled to 12 hours post-burst, using a temporal index of $\alpha = -1.0$. The *Chandra* x-ray spectrum is adopted from Rol et al. (2006a). The possibility exists that a break occurs between the high and low energy emission, but no standard model synchrotron break can explain the enormous disparity between the two regimes.

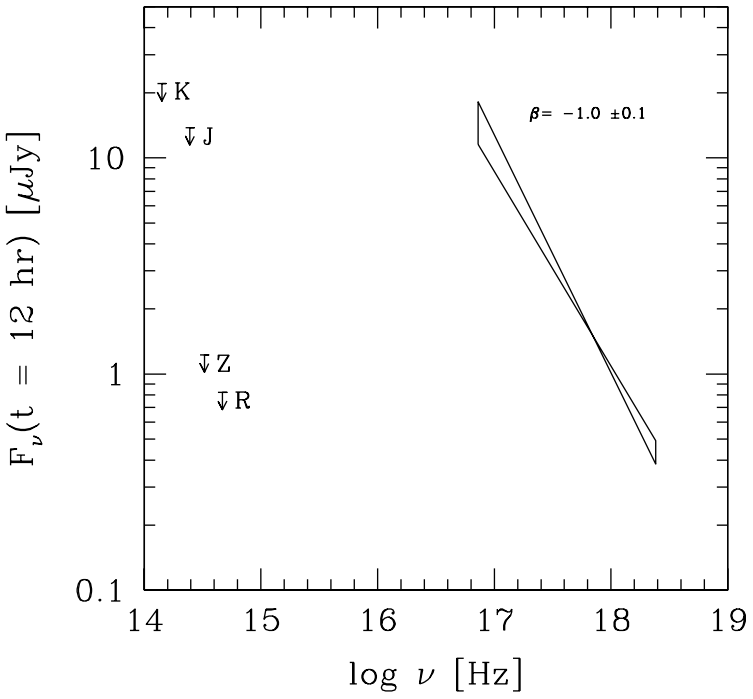

Figure 5.1: The broadband spectral plot of GRB 051022. The *Chandra* unextinguished x-ray spectrum ($\beta_x = -1.0 \pm 0.1$; Nakagawa et al. 2006; Rol et al. 2006a) is plotted along with the SOAR, Gemini and WHT $RZJK$ limiting magnitudes scaled to 12 hours. Optical observations have been scaled using the typical optical decay index of $\alpha_{opt} = -1.0$.

The previously measured Galactic neutral hydrogen column density along this line of sight is 4.9×10^{20} cm^{-2} (Dickey & Lockman 1990). If the excess neutral hydrogen observed by *Chandra* and *HETE-2* is from a previously unobserved overdensity located within or close to our Galaxy, then we can simply use the

relation found by Predehl & Schmitt (1995): $A_V = 0.56 \times N_H$ [10^{21} cm^{-2}] + 0.23 mag. Rol et al. (2006a) find that for the *Chandra* spectrum, $N_H = 1.08 \times 10^{22}$ cm^{-2} that gives $A_V = 6.3$ mag. In the *HETE-2* spectrum, Nakagawa et al. (2006) find $N_H = 1.51^{+0.53}_{-0.50} \times 10^{22}$ cm^{-2} hence $A_V = 8.7 \pm 0.3$ mag.

It is most likely that the excess column density is located within the host galaxy of GRB 051022. The source frame N_H is given by the observed $N_H \times (1 + z)^{2.6}$ (Morrison & McCammon 1983). Using z = 0.8, in this case, $N_H = 5.0 \times 10^{22}$ cm^{-2} (*Chandra*) and 7.0×10^{22} cm^{-2} (*HETE-2*). Host $A_V = A_{V obs} \times (1 + z)$ mag, so for the two measurements we find the enormous estimates of $A_V = 51$ (*Chandra*) and $A_V = 71$ magnitudes (*HETE-2*) in the rest frame. Using the extinction law of Cardelli et al. (1989) ($F \propto \nu^{1.6}$), $A_K = 5.8$ (*Chandra*), 8.0 (*HETE-2*) mag.

Clearly, under these conditions it would be unlikely to see an afterglow but these estimates assume a Milky Way type environment. Using the small dust to gas ratios of Pei (1992) for the Large and Small Magellanic Clouds, for an LMC environment, $A_K = 1.2$, 1.7 mag, and for SMC, $A_K = 0.6$, 0.9 mag for *Chandra* and *HETE-2* respectively. Any estimate of the optical extinction from the measured N_H absorption will depend highly on the assumed dust to gas ratios, which are uncertain. Also, the burst and afterglow likely change the environment close to the progenitor, and so we may find atypical properties of the dust and gas.

5.2 GRB 060306

GRB 060306 was a truly dark burst that we observed with both PROMPT on the rapid-timescale in *ri* and with deep imaging with SOAR in the near-infrared. The deep SOAR K_s imaging combined with K_s observations from our collaborators places strict limits on variability in the XRT localization. A possible bright host galaxy was detected but it is unclear if this is a galaxy or

a field star. Because our limits lie in the $K_{\rm s}$ filter, the burst is unlikely to be dark due to high redshift, and because of the deep ri limits, it is unlikely dark merely due to an usually steep temporal slope. The measured value of N_H from the x-ray afterglow is high for a GRB, and it implies $A_K \approx 23$ magnitudes of extinction assuming the mean *Swift* GRB redshift.

5.2.1 Observations

Swift located the long ($t_{90} \approx 30$ sec), bright burst, GRB 060306 at 00:49:10 UT on March 3^{rd} 2006. Immediately, *Swift*'s XRT slewed onto the site of the burst and found a bright x-ray afterglow that pinpointed the location to an $11''$ diameter region (Angelini et al. 2006). The afterglow faded steeply with $\alpha_x \approx -3.3$ for 3.5 minutes when it broke to a slope of $\alpha \approx -0.6$ (Page et al. 2006b). UVOT did not see an afterglow on the rapid timescale down to $V \approx 18^{th}$ magnitude and to $V \approx 20.1$ after stacking all observations during the first day (de Pasquale & Angelini 2006).

UNC optical observations began only 49 seconds after the burst with PROMPT ri responding on the rapid-timescale. These observations are summarized in §7.4 and the results are presented in Table 7.4. In deep images only one source is present in the error circle, but it is also well-detected in archived catalogue images. It is uncertain if this object is an unrelated field star or a possible host galaxy. The source was detected by Price et al. (2006) in RIJ ($R \approx 20.7$) with the MANGUM telescope, and did not appear to be fading.

Chen et al. (2006) observed the field with the 3.5-m ARC at 1.6 hours in $K_{\rm s}$ and measured a magnitude of $K_{\rm s} = 17.8 \pm 0.1$ for the object, and a limiting magnitude of 19.5 was derived for the field (Lamb et al. 2006). We triggered a Target of Opportunity observation with the 4.1-m SOAR telescope (Nysewander et al. 2006e) in $K_{\rm s}$ beginning 1.0 days after the burst and found a magnitude of $K_{\rm s} = 17.5 \pm 0.2$, and a limiting magnitude of 18.4 for the field. The images were reduced using CCDPROC and photometered using psf-fitting photometry using

DAOPHOT in IRAF. Both the ARC and SOAR images were calibrated to the same 2MASS field stars. A psf-matched field subtraction does not show signs of variability between the ARC and SOAR images.

5.2.2 Discussion

If the source and the GRB are unrelated, then we can cite the limiting magnitude of the ARC images, $K_s = 19.5$, as the limiting magnitude at 1.6 hours. But if the source is the host galaxy, we can only measure variability of the host to the limiting magnitude of the SOAR image, $K_s = 18.4$. Both K_s limits along with the most constraining PROMPT rapid ri limits from Table 7.4 are plotted in Figure 5.2. The data are scaled to 1.6 hours using the typical afterglow index of $\alpha_{opt} = -1.0$. The unabsorbed x-ray flux is scaled using the observed x-ray slope $\alpha_x = -0.6$ (Page et al. 2006b) and is plotted along with the x-ray spectral index.

Spectroscopy of the potential host galaxy is needed to determine if it is in fact a galaxy or simply a field star. Without knowing this we cannot say with certainty why the burst is dark. We can speculate on the likely causes:

Redshift

Due to the K_s-band imaging, we can with near-certainty rule out redshift as the primary cause for the darkness of the afterglow. A standard afterglow would have to lie at z > 17 to be undetected in K_s. Redshift may affect the deeper PROMPT ri limits, though, so we must take care in the analysis of the burst.

Break between the optical and x-ray

A break may occur between the optical and x-ray, although from Figure 5.2 we can see that even a flat spectrum between the optical and x-ray cannot explain the deep PROMPT ri limiting magnitudes. r and i are more likely to be highly

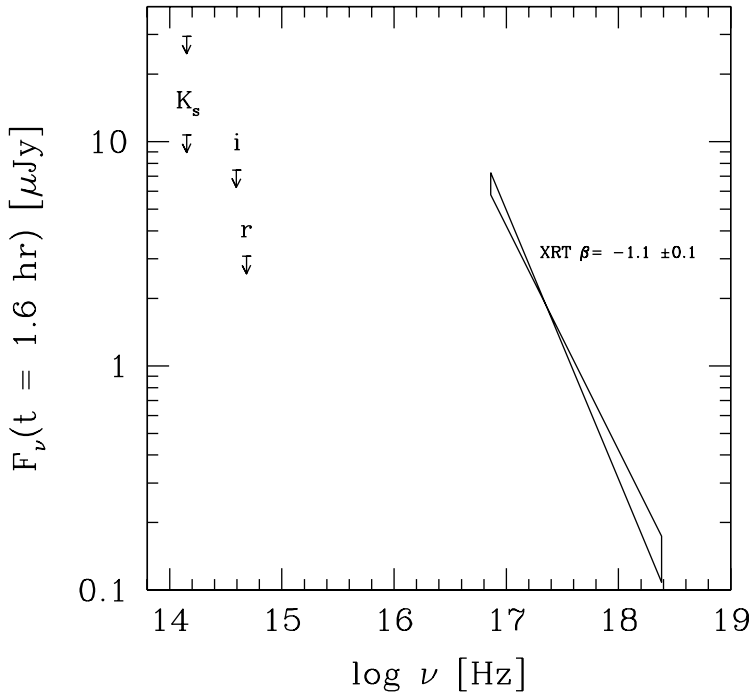

Figure 5.2: The broadband spectral plot of GRB 060306. The *Swift* XRT unextinguished x-ray spectrum ($\alpha_x = -0.6$, $\beta_x = -1.1 \pm 0.1$; Page et al. 2006b) is plotted along with the most constraining PROMPT limiting magnitudes and the early ARC K_s observation (Chen et al. 2006; Lamb et al. 2006). The x-ray spectrum has been scaled to 1.6 hours using the observed x-ray temporal index $\alpha_x = -0.6$. Optical observations have been scaled using the typical optical decay index of $\alpha_{opt} = -1.0$.

extinguished or absorbed due to redshift, though, so if we neglect the optical limits and focus instead on the NIR, then a flat spectrum between 14.151 log GHz and 16.861 log GHz is consistent with the data but is not consistent with the standard model scenarios. It is possible that the break occurred in the low energy portion of the x-ray spectrum, but was confused by the large value for N_H. A simple break to an extreme shallow spectral slope could explain the deep NIR limits, but it is unlikely that this is the sole cause of the very dark afterglow.

Could this be the cooling break? It is uncertain. $\beta_x = -1.1$ implies that p = 2.2 (ISM/Wind - Red) or 3.2 (ISM/Wind - Blue), hence it is likely that $\nu_c < \nu_x$

at this time. If this is the case, then $p = 2.2$ implies $\alpha_x = -1.2$, not the observed $\alpha_x \approx -0.6$. But also, β below the cooling break would be -0.6, which is not shallow enough to explain the broadband morphology.

Extinction

GRB 060306 had an observed neutral hydrogen host column density of $N_H = 4 \times 10^{21}$ cm^{-2} in addition to the previously detected Galactic $N_H = 3.6 \times 10^{20}$ cm^{-2}. This places GRB 060306 in the top 25% of all *Swift* bursts with reported N_H. There is often confusion between attributing extremely high Galactic values of N_H to the host galaxy (Beardmore et al. 2006; Pagani et al. 2006), so this percentage should be taken as a lower limit.

Using the same method outlined for GRB 051022, we find that

$$A_K = 0.56 N_{Hobs} (1+z)^{3.6} \left(\frac{\nu_K}{\nu_V} \right)^{1.6} \tag{5.1}$$

For $N_H = 4 \times 10^{21}$ cm^{-2}, $A_K = 0.25\ (1+z)^{3.6}$. For the median redshift of a *Swift* GRB, $z = 2.5$, $A_K = 23.1$ magnitudes of extinction. Even if the host were at a lower common redshift of $z = 1$, $A_K = 3.1$ magnitudes. If we place the constraint that the host $N_H < 10^{23}$ cm^{-2}, which is the typical upper limit for molecular clouds, then the $z < 2.4$. Just as for GRB 051022, the estimate is dependent on the composition of the interstellar medium and progenitor environment of the host, but it is likely that a combination of moderate redshift and extinction played a role in the nondetection of an afterglow for GRB 060306.

Chapter 6

PROMPT Design & Instrumentation

PROMPT (Panchromatic Robotic Optical Monitoring and Polarimetry Telescopes) is series of robotic telescopes that are uniquely designed to rapidly observe gamma-ray burst afterglows at multiple wavelengths. PROMPT not only produces highly sampled light curves but also information about the spectral properties of the optical afterglow. It is important to note that these observations are simultaneous: important information is lost at early times if the telescope switches between filters when the light curve may be undergoing small-scale variability. PROMPT will cover the wavelength range from 300 to 1700 nm and will include a polarimeter to test the proposed hypothesis that the very early emission is highly polarized (Coburn & Boggs 2003; Rutledge & Fox 2004).

The construction philosophy behind PROMPT is to use commercial hardware and software that is readily available and less expensive than custom designed and built items from manufacturers. Our experiences at PARI (Pisgah Astronomical Research Institute) with the López-Morales & Clemens (2004) Pisgah Automated Survey taught us that products available in the high-end amateur astronomy market are sufficient to produce professional results. PROMPT will consist of six 0.41-m Ritchey-Chrétien telescopes on rapidly-slewing German Equatorial

mounts, five of which use back-illuminated CCD cameras while the sixth will use an LN2 cooled near-infrared camera. Each system has been optimized to observe in a specific region of the optical/NIR spectrum. The polarimeter will be installed and commissioned on one of the five optical telescopes.

6.1 Science Objectives

The strength of quick multi-band photometry is that we will rapidly and accurately determine the temporal and spectral properties of the afterglow. In PROMPT's final stage, we will be able to reconstruct the full $ugrizYJH$ spectral flux distribution of the afterglow. A single telescope moving through filters while observing a variable and ill-behaved afterglow gives an incomplete description. With each filter change, an observer can not disentangle changes in brightness from changes in filters. Barring chromatic effects, we will be able to fully characterize the light curve because we will have many telescopes that will image in a single filter and so will produce a complete description of the temporal behavior of the afterglow. Using this information, we can reconstruct the full picture of the afterglow's spectral behavior.

Photometric Redshifts

Theoretically we will be able to determine the photometric redshift of a GRB to z $\approx$ 12 if the Lyman α cut-off lies between the H and J filters. A bright detection in one filter, with nondetections in seven others could be PROMPT's greatest discovery. In its current optical form, PROMPT can fit photometric redshifts to z $\approx$ 6. Redshifts of $6 <$ z < 12 would seem to be difficult to catch with 16" telescopes, but as Lamb & Reichart (2000) found, the counter effects of time dilation (the effect of viewing an earlier, brighter portion of the light curve) and distance balance each other to produce a relatively bright afterglow. Beyond z $\approx$ 3, distance has only a small effect on brightness. In fact we see this effect

in the afterglow of GRB 050904 (§4). This burst shows signs of a bright early phase – a possible reverse shock – which would normally last only a few minutes, but in this case, due to time-dilation it lasted nearly thirty minutes (Boër et al. 2006).

Extinction Curves

Extinction produces a clear curvature in the spectrum and suppresses blue light preferentially. Although it is possible to see curvature in an optical spectral flux distribution, without near-infrared coverage, there are large uncertainties in differentiating between an intrinsically steep spectral slope and an extinguished source. When the NIR telescope comes online, PROMPT will be able to independently fit extinction curves, but until then, we rely on NIR observations through programs on SOAR, Gemini or through collaborators. Because one needs to be able to identify a single point source to measure an extinction curve, they have not been measured outside of the local group. PROMPT is able to do this, not only outside of our local group, but to high redshift. And, with high redshift, we can not only probe the evolution of circumburst dust properties, we are able to regularly measure extinction curves in the source-frame UV wavelengths, where new data are sparse.

Reverse Shocks

Observations of afterglows tens of minutes to days after the burst over the past decade have supported the standard model of Meszaros & Rees (1993). The external "forward" shocks are well understood, but PROMPT hopes to break ground with observations of bright "reverse" shocks. Only twice in the past decade, observers have caught definite flux from the reverse shock: GRB 990123 (Akerlof et al. 1999) and GRB 021211 (Fox et al. 2003a; Li et al. 2003; Nysewander et al. 2005b; §2). Possible reverse shocks include the early emission seen in GRB 050525 (Blustin et al. 2006), and GRB 050904 (§4, Boër et al.

2006. No one has yet measured spectral parameters or performed polarimetry of a reverse shock. One goal of PROMPT is to break new ground and do both of these. At these extreme early times, with a reverse shock we may see signs of changing extinction curve patterns as the jet sublimates and fragments the dust along its line of sight.

Chromatic Variations

Significant chromatic variations were seen in GRB 021211 (§2, Nysewander et al. 2005b) and similar variations were seen in PROMPT's observations of the early afterglow of GRB 060908 (§7.9: Figure 7.6). With this, PROMPT delves into a new regime. No automated rapid-response GRB dedicated telescope has attempted to provide spectral information at early times. No follow-up effort at all observes in multiple wavelengths *simultaneously* as PROMPT does. In all highly sampled afterglows, small-scale variations are common, and without simultaneous observations in multiple filters, one cannot have a full picture of the behavior of the afterglow. With simultaneous, multi-wavelength coverage, PROMPT is the only current program that can explore these possibilities.

Supplementary Science and Outreach

PROMPT is a GRB dedicated facility, but while not chasing GRBs, a large portion of its time will be devoted to non-GRB science and public outreach. PROMPT's GRB filters are $ugrizYJH$, but we also have available standard Bessell $UBVRI$ and *Red*, *Green* and *Blue* filters designed for use in amateur astronomy. PROMPT has already been used by a number of astronomers at colleges and universities across the state of North Carolina. Morehead Planetarium and Science Center is conducting a K-12 outreach program where students can use a basic online tool to observe selected interesting targets. Hundreds of students across the state have already used PROMPT in their classrooms.

6.2 Design Considerations

Timing of Operations

Swift's first successful detection of a gamma-ray burst was on December 17^{th}, 2004, and the same day the first PROMPT telescope began operations. This was not a coincidence – PROMPT was planned to commence operations with the arrival of the satellite. Because of the speed needed to match this timeline, PROMPT was built in two phases. Phase I was planned early, to match *Swift*, and also cheaply, because at this time the project was only funded by UNC and private donors to a total of $345,000. Phase I consisted of four inexpensive commercial optical telescopes and two new mounts to add to the older model mounts that were used at PARI. Implementation of Phase II began when funding was secured from NSF. Phase II consists of PROMPT in its current form, four optical telescopes, along with the eventual addition of the NIR camera (2007) and polarimeter (2006).

Location

PROMPT is located on Cerro Tololo at CTIO. Figure 6.1 presents a log of observing conditions beginning with December 2004, and is based on archived data from the CTIO website. During most months of the year, PROMPT enjoys predominantly photometric nights, but during the Chilean winter, most nights are non-photometric (although usable) or completely cloudy. Not only is this a site with fine observing conditions but it is also located near to the UNC-led 4.1-m SOAR Telescope. The proximity of the PROMPT site was planned so that observing conditions would be the same for both facilities. PROMPT can track afterglows for hours to faint limits, but larger aperture telescopes are needed to track them further and measure magnitudes days after the event. SOAR imaging can also complement PROMPT in JHK in PROMPT's current form, and with K-band imaging in PROMPT's final form.

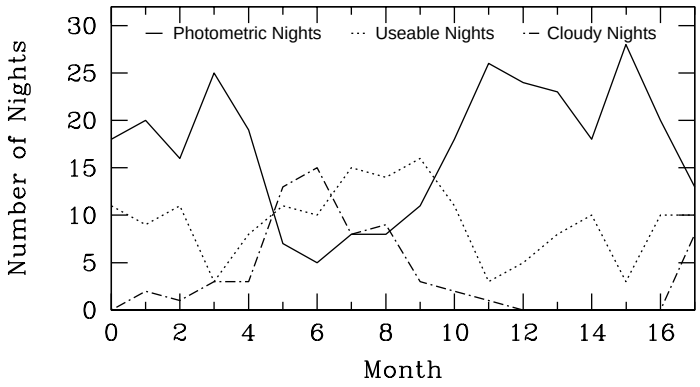

Figure 6.1: The weather information at CTIO starting in December 2004, the beginning of PROMPT operations. This information was gathered from archived weather information given on the CTIO website.

System Speed

The goal of PROMPT is to observe the early afterglows of gamma-ray bursts, and so it is important that the system respond quickly to GRB triggers and rapidly begin imaging. PROMPT is alerted via the GCN socket system, which is the most rapid of the methods of responding to GRB triggers. The mounts can slew rapidly, although their German Equatorial design causes a greater lag in movement than a standard fork mount. Once the mount arrives at the GRB field, observations must begin immediately and the cameras must have a short read out time in order to minimize the delay between exposures.

Robustness

It is important that the system be robust to reduce downtime in general, but also to reduce the added downtime involved in remotely fixing hardware problems. Troubleshooting remotely is difficult and many times impossible without communication and help from CTIO support personnel. The technical staff at CTIO is necessary for helping in this process, but the back-and-forth of e-mail conversation can cause a one hour project to last days. Using widely used and tested high-quality commercial hardware has helped in this endeavor.

Automation

The PROMPT hardware is controlled by a suite of commercially available programs that interface via ActiveX controls with an automation program called *Terminator*. Each Terminator is linked to a central program, *SkyNet*, which controls the entire global network of telescopes. Consideration was given when choosing PROMPT hardware in order to ease the automation process.

6.3 Hardware

Commercial "off-the-shelf" hardware has four important qualities: (1) it is much cheaper than custom designed and built pieces, (2) is it easily and quickly available, (3) it has been tested over many years by many users and hence is engineered to be more reliable, and (4) a manufacturer with a larger consumer base will have a stronger emphasis on customer support.

The prototype for PROMPT, the Dark Burst Telescope (DBT), was developed at PARI in 2003 and 2004. The DBT was largely based on the same design as the Pisgah Survey Telescope (López-Morales & Clemens 2004) which consisted of the same mount, a Paramount GT1100s, a similar telescope, a Meade f/10 12-inch, and was controlled by the same suite of Software Bisque telescope software: TheSky, TPoint and CCDSoft. The main feature of the DBT is that it used

a thermoelectrically cooled Indigo Systems Alpha InGaAs near-infrafed camera that covered $0.9 - 1.68\ \mu$n. The near-infrared coverage was unique among robotic GRB follow-up telescopes at the time, but it was not able to rapidly observe a gamma-ray burst before it was decommissioned in September 2004 due to the beginning of construction of PROMPT.

Figure 6.2: The Dark Burst Telescope at Pisgah Astronomical Research Institute, which is located in the mountains of western North Carolina.

Construction on the PROMPT enclosures began in September 2004 and the hardware has been assembled in three trips that occurred in December 2004, March 2005, and December 2005. During the commissioning phase (that ended January 2006) PROMPT has had anywhere from one to five telescopes operational at a time. Hardware failures, planned outages or upgrades to the system

have caused one or more telescopes to be temporarily non-functioning at any given time.

The first trip was timed to match the beginning of *Swift* operations. As of that time, we had procured the hardware to set up two functioning telescopes. March 2005 saw the completion of a third telescope, the UV optimized, but due to a camera defect that did not appear until after two months of regular operation, this third telescope was taken offline. After the December 2005 trip PROMPT temporarily had five fully functioning telescopes. Since December 2005, we discovered that three cameras had additional manufacturing defects and were all in need of repair, which caused more downtime. A fifth camera was eventually sent back to UNC to be tested with the polarimeter, leaving PROMPT in its current form of four functioning telescopes.

Telescopes

RC Optical Systems provided the six 16-inch Ritchey-Chrétien optical tube assemblies utilizing optics designed and manufactured by Star Instruments. Each set of mirrors were individually coated to enhance reflectivity in the telescope's primary wavelength range, with coatings peaking at 356, 483, 696, 780, 910, and 1327 nm. The focal ratios of the telescopes (optical: f/11.26; NIR: f/17.32) were chosen to provide optimum fields of view (optical: $10'$; NIR: $5'$). The carbon-fiber truss design reduces both wind load on the mount and thermal expansion that enhances its ability to maintain focus. The ambient temperature and the temperatures of both the primary and secondary mirrors are constantly monitored and the mirror temperature is regulated using cooling fans. Maintaining thermal equilibrium between the mirror and its environment is important in eliminating distortion due to air currents.

PROMPT originally was to consist of 3 24" telescopes, which was then scaled to 4 20", but when factoring in load considerations on the mounts, (16": 89 lbs vs. 20": 150 lbs) the added aperture did not outweigh the lessened stability

Figure 6.3: The PROMPT 2 Telescope overlooking the Andes. (Photo by Aaron LaClyuze)

of the system. However, throughout the incarnations of PROMPT design, its combined approximate 1-meter aperture remained a constant. The possibility of autoguiding was explored, but dismissed as an alternative to reducing aperture size due to the difficulty of remote automation. RCOS is currently developing an automated guiding system designed specifically for their telescopes that may be implemented within the next year on the PROMPT telescopes. Guiding will greatly enhance the tracking of the system that will improve the point-spread function and depth of imaging.

PROMPT Phase I used 3 14" f/11 Celestron telescopes, along with one 12" f/10 Meade telescope. Although these produced research-quality data from De-

cember 2004 to December 2005, they had drawbacks. Thermal expansion of the tube assembly caused the focus to be highly dependent upon ambient temperature, and so it was difficult to maintain tight focus during a night of observing. Hysteresis in the focus mechanism made implementing an automated focusing routine impossible. In fact, because the focusing process depended on moving the primary mirror, the pointing of the telescope could change by arcminutes depending on the focus setting. Additionally, the optics were also of a much lesser quality than those of the current telescopes.

Cameras

PROMPT's five optical cameras are Apogee Instruments Inc. Apogee Alta U47+ model cameras with back-illuminated 1024 × 1024 pixel E2V CCDs. Just as the telescope optics are enhanced for a given wavelength, the CCDs are as well: one is UV optimized that extends the quantum efficiency curve of the chip to include the 200 – 350 nm wavelength range, three are midband coated, which enhances sensitivity uniformly across the spectrum (≈400 – 900 nm), and the remaining is broadband coated which improves the sensitivity from 300 – 500 nm (See Figure 6.5). Given the f/11.26 focal ratios of the telescopes and the 13 μm pixel size, the plate scale is 0.59 arcsec per pixel, giving exactly a $10' \times 10'$ field of view. The cameras have short read-out times of $\approx 1 - 2$ seconds, which is highly desired for the short early exposures of the GRB sequence when the afterglow will be fading rapidly and each second on sky is precious.

PROMPT's near-infrared camera is a Rockwell Scientific MicroCam, which is the closest LN2-cooled HgCdTe instrument resembling an "off-the-shelf" item in accordance with the design philosophy of PROMPT. The PICNIC focal plane array is identical to the NICMOS3 instrument and has a size of 512 × 512 pixels with a 40 μn pixel size, which when on an f/17.32 telescope results in a plate scale of 1.17 arcsec per pixel and an exact $5' \times 5'$ field of view. Future plans for the instrument are to replace the bulky LN2 system with a Helium closed

loop system that will require less maintenance and will put a smaller load on the mount. Currently the MicroCam is being tested at UNC and will have control software written for it for during the next 4 – 6 months after which it will see first light at CTIO.

Figure 6.4: UNC's Rockwell Scientific Microcam NIR Camera. (Photo by Aaron LaClyuze)

Filter transmission curves are given in Figures 6.5 – 6.6. The primary GRB filter set is the *ugriz* SDSS (Sloan Digitized Sky Survey: York et al. 2000) filter set (Figure 6.5) that was purchased from Barr Associates. It is a broad-band AB magnitude system of filters based on the Thuan-Gunn set and was defined specifically for the SDSS by Fukugita et al. (1996) (see also Gunn et al. 1998). The J & H near-infrared filters were purchased from Barr Associates but Omega Optical provided the Y filter (Hillenbrand et al. 2002), which, although not commonly used, fills an important gap (0.97 – 1.07 μn) in the filter sequence between z and J. NIR filters are presented in Figure 6.6. Additional PROMPT optical filters that were purchased from Omega Optical: Bessell $UBVRI$, and from Andover Corp.: Kron-Cousins RI.

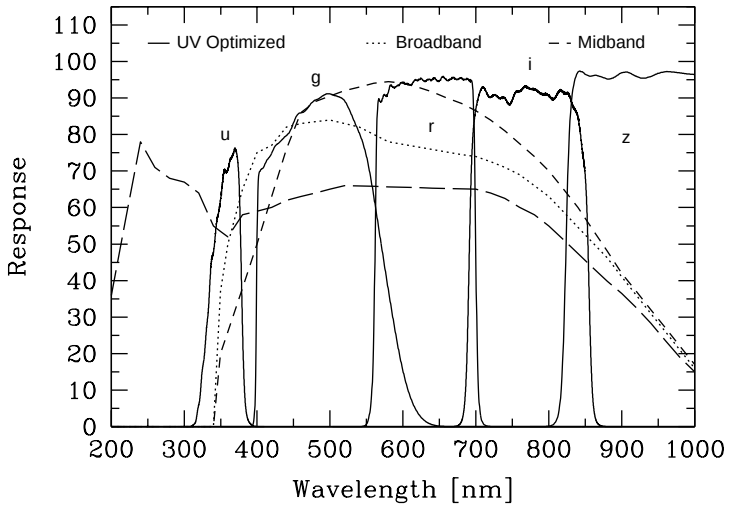

Figure 6.5: The *ugriz* filter profiles were supplied by Barr Associates. Camera quantum efficiencies were adapted from Apogee Instruments Inc. documentation.

Mounts

The mounts are the third vital piece of hardware needed for research quality imaging. The only off-the-shelf commercial mount with the necessary specifications is the German Equatorial Software Bisque Paramount ME. The Paramount GT1100s that was used at PARI is an earlier version of this mount. The ME satisfies all of the main priorities for fast, automated GRB follow-up: (1) it has rapid slewing capability of up to a few degrees per second, (2) it has pointing accuracy of less than 1-2 arcmin, which ensures that PROMPT will cover the early 3 arcmin radius *Swift* BAT localizations, (3) it has a large right ascension gear for accurate tracking and reduced period error (less than 5″ peak-to-peak), and (4) it seamlessly interacts with TheSky software that is easily scripted for automation. It is designed to perform to these specifications under a payload of

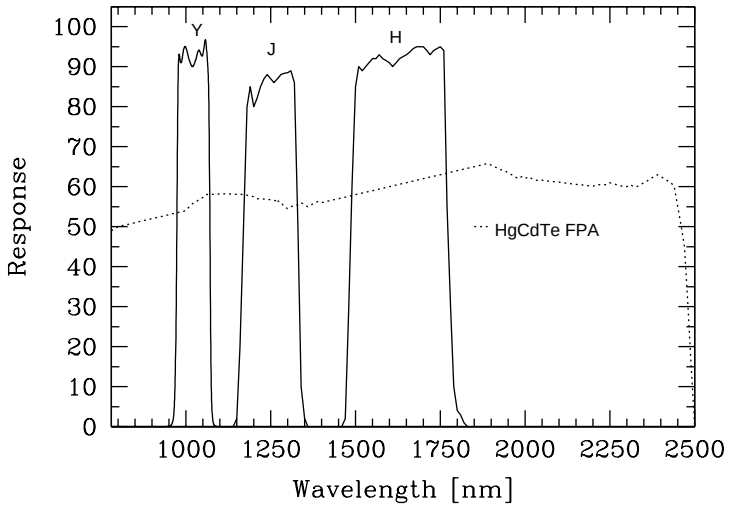

Figure 6.6: The Y filter profile was supplied by Omega Optical. JH filter profiles were adapted from documentation supplied by Barr Associates. The HgCdTe FPA quantum efficiency was adapted from materials from Rockwell Scientific.

up to 150 lbs, although many users have found good performance beyond this limit.

6.4 Commissioning and Calibrations

Each of the five optical cameras has undergone a series of tests to ensure quality. These tests are roughly based on Tim Abbott's *In Situ CCD Testing Guide* that was written in 1995 and outlines the CCD testing program designed for the European Southern Observatory (ESO) in La Silla, Chile. Our tests include: (1) testing the cameras for light leaks, (2) looking for structure in the bias, (3) ensuring that the darks are scalable, (4) finding the effects of temperature on dark noise, (5) assessing the minimum allowed exposure time in order to remove

shutter effects, (6) determining the linearity of the CCD, and finally, measuring the (7) read noise and (8) gain. A summary of each camera, including its read noise and gain is given in Table 6.1.

Table 6.1: PROMPT Camera Characteristics

Telescope	Model	Serial No.	Gain (e-/ADU)	Readnoise (e-)
P1	U47 Mid	A4434	1.5	8.6
P2	U47+UV	A4435	1.5	8.4
P3	U47 Broad	A4245	1.6	19.0
P4	U47 Mid	A4201	2.2	28.2
P5	U47 Mid	A4437	1.6	11.3

The cameras passed most of the quality testing, but there are some significant problems. The dark noise for each camera is low, and scales normally with time and temperature, and although there are hot pixels, there is no large scale structure in the dark images. The minimum exposure time allowable by the speed of the shutter is approximately 0.4 seconds although exposure times could be set lower depending on the quality of the output needed. Low level shutter effects won't be noticeable in some of the public outreach projects PROMPT is involved with, and shorter exposure times would allow brighter objects, such as the moon and planets, to be observed. The CCD responds linearly until it reaches saturation near 40,000 – 50,000 counts; the exact saturation level is different for each camera.

Two of the Apogee Alta U47+ cameras have problems with additional noise and variable structure in the bias. From Table 6.1 one can see that P3 and P4 are currently affected by the problem. The noise appears as "waves" passing through the bias images that in effect increase the measured read noise. The waves move between individual exposures so we cannot subtract out the effect, and over long time scales, the problem worsens. The affected cameras will be returned to

Apogee one at a time this fall to minimize downtime. In addition to this, P2's camera suffers from defects due to the UV coating. Bright stars leave residual charge in the image that appears in subsequent exposures. For photometry this is not often a problem although care must be taken to determine if this is the case for each image or set of images.

Full commissioning of the instruments is scheduled to begin in Winter 2006 after the end of Chilean "rainy season". During this season, photometric nights are sparse and we are unable to ensure that we obtain quality photometric data (see Table 6.1). This series of tests includes: (1) determining photometric zero-points, extinction coefficients and color terms for the SDSS $ugriz$, NIR YJH and Johnson-Cousins $UBVRI$ filter sets, (2) observing astrometric standard fields to map positional distortion, and (3) measuring corrections to the flat-field by fitting a polynomial to the photometric residuals as a function of position on the chip. Because the CCD quantum efficiency and mirror coatings produce a different over-all color response for each telescope, the first test will be performed for each telescope in each filter – P2: $UBug$, P3: $UBugr$, P4: $BVRIriz$, P5: $BVRIiz$, P6: YJH. The polarimeter requires a unique set of tests and will be calibrated relative to polarimetric standards, and the NIR camera will not be operational until 2007.

Extinction coefficients and zero-points for the primary PROMPT GRB filters are presented in Table 6.3. These values are based on a preliminary analysis of observations of the ten middle latitude SDSS photometric standards given in Table 6.2. The full analysis will include observations of at least thirty standard stars taken under photometric conditions in order to accurately determine color terms.

Table 6.2: SDSS *ugriz* Photometric Standard Stars

Star	R.A.	Dec.	r	$u-g$	$g-r$	$r-i$	$i-z$
SA 114548	22:41:36.8	00:59:05.7	11.135	3.146	1.120	0.442	0.252
SA 114750	22:41:44.7	01:12:36.2	12.021	0.548	-0.212	-0.230	-0.163
G 27-45	22:44:56.3	-02:21:12.8	11.282	1.111	0.503	0.193	0.081
Ross 786	23:09:33.34	00:43:02.1	9.706	1.221	0.540	0.224	0.093
GD 246	23:12:23.07	10:47:04.2	13.346	-0.491	-0.504	-0.378	-0.367
PG2336	23:38:38.26	00:42:46.4	12.312	1.101	0.336	0.100	0.014
SA 115420	23:42:36.48	01:05:58.8	11.063	1.091	0.290	0.080	0.007
SA 115516	23:44:15.38	01:14:12.5	10.107	2.167	0.807	0.317	0.172
G 158-100	00:33:54.6	-12:07:58.9	14.691	1.101	0.510	0.222	0.092
SA 92263	00:55:39.41	00:36:20	11.467	2.229	0.801	0.307	0.166

Standard stars are taken from Smith et al. (2002).

6.5 GRB Observing Rates

Table 6.5 presents all PROMPT GRB observations and gives details of the GCN (GRB Coordinates Network) Circular if applicable. Many nights when GRB observations are triggered, either the images do not go deep enough early enough to be suitable for a GCN. This can happen when the field is not visible for many hours or if the weather prohibits adequate observing. The weather in Chile varies throughout the year, with the Chilean winter (May through September) bringing the most cloudy nights (see Table 6.1). Approximately 30 – 50% of the nights during this time are completely unusable, and only a very small fraction is photometric.

The table gives the general response of PROMPT: number of telescopes, filters used, the response time of the onset of observations from the time of the GRB trigger, and whether or not an afterglow was detected. It also gives details of the GCN reporting the observations: which filter was cited for the GCN, the

Table 6.3: PROMPT *ugriz* Preliminary Photometric Information

Filter	Telescope	Zeropoint	Extinction Coefficient	No. of Obs.	Airmass Range
u^a	P2	-	-	-	-
g	P3	22.01	0.228	141	1.05 - 1.68
r	P4	21.04	0.083	95	1.16 - 3.64
i	P4	20.61	0.039	85	1.17 - 3.71
z	P5	20.26	0.027	82	1.11 - 3.92

[a]the u filter has not yet arrived in Chile.

mean time of the reported value, the magnitude or limiting magnitude itself, and finally the number of the GCN Circular. This table contains all information as of October 1^{st}, 2006. Further details of PROMPT's rapid responses are given in Table 7.1.

As of September 29^{th}, 2006, PROMPT has triggered 78 GRB localizations since December 17^{th}, 2004, although 14 of these nights (18%) have been cloudy and not resulted in usable data. 71 of these have been *Swift* bursts (PROMPT has responded to 38% of all *Swift* bursts), 35 have been significant enough to be presented in a GCN observing report and 12 of these have resulted in the detection of an afterglow. Of the clear nights, 14 responses have been within an hour of the GRB trigger (19 cloudy), 10 have been within ten minutes (14 cloudy), and 8 have been within three minutes (11 cloudy). The last value of three minutes is the timescale we define as a *rapid response*.

PROMPT successfully automatically observed its first gamma-ray burst on July 30^{th}, 2005. Although the exact start date of operations is unknown, we can use this day to measure statistics for GRB responses. Since regular operations began, PROMPT has responded to 68 GRB alerts (only 5 are non-*Swift* triggers). *Swift* localizes a burst an average of every 3.5 days since this time, and PROMPT

Table 6.4: PROMPT Afterglow Follow-Up

GRB	Number of Telescopes	Filters (all)	Response Time [hr]	Detection? (y/n)	Filter (GCN)	Time (GCN)	Mag (GCN)	Circ. No. (GCN)
041217	1	R	22.700	n	R	23.8 hr	>21.5	2864
041219c	1	V	29.000	n	V	30.0 hr	>20.4	2900
050223	3	VRI	2.500	n	R	4.1 hr	>21.2	3067
050408	3	VRI	8.700	y	V	9.7 hr	21.4	3228
050412	1	VRI	0.097	n	R	6.7 min	>18.5	3259
050525	1	VRI	5.300	y	R	8.1 hr	19.8	3568
050607	1	VRI	0.225	n	I	14.1 min	>17.5	3535
050709	1	R	26.400	n	R	26.2 hr	>21.6	3702
050717	1	RI	13.000	n	R	13.7 hr	>21.7	3652
050726	1	R	18.500	n	R	19.8 hr	>22.2	3687
050730[a]	2	VRI	3.100	y	R	3.3 hr	17.8	3712
050801	1	VRI	4.621	n				
050803	2	$BVRI$	7.100	n	R	10 hr	>21.4	3780
050807	2	$BVRI$	12.304	n				
050815	1	B	5.781	cloudy				
050819	2	BI	10.449	cloudy				
050820a	2	$BVRI$	0.022	cloudy				
050820b	2	RI	2.000	y	R	2.2 hr	17.6	3863

Current as of September 28^{th}, 2006. [a]GRB 050730 marks the first successful automated response from SkyNet.

Table 6.5 (continued)

GRB	Number of Telescopes	Filters (all)	Response Time [hr]	Detection? (y/n)	Filter (GCN)	Time (GCN)	Mag (GCN)	Circ. No. (GCN)
050822	1	I	0.011	cloudy				
050824	2	$BVRI$	4.005	n				
050826	2	$BVRI$	0.754	n				
050827	2	$BVRI$	11.338	cloudy				
050904	2	RI	3.000	n	R	6.9 hr	$>20.0^b$	3913
050906	2	$BVRI$	16.960	n				
050908	2	$BVRI$	0.017	y	R	20 min	19.0	3947
050911	2	$BVRI$	7.580	n				
050915b	2	$BVRI$	2.077	n				
051016a	2	$BVRI$	0.110	n	R	25.6 min	>19.1	4097
051021a	2	RI	12.900	n	R	14.2 hr	>20.7	4147
051022	2	$BVRI$	10.746	n				
051109	2	$BVRI$	0.028	y	V	3.3 min	16.6	4220
051116	2	$BVRI$	16.148	n				
060108	2	UI	13.257	n				
060110	4	$Uriz$	16.799	cloudy				
060115	4	$UBIriz$	11.700	n	r	13.6 hr	>21.5	4530
060116	5	$UBIgriz$	16.200	n	I	19.1 hr	>21.6	4537

^{b}The limiting magnitude of the POSS2 catalogue is assumed to be ≈ 20.0.

Table 6.5 (continued)

GRB	Number of Telescopes	Filters (all)	Response Time [hr]	Detection? (y/n)	Filter (GCN)	Time (GCN)	Mag (GCN)	Circ. No. (GCN)
060117	4	$Uirz$	18.000	n	I	18.7 hr	>21.2	4548
060130	3	Irz	23.800	n	I	24.7 hr	>19.8	4626
060202	3	Uir	16.100	n	I	16.3 hr	>19.1	4642
060204a	2	Ur	15.178	n				
060204b	2	Ur	16.792	n				
060206	2	Uri	1.600	y	r	1.6 hr	16.9	4709
060210	3	BrI	19.541	n				
060211B	3	$BIri$	9.300	n	I	10.9 hr	>20.5	4772
060218	1	I	21.208	n				
060306	1	ri	0.014	n	i	7.5 min	>17.4	4849
060312	2	rI	22.342	n				
060313	2	Iri	0.728	y	r	1.3 hr	19.9	4878
060322	2	rI	5.415	n				
060418	3	$Ugriz$	0.011	y	z	42.5 s	15.3	4971
060428A	3	$Ugriz$	0.016	n	z	63 s	>17.1	5033
060501	2	rz	1.884	cloudy				
060505	3	$Ugriz$	23.200	n	z	25.5 hr	>20.6	5089
060512	1	Ug	0.828	cloudy				

Table 6.5 (continued)

GRB	Number of Telescopes	Filters (all)	Response Time [hr]	Detection? (y/n)	Filter (GCN)	Time (GCN)	Mag (GCN)	Circ. No. (GCN)
060516	3	Urz	16.140	n				
060522	3	$Ugriz$	3.100	n	r	4.2 hr	>21.1	5232
060526	3	$Ugriz$	6.388	y				
060602a	2	riz	1.252	cloudy				
060602b	2	riz	0.254	n				
060604	3	$Ugriz$	10.468	n				
060605	3	$Uriz$	9.638	n				
060607a	3	$UBgri$	0.012	y	r	65 s	16.3	5236
060607b	3	$Uriz$	10.704	cloudy				
060708	4	$UBgriz$	15.400	n	r	15.7 hr	>19.3	5299
060712	3	$Uriz$	1.799	cloudy				
060719	3	$Uriz$	0.010	n	z	58 s	>16.6	5344
060728	1	z	4.208	n				
060729	2	UBz	3.851	n				
060801	2	Uz	10.822	cloudy				
060807	3	$Uriz$	8.440	n				
060813	4	$UBgriz$	9.960	n				
060814	4	$UBgriz$	0.150	cloudy				

Table 6.5 (continued)

GRB	Number of Telescopes	Filters (all)	Response Time [hr]	Detection? (y/n)	Filter (GCN)	Time (GCN)	Mag (GCN)	Circ. No. (GCN)
060904b	3	*griz*	2.077	n				
060906	3	*griz*	0.038	cloudy				
060908	3	*Ugriz*	0.018	y	*r*	105 s	15	5545
060923b	3	*Urz*	11.910	n				
060926	4	*Ugriz*	6.765	n				
060927	4	*Ugriz*	14.113	n				

triggers to an alert an average of every 6.7 days. 20% of these responses are made under cloudy conditions, so we successfully observe *Swift* triggers $\approx 40\%$ of the time. The median response time for all bursts is 6.6 hours (average: 7.8 hr). Of the triggers with results worthy for the GCN Circulars, the median response time is 3.0 hours (average: 6.7 hr). These two numbers are biased though, because if there are deep limits reported early after the trigger we may cancel a pending GRB observation before PROMPT can observe it. Of the GRBs with a detected optical afterglow, the median response time is 0.4 hours (average: 1.4 hr).

The strength of PROMPT is in its rapid observations; these occur under clear skies roughly once every two months. Half of the afterglow detections made with PROMPT were observed through the rapid responses, and only seconds after the trigger. The median response for PROMPT after it recieves a GCN alert is 25 seconds (average: 33 sec). Although it can track an afterglow to deep limits, they are rarely bright enough to be detected hours after a trigger. §7 presents the eight rapid responses and gives detailed photometry and preliminary analysis.

Chapter 7

One Year of PROMPT Rapid Time GRB Observations

7.1 Introduction

Although PROMPT regularly observes afterglows beginning on the timescale of hours (see Table 6.5) and has produced high-quality and scientifically interesting data, the main success of PROMPT has been the rapid-time follow-up observations of gamma-ray bursts. At early times, GRBs can be incredibly bright, sometimes reaching R $\approx 10 - 12^{th}$ magnitude, although their brightnesses more often peak at around $15 - 17^{th}$ magnitude. PROMPT has responded to nine burst alerts on the rapid timescale, and for eight of these conditions at CTIO were clear enough for observations. Six of the eight rapid responses by PROMPT have resulted in the discovery of an afterglow. One of the eight is the dark burst GRB 060306 that was discussed in §5.2, and the remaining one, GRB 060719, had a detected afterglow, but it was too faint for PROMPT's small apertures. Table 7.1 summarizes these bursts.

Table 7.1: PROMPT Rapid Follow-Up of Gamma-Ray Bursts

GRB	Number of Telescopes	Filters	Response (GRB)	Response Time (GCN)	Detection? (y/n)
050908	2	$BVRI$	50 s	22 s	y
051109A	2	$BVRI$	102 s	38 s	y
060306	1	ri	49 s	25 s	n
060418	3	$Ugriz$	40 s	15 s	y
060428A	3	$Ugriz$	58 s	44 s	y
060607	3	$UBgri$	44 s	25 s	y
060719	3	$Uriz$	36 s	21 s	n
060906	3	$griz$	136 s	57 s	cloudy
060908	4	$Ugriz$	63 s	49 s	y

Current as of October 1^{st}, 2006.

7.2 GRB 050908

GRB 050908 was the very first successful rapid response by PROMPT, and is an example of PROMPT acting as a trigger for larger aperture telescopes. Two previous attempts at rapid follow-up (GRB 050820a & GRB 050822) were lost due to software failures, but on this date the automated observing pipeline worked properly. This GRB was not a very bright burst ($R \approx 19$ at 20 min), but we followed up the $BVRI$ PROMPT observations with optical imaging through UNC (11-m SALT, 8-m Gemini) and collaboration (Blanco 4-m) resources. Our coverage of this afterglow begins 49 seconds and lasts for nearly a day in $UuBgVrRiIz$ filters.

Observations

Swift observed GRB 050908 at 05:42:31 UT on September 8^{th}, 2005 and triggered a GCN alert 37 seconds afterwards (Goad et al. 2005a). The gamma-rays lasted for $t_{90} = 20$ seconds in the 15 – 350 keV range and underwent spectral

evolution at early times (Sato et al. 2005). No initial x-ray afterglow was found by XRT, but later a weak source was found coincident with the optical afterglow (Goad et al. 2005b). The temporal slope of the x-ray early afterglow is obscured by flares, but later data shows it to fade with $\alpha_x = -1.33$. The x-ray spectral slope also shows signs of spectral evolution; the early afterglow has a very steep slope of $\beta_x = -2.9^{+1.1}_{-0.5}$ that later settles to $\beta_x = -1.0 \pm 0.6$ (Goad et al. 2005c). *Swift*'s UVOT found only a very faint source in its early V images (de Pasquale et al. 2005).

Torii (2005b) announced the discovery of a dim afterglow in images taken at New Mexico Skies Observatory, and the identification was quickly confirmed by Cenko et al. (2005a) with images taken by the automated Palomar 60-inch telescope. Other groups followed the dim afterglow as it faded with $\alpha \approx -0.9$ (Piranomonte et al. 2005), and Fugazza et al. (2005) obtained a spectrum of the afterglow that found a high redshift of 3.350 ± 0.005. Using this redshift and $\Omega_M = 0.3$, $\Omega_\lambda = 0.7$ and $H_0 = 65$ km s^{-1} Mpc^{-1} Sato et al. (2005) derive $E_{iso} = 1.36 \times 10^{52}$ ergs in the GRB rest frame.

Collaborations Observations

PROMPT responded to the GCN alert and slewed to the field after only 22 seconds after receiving the message and 49 seconds after the GRB itself (Kirschbrown et al. 2005) and continued to observe in VRI the field for many hours. The dim afterglow is only visible by PROMPT for 40 minutes after which we initiated observations at larger telescopes. Collaborators triggered the Blanco 4-m telescope at CTIO, and obtained one 10 minute image in I at 1.4 hours post-burst. We imaged the field with Gemini South from 2.6 – 4.1 hours, and detected the fading source in $griz$. At 16.5 hours, we resumed imaging, now with the SALT Telescope in South Africa and continued for 5.4 hours in $UBVRI$.

Raw PROMPT images were processed through IRAF's CCDPROC, but the Gemini and SALT observations were reduced using IRAF reduction packages

specific to each instrument. Aperture photometry was performed using the DAOPHOT IRAF package. The observations are calibrated to stars from the USNO-B1.0 and Tycho-2 catalogs, and $BVRI$ magnitudes have been converted to $griz$ values using the conversions of Smith et al. (2002). The results of our global observing campaign are presented in Table 7.2 and Figure 7.1.

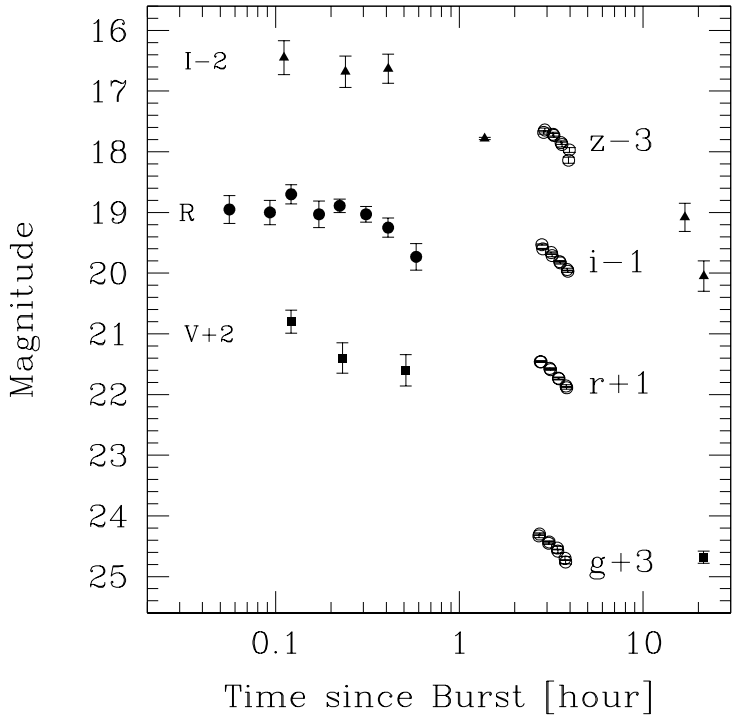

Figure 7.1: The $gVrRiIz$ afterglow of GRB 050908 from 49 seconds to 0.9 days. GRB 050908 is PROMPT's first successful detection of an early-time optical afterglow, and it led to observations with large aperture telescopes: the CTIO 4-m Blanco Telescope, the 8-m Gemini South Telescope and the 11-m South African Large Telescope (SALT).

Discussion

GRB 050908 marks the first successful rapid response of PROMPT to a GRB; on that night the entire observing pipeline functioned without fail. All hardware components and software packages worked properly, SkyNet responded to the

Table 7.2: UNC Observations of the Afterglow of GRB 050908

Mean Time (UT)	Exp Time (s)	Mean Δ t (hr)	Filter	Magnitude	Telescope
Sept 8 5:49:48	80	0.1214	V	18.80 ± 0.19	PROMPT
Sept 8 5:56:23	240	0.2311	V	19.40 ± 0.25	PROMPT
Sept 8 6:13:10	400	0.5109	V	19.60 ± 0.26	PROMPT
Sept 8 5:45:52	60	0.0560	R	18.95 ± 0.23	PROMPT
Sept 8 5:48:06	40	0.0931	R	19.00 ± 0.20	PROMPT
Sept 8 5:49:48	80	0.1214	R	18.70 ± 0.16	PROMPT
Sept 8 5:52:51	80	0.1722	R	19.03 ± 0.22	PROMPT
Sept 8 5:55:54	80	0.2231	R	18.89 ± 0.11	PROMPT
Sept 8 6:01:08	160	0.3103	R	19.03 ± 0.13	PROMPT
Sept 8 6:07:05	160	0.4096	R	19.25 ± 0.16	PROMPT
Sept 8 6:17:27	320	0.5821	R	19.73 ± 0.22	PROMPT
Sept 8 5:49:11	160	0.1110	I	18.45 ± 0.28	PROMPT
Sept 8 5:56:54	240	0.2397	I	18.68 ± 0.26	PROMPT
Sept 8 6:07:06	320	0.4099	I	18.63 ± 0.24	PROMPT
Sept 8 7:05:00	600	1.3747	I	19.78 ± 0.02	Blanco
Sept 8 8:25:03	30	2.7090	g	21.33 ± 0.03	Gemini-S
Sept 8 8:26:27	30	2.7322	g	21.30 ± 0.02	Gemini-S
Sept 8 8:46:07	30	3.0600	g	21.45 ± 0.02	Gemini-S
Sept 8 8:47:31	30	3.0833	g	21.43 ± 0.02	Gemini-S
Sept 8 9:07:11	30	3.4111	g	21.53 ± 0.03	Gemini-S
Sept 8 9:08:34	30	3.4342	g	21.58 ± 0.03	Gemini-S
Sept 8 9:28:14	30	3.7621	g	21.70 ± 0.03	Gemini-S
Sept 8 9:29:38	30	3.7853	g	21.76 ± 0.03	Gemini-S
Sept 8 8:27:55	45	2.7567	r	20.46 ± 0.01	Gemini-S
Sept 8 8:29:34	45	2.7842	r	20.46 ± 0.01	Gemini-S
Sept 8 8:48:59	45	3.1076	r	20.57 ± 0.01	Gemini-S
Sept 8 8:50:37	45	3.1350	r	20.59 ± 0.01	Gemini-S
Sept 8 9:10:03	45	3.4588	r	20.73 ± 0.02	Gemini-S
Sept 8 9:11:41	45	3.4861	r	20.74 ± 0.02	Gemini-S

GCN trigger, and weather conditions allowed for observing. Our later observations expand the insight from the early afterglow in order to give a broader view of the behavior of the afterglow and pinpoint the later temporal and spectral slope after the afterglow has began a more predictable fading behavior. This burst was not necessarily bright nor presented atypical features for us to model; its main importance lies in the successful, enthusiastic and collaborative follow-up effort.

Temporally, the early PROMPT afterglow remains flat until 16 minutes after which time it begins to fade with a slope of $\alpha = -1.15$. We do not see evidence for a break in the light curve within the data set which spans 21 hours post-burst. At z = 3.35 (Fugazza et al. 2005; Foley et al. 2005), Lyman α will be shifted to 529 nm, so we expect no emission in U or u, ≈90% suppression in B, moderate in g and slight suppression of V. This effect is easily seen in the Gemini-South g-band magnitudes, which are highly suppressed. Using the cases for the standard model (Wind & ISM, ν_c above and below ν_{opt}), for a temporal index of $\alpha = -1.15$, we expect $\beta = -0.43$ (Wind-Blue), -0.77 (ISM-Blue) or -1.10 (Wind or ISM Red). The early PROMPT spectral index is $\beta \approx -0.9$, which is consistent with the latter two scenarios.

7.3 GRB 051109A

PROMPT's second burst was observed under poor conditions at very high air-mass and just barely caught due to its Northern Hemisphere location. Although PROMPT successfully observed the burst beginning only 102 seconds after the GRB trigger, GRB 051109A occurred early in PROMPT's commissioning phase and hence only one telescope was operational at the time. A second telescope was not functioning due to a camera error, but was brought online beginning at nearly 20 minutes.

Table 7.2 (continued)

Mean Time (UT)	Exp Time (s)	Mean Δ t (hr)	Filter	Magnitude	Telescope
Sept 8 9:31:06	45	3.8097	r	20.86 ± 0.02	Gemini-S
Sept 8 9:32:45	45	3.8372	r	20.89 ± 0.02	Gemini-S
Sept 8 8:31:17	60	2.8129	i	20.53 ± 0.01	Gemini-S
Sept 8 8:33:11	60	2.8444	i	20.60 ± 0.01	Gemini-S
Sept 8 8:52:21	60	3.1640	i	20.66 ± 0.01	Gemini-S
Sept 8 8:54:15	60	3.1956	i	20.71 ± 0.02	Gemini-S
Sept 8 9:13:24	60	3.5147	i	20.81 ± 0.02	Gemini-S
Sept 8 9:15:18	60	3.5464	i	20.83 ± 0.02	Gemini-S
Sept 8 9:34:28	60	3.8658	i	20.94 ± 0.02	Gemini-S
Sept 8 9:36:21	60	3.8972	i	20.97 ± 0.02	Gemini-S
Sept 8 8:35:09	90	2.8772	z	20.68 ± 0.03	Gemini-S
Sept 8 8:37:33	90	2.9172	z	20.64 ± 0.03	Gemini-S
Sept 8 8:56:13	90	3.2283	z	20.71 ± 0.03	Gemini-S
Sept 8 8:58:36	90	3.2681	z	20.73 ± 0.03	Gemini-S
Sept 8 9:17:16	90	3.5792	z	20.85 ± 0.03	Gemini-S
Sept 8 9:19:40	90	3.6192	z	20.88 ± 0.04	Gemini-S
Sept 8 9:38:20	90	3.9301	z	21.14 ± 0.05	Gemini-S
Sept 8 9:40:43	90	3.9700	z	20.97 ± 0.04	Gemini-S
Sept 9 3:03:42	540	21.3531	V	22.68 ± 0.07	SALT
Sept 8 22:34:53	540	16.8727	I	21.08 ± 0.09	SALT
Sept 9 3:07:30	540	21.4164	I	22.05 ± 0.13	SALT

Observations

Swift localized the long (t_{90} = 36 ± 2 s) doubly-peaked GRB 051109A at 01:12:20 UT on November 9th 2005 (Tagliaferri et al. 2005; Fenimore et al. 2005). At 120 seconds, the *Swift* XRT discovered the fading x-ray afterglow, and at 123 seconds, *Swift*'s UVOT observed the bright optical afterglow. The early x-ray afterglow shows a steep decline with $\alpha \approx -3.1 \pm 0.6$, transitioning to a shallower $\alpha \approx -0.6 \pm 0.2$ (Campana et al. 2005).

The first GCN trigger was sent at 28 seconds, and within minutes, a bright optical afterglow candidate was reported by Rykoff et al. (2005) with an unfiltered magnitude of ≈ 15.5 as observed with ROTSE-III. Bloom (2005) confirmed the afterglow with rapid-time (Δt = 95 s) near-infrared observations with the automated telescope, PAIRITEL. In addition to these two, four more automated telescopes rapidly observed the afterglow: RAPTOR (34 seconds, Wozniak et al. 2005), Super-LOTIS (43 seconds, Milne et al. 2005), BOOTES (55 seconds, Jelinek et al. 2005), and PROMPT (102 seconds, Haislip et al. 2005a). Initial estimates of the decay rate of the afterglow show it to be more shallow than normal, with α between ≈ -0.4 (Schaefer et al. 2005) and ≈ -0.7 (Mirabal et al. 2005). Using the 9.2-m HET, Quimby et al. (2005) find a redshift to the burst of z = 2.346.

PROMPT Observations

Under the control of SkyNet, PROMPT observed the location of GRB 051109A at high airmass (Decl = +40:49:23.3) beginning 102 seconds after the GRB trigger with one of the PROMPT telescopes (Haislip et al. 2005a) in Bessell B & V. Imaging with the second PROMPT telescope was delayed due to a camera malfunction, but it obtained the field beginning at 18.6 minutes in Bessell R & I. The afterglow is bright in early V exposures, but all other images were stacked to improve signal-to-noise. Due to the camera error, the cooler was not

at its set point on the second telescope, and so R & I images are noisy due to an increased dark current . Each image was reduced using IRAF's CCDPROC package and psf photometered using IRAF's DAOPHOT package. The images were absolutely calibrated using field and standard stars taken with the 2.3-m Bok Telescope at Steward Observatory. Table 7.3 and Figure 7.2 summarize our results.

Table 7.3: PROMPT Observations of the Afterglow of GRB 051109A

Mean Time (UT)	Exp. Time	Mean Δt (hr)	Filter	Magnitude
Nov 9 1:35:23	160 s	0.3842	R	18.05 $\pm$ 0.10
Nov 9 1:41:29	160 s	0.4858	R	17.99 $\pm$ 0.11
Nov 9 1:44:24	160 s	0.5344	R	18.26 $\pm$ 0.11
Nov 9 1:53:20	160 s	0.6833	R	18.19 $\pm$ 0.11
Nov 9 1:14:36	20 s	0.0378	V	16.45 $\pm$ 0.28
Nov 9 1:15:40	20 s	0.0556	V	16.50 $\pm$ 0.19
Nov 9 1:17:13	40 s	0.0814	V	16.78 $\pm$ 0.17
Nov 9 1:18:56	40 s	0.1100	V	17.28 $\pm$ 0.20
Nov 9 1:21:42	80 s	0.1561	V	17.64 $\pm$ 0.14
Nov 9 1:24:49	80 s	0.2081	V	17.53 $\pm$ 0.14
Nov 9 1:29:25	80 s	0.2847	V	17.91 $\pm$ 0.16
Nov 9 1:40:38	200 s	0.4716	V	18.52 $\pm$ 0.25
Nov 9 1:15:45	60 s	0.0569	B	17.60 $\pm$ 0.21
Nov 9 1:19:06	120 s	0.1126	B	17.86 $\pm$ 0.15
Nov 9 1:35:24	280 s	0.3843	B	18.80 $\pm$ 0.36
Nov 9 1:35:25	320 s	0.3847	I	17.28 $\pm$ 0.13
Nov 9 1:47:24	160 s	0.5844	I	17.35 $\pm$ 0.16
Nov 9 1:50:20	160 s	0.6333	I	17.59 $\pm$ 0.15

Discussion

Only the V-band light curve is reliable enough to obtain a temporal decay index of the afterglow. Although sparsely sampled, the over-all slope of the light

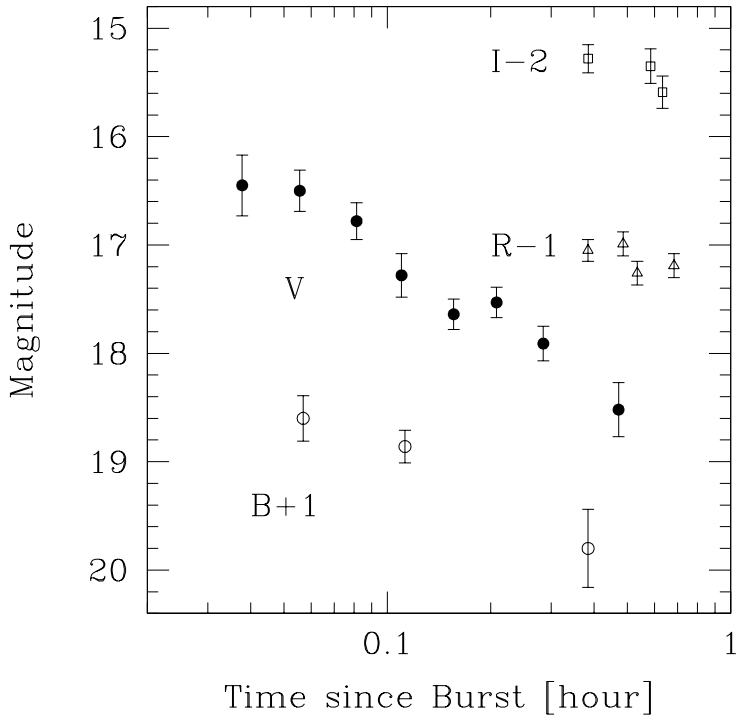

Figure 7.2: The $BVRI$ afterglow of GRB 051109A from 102 seconds to 40 minutes. A camera malfuntion and high declination hindered observations but we were still able to produce quality data.

curve is $\alpha \approx -0.8$. Collaboration data, along with the early V light curve suggest a shallow early slope similar to GRB 021004 (Fox et al. 2003b), GRB 050319 (Woźniak et al. 2005) and GRB 060124 (Curran et al. 2006). Uncertainties in the preliminary I-band field calibration ($\pm$ 0.4 mag) make obtaining a spectral index of the afterglow difficult. Disregarding this filter, at $\approx$ 25 minutes, the spectral energy distribution of the BVR bands shows a steep spectral slope of $\beta \approx -1.8$. At a redshift of z = 2.346, Lyman α is shifted to 407 nm and will minimally affect the B filter, hence the true slope is shallower than this estimate. None of the standard cases (Wind or constant density ISM; ν_c above or below ν_{opt}) can explain this steep index: given a temporal slope of $\alpha = -1.1$, the predicted spectral slopes are $\beta = -1.06$, -0.72 & -0.39 for ISM/Wind Red, ISM Blue and Wind Blue respectively. Extinction is likely the cause of any

additional steepening of the slope beyond the effect of Lyman α.

7.4 GRB 060306

The darkness of GRB 060306 was discussed on §5.2, but is also included here because it was a rapid-time response by PROMPT. Because we did not see an afterglow in our initial optical images, we triggered a Target of Opportunity on the 4.1-m SOAR telescope in K_s 1.0 days after the burst. A discussion of the discovery and the GRB community's follow-up efforts is presented in §5.2.2. The fast, near-infrared limits placed on afterglow emission by Chen et al. (2006) (see also Lamb et al. 2006) are especially significant given the brightness of the XRT x-ray afterglow (Page et al. 2006b). It is in the top 10% of brightest bursts, and out of all the bursts that can be classified as dark by the definition of Jakobsson et al. (2004) (optical to x-ray spectral slope is greater than -0.5) only GRB 060607 (§7.7) and GRB 060814 had brighter x-ray afterglows. The possibility of extinction as a cause of the darkness is discussed in §5.2.4.

PROMPT Observations

PROMPT responded to GRB 060306 only 49 seconds after the trigger and 25 seconds after the GCN notice (Nysewander et al. 2006a). At this point, only one of the PROMPT telescopes was functioning, but it observed the field in SDSS ri under partly cloudy conditions for nearly an hour before the field set below the horizon. Table 7.4 presents the limiting magnitudes of early single exposures, and later combined exposures that were stacked to match the filter sequence of the telescope. After scaling to 1.6 hours using $\alpha_{opt} = -1.0$, the deepest of these limiting magnitudes are plotted in Figure 5.2 along with the deep K_s and bright x-ray spectrum. The field was calibrated relative to the USNO-B1.0 and Tycho-2 catalogues, using the equations of Smith et al. (2002) to transform magnitudes from $BVRI$ to ri. The images were reduced in IRAF's

CCDPROC using standard methods, and photometered in IRAF's DAOPHOT.

Table 7.4: PROMPT Observations of the Field of GRB 060306

Mean Time (UT)	Exp. Time (s)	Mean Δt (hr)	Filter	Magnitude
Mar 6 0:50:03	5	0.0146	r	> 16.4
Mar 6 0:51:20	20	0.0361	r	> 17.8
Mar 6 0:53:05	40	0.0653	r	> 19.2
Mar 6 1:00:18	160	0.1854	r	> 20.0
Mar 6 1:10:16	240	0.3517	r	> 19.9
Mar 6 1:19:51	240	0.5115	r	> 20.0
Mar 6 1:33:16	320	0.7351	r	> 20.3
Mar 6 0:50:37	10	0.0242	i	> 16.5
Mar 6 0:52:07	20	0.0492	i	> 17.2
Mar 6 0:54:11	40	0.0836	i	> 17.9
Mar 6 0:56:42	80	0.1256	i	> 19.0
Mar 6 1:03:09	200	0.2330	i	> 18.5
Mar 6 1:13:08	240	0.3993	i	> 18.5
Mar 6 1:29:11	400	0.6669	i	> 19.3

Upper limits are 3σ.

7.5 GRB 060418

GRB 060418 is an awesome example of the strength of PROMPT: 218 individual measurements of the bright afterglow of the burst were taken in the Sloan *griz* filters between 42 seconds and 5 hours (see Figure 7.3). PROMPT caught the initial rise of the forward shock moving through optical wavelengths, which peak at least as bright as $z \approx 15.2$, and followed the light curve until it faded below $iz \approx 19^{th}$, and $gr \approx 20^{th}$ magnitude. The light curve shows a clear power-law fading of $\alpha \approx -1.2$, with only small deviations super-imposed.

Stunningly, though, this burst displays the delicacy of the SkyNet & PROMPT

system. If a single process in the chain fails, it can cause disastrous results. Shortly after PROMPT responded to the GCN trigger and after it was only able to take one observations of the afterglow, ($z \approx 15.2$, Δt = 43 s) the PC that runs SkyNet rebooted for weekly scheduled automatic Windows Updates. Luckily, this problem was noted quickly and a member of the UNC GRB Team was able to remotely log in to the computer to restart SkyNet, so PROMPT re-obtained the field at 16.6 minutes. The next day we moved the weekly automatic rebooting to be done at noon EST.

Observations

The *Swift* BAT detected the long (t $\approx$ 44 s, Golenetskii et al. 2006), bright GRB 060418 at 03:06:08 UT on April 18^{th} 2006 and issued a GCN trigger 25 seconds later. At 78 seconds, *Swift*'s XRT slewed to the site and further localized the position to a six arcsecond radius error circle. Bright flares are present in the XRT light curve, some of which correspond to flares in the GRB itself, but the underlying decay can be loosely constrained to $\alpha \approx -0.6 \pm 0.3$ (Falcone et al. 2006b). Starting 88 seconds after the BAT trigger, *Swift*'s UVOT found a bright $V \approx 14.5$ magnitude fading source within this localization (Falcone et al. 2006a).

Due to its middle latitude location and fortuitously good weather, four ground-based automated telescopes observed the localization within minutes: REM (in both NIR and optical, Covino et al. 2006a), PROMPT, (40 s; Nysewander et al. 2006b), FRAM (51 s; Jelinek et al. 2006), and the 2-m Liverpool Telescope (5 minutes; Melandri et al. 2006). Spectroscopic observations taken with the Magellan Clay Telescope only 28 minutes after the burst show a redshift of z = 1.49 (Dupree et al. 2006; Vreeswijk & Jaunsen 2006). Using this redshift and standard cosmological parameters, $H_0 = 70$ km s^{-1} Mpc^{-1}, $\Omega_M = 0.3$, $\Omega_\Lambda = 0.7$, Golenetskii et al. (2006) find E_{iso} to be $\approx 9 \times 10^{52}$ ergs.

PROMPT Observations

SkyNet responded to the GCN trigger in real time and PROMPT began observations within 14 seconds of the alert (42 seconds after the GRB time) yet produced only one 5 second Sloan z image before the poorly timed computer reboot. Observations continued at 16.6 minutes in the Bessell U and Sloan $griz$ filters with three telescopes simultaneously gathering data. The afterglow is clearly observed in single $griz$ early exposures; later exposures were stacked to improve signal-to-noise. The afterglow is not detected in U. Each image was reduced using IRAF's CCDPROC package and psf photometered using IRAF's DAOPHOT package. The observations are summarized in Table 7.5 and plotted in Figure 7.3.

Table 7.5: PROMPT Observations of the Afterglow of GRB 060418

Mean Time (UT)	Exp. Time	Mean Δt (hr)	Filter	Magnitude
Apr 18 3:25:54	80 s	0.3294	g	16.71 $\pm$ 0.03
Apr 18 3:27:25	80 s	0.3547	g	16.84 $\pm$ 0.02
Apr 18 3:32:04	80 s	0.4322	g	17.06 $\pm$ 0.03
Apr 18 3:33:35	80 s	0.4575	g	17.13 $\pm$ 0.03
Apr 18 3:41:10	80 s	0.5839	g	17.47 $\pm$ 0.02
Apr 18 3:42:41	80 s	0.6092	g	17.40 $\pm$ 0.04
Apr 18 3:44:13	80 s	0.6347	g	17.54 $\pm$ 0.03
Apr 18 3:45:24	80 s	0.6544	g	17.56 $\pm$ 0.05
Apr 18 3:53:12	80 s	0.7844	g	17.92 $\pm$ 0.04
Apr 18 3:54:46	80 s	0.8106	g	17.88 $\pm$ 0.05
Apr 18 3:56:17	80 s	0.8358	g	17.90 $\pm$ 0.05
Apr 18 3:57:28	80 s	0.8556	g	17.97 $\pm$ 0.06
Apr 18 4:05:11	80 s	0.9842	g	18.09 $\pm$ 0.03
Apr 18 4:06:42	80 s	1.0094	g	18.15 $\pm$ 0.04
Apr 18 4:08:12	80 s	1.0344	g	18.14 $\pm$ 0.05
Apr 18 4:09:43	80 s	1.0597	g	18.17 $\pm$ 0.05
Apr 18 4:11:15	80 s	1.0853	g	18.25 $\pm$ 0.04
Apr 18 4:12:46	80 s	1.1106	g	18.30 $\pm$ 0.05
Apr 18 4:14:18	80 s	1.1361	g	18.39 $\pm$ 0.07
Apr 18 4:26:38	80 s	1.3417	g	18.50 $\pm$ 0.09
Apr 18 4:28:09	80 s	1.3669	g	18.58 $\pm$ 0.08
Apr 18 4:29:40	80 s	1.3922	g	18.65 $\pm$ 0.06
Apr 18 4:31:12	80 s	1.4178	g	18.62 $\pm$ 0.09
Apr 18 4:32:43	80 s	1.4431	g	18.75 $\pm$ 0.10
Apr 18 4:35:44	80 s	1.4933	g	18.77 $\pm$ 0.11
Apr 18 4:48:04	80 s	1.6989	g	18.72 $\pm$ 0.09
Apr 18 4:49:35	80 s	1.7242	g	18.69 $\pm$ 0.09
Apr 18 4:51:08	80 s	1.7500	g	18.93 $\pm$ 0.12
Apr 18 4:52:41	80 s	1.7758	g	19.00 $\pm$ 0.13
Apr 18 4:54:14	80 s	1.8017	g	18.74 $\pm$ 0.11

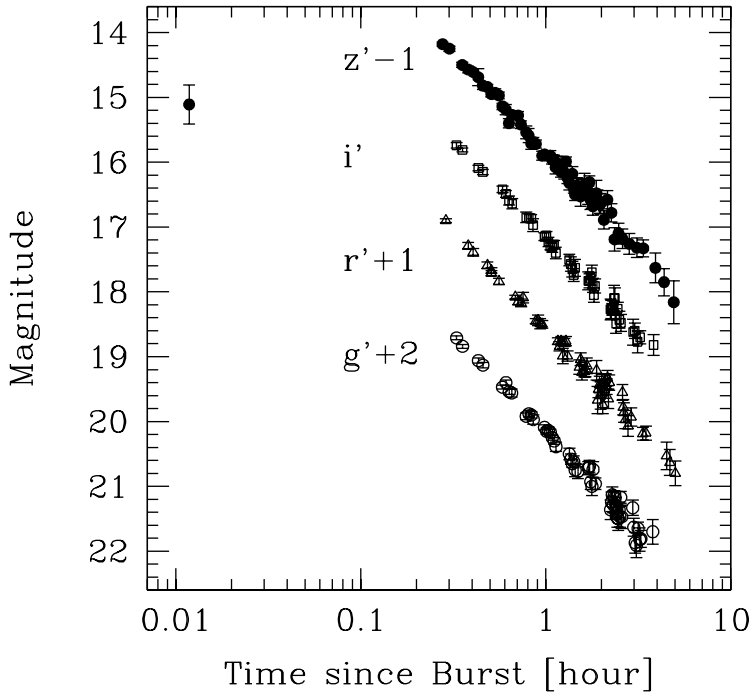

Figure 7.3: The PROMPT highly-sampled *griz* afterglow of GRB 060418 between 42 seconds and five hours.

Discussion

The light curve of GRB 060418 is well described as a power-law with temporal slope $\alpha = -1.21 \pm 0.03$ with small-scale achromatic superimposed variations. Although we are not able to glean much information from the early 5 second z-band point, we do witness the forward shock moving through optical wavelengths with no evidence for a bright reverse shock. If the forward shock rises and fades with a similar absolute slope (as is the case for GRB 060607; §7.7), then the afterglow peaked at ≈ 5 minutes.

At a redshift of z = 1.49, the Lyman α break is shifted to $\lambda = 303$ nm, which does not affect the shape of the *griz* spectrum. The spectrum has a steep power-law slope with $\beta_{opt} \approx -1.87$ with little signs of curvature, although

Table 7.5 (continued)

Mean Time (UT)	Exp. Time	Mean Δt (hr)	Filter	Magnitude
Apr 18 4:57:23	80 s	1.8542	g	18.96 $\pm$ 0.08
Apr 18 5:20:28	80 s	2.2389	g	19.36 $\pm$ 0.15
Apr 18 5:22:01	80 s	2.2647	g	19.24 $\pm$ 0.15
Apr 18 5:23:33	80 s	2.2903	g	19.13 $\pm$ 0.11
Apr 18 5:25:04	80 s	2.3156	g	19.28 $\pm$ 0.13
Apr 18 5:26:34	80 s	2.3406	g	19.15 $\pm$ 0.07
Apr 18 5:28:05	80 s	2.3658	g	19.18 $\pm$ 0.10
Apr 18 5:29:37	80 s	2.3914	g	19.29 $\pm$ 0.12
Apr 18 5:31:08	80 s	2.4167	g	19.39 $\pm$ 0.11
Apr 18 5:32:40	80 s	2.4422	g	19.49 $\pm$ 0.13
Apr 18 5:34:11	80 s	2.4675	g	19.50 $\pm$ 0.18
Apr 18 5:35:42	80 s	2.4928	g	19.36 $\pm$ 0.11
Apr 18 5:37:14	80 s	2.5183	g	19.47 $\pm$ 0.15
Apr 18 5:38:45	80 s	2.5436	g	19.17 $\pm$ 0.08
Apr 18 5:40:23	80 s	2.5708	g	19.47 $\pm$ 0.18
Apr 18 6:03:19	80 s	2.9531	g	19.33 $\pm$ 0.11
Apr 18 6:05:35	160 s	2.9910	g	19.63 $\pm$ 0.14
Apr 18 6:08:40	160 s	3.0424	g	19.87 $\pm$ 0.16
Apr 18 6:11:42	160 s	3.0929	g	19.91 $\pm$ 0.19
Apr 18 6:15:30	240 s	3.1561	g	19.65 $\pm$ 0.10
Apr 18 6:19:18	160 s	3.2194	g	19.82 $\pm$ 0.18
Apr 18 6:22:20	160 s	3.2700	g	19.81 $\pm$ 0.12
Apr 18 6:53:29	80 s	3.7892	g	19.70 $\pm$ 0.19
Apr 18 3:23:26	80 s	0.2883	r	15.90 $\pm$ 0.01
Apr 18 3:28:58	80 s	0.3806	r	16.29 $\pm$ 0.02
Apr 18 3:30:27	80 s	0.4053	r	16.39 $\pm$ 0.04
Apr 18 3:35:09	80 s	0.4836	r	16.59 $\pm$ 0.03
Apr 18 3:36:38	80 s	0.5083	r	16.67 $\pm$ 0.03
Apr 18 3:36:38	80 s	0.5083	r	16.71 $\pm$ 0.02
Apr 18 3:39:36	80 s	0.5578	r	16.84 $\pm$ 0.03

Table 7.5 (continued)

Mean Time (UT)	Exp. Time	Mean Δt (hr)	Filter	Magnitude
Apr 18 3:47:12	80 s	0.6844	r	17.08 $\pm$ 0.02
Apr 18 3:48:41	80 s	0.7092	r	17.15 $\pm$ 0.04
Apr 18 3:50:16	80 s	0.7356	r	17.17 $\pm$ 0.04
Apr 18 3:51:25	80 s	0.7547	r	17.09 $\pm$ 0.06
Apr 18 3:59:09	80 s	0.8836	r	17.45 $\pm$ 0.03
Apr 18 4:00:38	80 s	0.9083	r	17.44 $\pm$ 0.07
Apr 18 4:02:08	80 s	0.9333	r	17.49 $\pm$ 0.07
Apr 18 4:03:37	80 s	0.9581	r	17.50 $\pm$ 0.05
Apr 18 4:15:52	80 s	1.1622	r	17.76 $\pm$ 0.04
Apr 18 4:17:21	80 s	1.1869	r	17.84 $\pm$ 0.07
Apr 18 4:18:51	80 s	1.2119	r	17.76 $\pm$ 0.06
Apr 18 4:20:20	80 s	1.2367	r	17.99 $\pm$ 0.11
Apr 18 4:21:49	80 s	1.2614	r	17.78 $\pm$ 0.06
Apr 18 4:23:18	80 s	1.2861	r	17.76 $\pm$ 0.07
Apr 18 4:24:47	80 s	1.3108	r	17.99 $\pm$ 0.07
Apr 18 4:37:19	80 s	1.5197	r	18.16 $\pm$ 0.10
Apr 18 4:38:48	80 s	1.5444	r	18.04 $\pm$ 0.09
Apr 18 4:40:17	80 s	1.5692	r	18.24 $\pm$ 0.12
Apr 18 4:43:17	80 s	1.6192	r	18.23 $\pm$ 0.08
Apr 18 4:44:46	80 s	1.6439	r	18.19 $\pm$ 0.12
Apr 18 4:46:14	80 s	1.6683	r	18.14 $\pm$ 0.12
Apr 18 4:58:57	80 s	1.8803	r	18.21 $\pm$ 0.15
Apr 18 5:00:26	80 s	1.9050	r	18.67 $\pm$ 0.21
Apr 18 5:01:55	80 s	1.9297	r	18.50 $\pm$ 0.12
Apr 18 5:03:24	80 s	1.9544	r	18.43 $\pm$ 0.12
Apr 18 5:04:58	80 s	1.9806	r	18.60 $\pm$ 0.21
Apr 18 5:06:33	80 s	2.0069	r	18.43 $\pm$ 0.16
Apr 18 5:08:02	80 s	2.0317	r	18.74 $\pm$ 0.13
Apr 18 5:11:00	80 s	2.0811	r	18.50 $\pm$ 0.14
Apr 18 5:12:29	80 s	2.1058	r	18.36 $\pm$ 0.09

Table 7.5 (continued)

Mean Time (UT)	Exp. Time	Mean Δt (hr)	Filter	Magnitude
Apr 18 5:13:59	80 s	2.1308	r	18.46 $\pm$ 0.12
Apr 18 5:15:28	80 s	2.1556	r	18.33 $\pm$ 0.11
Apr 18 5:16:57	80 s	2.1803	r	18.65 $\pm$ 0.14
Apr 18 5:18:26	80 s	2.2050	r	18.40 $\pm$ 0.12
Apr 18 5:41:56	80 s	2.5967	r	18.55 $\pm$ 0.11
Apr 18 5:43:25	80 s	2.6214	r	18.78 $\pm$ 0.11
Apr 18 5:44:54	80 s	2.6461	r	18.86 $\pm$ 0.15
Apr 18 5:47:52	240 s	2.6956	r	18.97 $\pm$ 0.13
Apr 18 5:53:29	320 s	2.7891	r	19.07 $\pm$ 0.16
Apr 18 5:59:50	240 s	2.8950	r	18.93 $\pm$ 0.13
Apr 18 6:26:54	320 s	3.3460	r	19.19 $\pm$ 0.10
Apr 18 6:35:03	400 s	3.4819	r	19.18 $\pm$ 0.11
Apr 18 7:36:11	400 s	4.5008	r	19.53 $\pm$ 0.21
Apr 18 7:47:22	640 s	4.6873	r	19.63 $\pm$ 0.20
Apr 18 8:07:21	720 s	5.0203	r	19.80 $\pm$ 0.19
Apr 18 3:25:53	80 s	0.3292	i	15.74 $\pm$ 0.02
Apr 18 3:27:23	80 s	0.3542	i	15.81 $\pm$ 0.02
Apr 18 3:32:03	80 s	0.4319	i	16.09 $\pm$ 0.02
Apr 18 3:33:32	80 s	0.4567	i	16.15 $\pm$ 0.03
Apr 18 3:41:09	80 s	0.5836	i	16.42 $\pm$ 0.03
Apr 18 3:42:39	80 s	0.6086	i	16.49 $\pm$ 0.05
Apr 18 3:44:10	80 s	0.6339	i	16.59 $\pm$ 0.05
Apr 18 3:45:39	80 s	0.6586	i	16.64 $\pm$ 0.05
Apr 18 3:53:11	80 s	0.7842	i	16.85 $\pm$ 0.08
Apr 18 3:54:41	80 s	0.8092	i	16.86 $\pm$ 0.06
Apr 18 3:56:13	80 s	0.8347	i	16.87 $\pm$ 0.04
Apr 18 3:57:22	80 s	0.8539	i	16.97 $\pm$ 0.08
Apr 18 4:05:10	80 s	0.9839	i	17.15 $\pm$ 0.05
Apr 18 4:06:39	80 s	1.0086	i	17.13 $\pm$ 0.04
Apr 18 4:08:08	80 s	1.0333	i	17.23 $\pm$ 0.07

Table 7.5 (continued)

Mean Time (UT)	Exp. Time	Mean Δt (hr)	Filter	Magnitude
Apr 18 4:09:41	80 s	1.0592	i	17.30 ± 0.04
Apr 18 4:11:11	80 s	1.0842	i	17.31 ± 0.08
Apr 18 4:12:39	80 s	1.1086	i	17.27 ± 0.06
Apr 18 4:14:08	80 s	1.1333	i	17.40 ± 0.09
Apr 18 4:26:37	80 s	1.3414	i	17.51 ± 0.09
Apr 18 4:28:06	80 s	1.3661	i	17.57 ± 0.10
Apr 18 4:29:36	80 s	1.3911	i	17.65 ± 0.11
Apr 18 4:31:05	80 s	1.4158	i	17.74 ± 0.09
Apr 18 4:32:34	80 s	1.4406	i	17.63 ± 0.12
Apr 18 4:48:04	80 s	1.6989	i	17.83 ± 0.13
Apr 18 4:49:33	80 s	1.7236	i	17.83 ± 0.11
Apr 18 4:51:02	80 s	1.7483	i	17.80 ± 0.10
Apr 18 4:52:32	80 s	1.7733	i	17.70 ± 0.09
Apr 18 4:54:00	80 s	1.7978	i	17.90 ± 0.10
Apr 18 4:55:29	80 s	1.8225	i	18.05 ± 0.11
Apr 18 4:56:58	80 s	1.8472	i	17.91 ± 0.10
Apr 18 5:20:27	80 s	2.2386	i	18.27 ± 0.16
Apr 18 5:21:56	80 s	2.2633	i	18.27 ± 0.13
Apr 18 5:23:26	80 s	2.2883	i	18.27 ± 0.08
Apr 18 5:24:56	80 s	2.3133	i	18.25 ± 0.11
Apr 18 5:26:25	80 s	2.3381	i	18.10 ± 0.20
Apr 18 5:27:54	80 s	2.3628	i	18.10 ± 0.16
Apr 18 5:30:08	160 s	2.3999	i	18.49 ± 0.14
Apr 18 5:33:06	160 s	2.4494	i	18.26 ± 0.09
Apr 18 5:36:06	160 s	2.4994	i	18.43 ± 0.12
Apr 18 5:39:06	160 s	2.5493	i	18.48 ± 0.12
Apr 18 6:04:06	160 s	2.9660	i	18.62 ± 0.20
Apr 18 6:07:51	240 s	3.0286	i	18.60 ± 0.12
Apr 18 6:14:33	320 s	3.1402	i	18.77 ± 0.17
Apr 18 6:20:31	320 s	3.2397	i	18.70 ± 0.09

Table 7.5 (continued)

Mean Time (UT)	Exp. Time	Mean Δt (hr)	Filter	Magnitude
Apr 18 6:55:47	400 s	3.8275	i	18.82 $\pm$ 0.15
Apr 18 3:06:51	5 s	0.0118	z	16.11 $\pm$ 0.29
Apr 18 3:22:44	80 s	0.2767	z	15.18 $\pm$ 0.02
Apr 18 3:24:13	80 s	0.3014	z	15.25 $\pm$ 0.03
Apr 18 3:27:21	80 s	0.3536	z	15.50 $\pm$ 0.03
Apr 18 3:28:56	80 s	0.3800	z	15.57 $\pm$ 0.04
Apr 18 3:30:25	80 s	0.4047	z	15.61 $\pm$ 0.03
Apr 18 3:32:01	80 s	0.4314	z	15.69 $\pm$ 0.06
Apr 18 3:33:32	80 s	0.4567	z	15.82 $\pm$ 0.05
Apr 18 3:35:07	80 s	0.4831	z	15.84 $\pm$ 0.02
Apr 18 3:36:36	80 s	0.5078	z	15.95 $\pm$ 0.03
Apr 18 3:38:05	80 s	0.5325	z	15.93 $\pm$ 0.04
Apr 18 3:39:34	80 s	0.5572	z	15.97 $\pm$ 0.05
Apr 18 3:41:07	80 s	0.5831	z	16.14 $\pm$ 0.04
Apr 18 3:42:36	80 s	0.6078	z	16.19 $\pm$ 0.07
Apr 18 3:44:04	80 s	0.6322	z	16.40 $\pm$ 0.07
Apr 18 3:45:35	80 s	0.6575	z	16.27 $\pm$ 0.04
Apr 18 3:48:39	80 s	0.7086	z	16.28 $\pm$ 0.06
Apr 18 3:50:10	80 s	0.7339	z	16.42 $\pm$ 0.06
Apr 18 3:53:10	80 s	0.7839	z	16.54 $\pm$ 0.10
Apr 18 3:54:39	80 s	0.8086	z	16.59 $\pm$ 0.11
Apr 18 3:56:08	80 s	0.8333	z	16.71 $\pm$ 0.08
Apr 18 3:57:36	80 s	0.8578	z	16.69 $\pm$ 0.07
Apr 18 3:59:07	80 s	0.8831	z	16.72 $\pm$ 0.05
Apr 18 4:03:34	80 s	0.9572	z	16.90 $\pm$ 0.06
Apr 18 4:05:08	80 s	0.9833	z	16.88 $\pm$ 0.05
Apr 18 4:09:35	80 s	1.0575	z	16.90 $\pm$ 0.07
Apr 18 4:11:04	80 s	1.0822	z	16.96 $\pm$ 0.07
Apr 18 4:12:33	80 s	1.1069	z	16.96 $\pm$ 0.06
Apr 18 4:14:02	80 s	1.1317	z	17.08 $\pm$ 0.10

Table 7.5 (continued)

Mean Time (UT)	Exp. Time	Mean Δt (hr)	Filter	Magnitude
Apr 18 4:15:50	80 s	1.1617	z	17.02 $\pm$ 0.11
Apr 18 4:17:19	80 s	1.1864	z	17.09 $\pm$ 0.08
Apr 18 4:18:48	80 s	1.2111	z	17.15 $\pm$ 0.08
Apr 18 4:20:17	80 s	1.2358	z	17.03 $\pm$ 0.12
Apr 18 4:21:45	80 s	1.2603	z	17.16 $\pm$ 0.09
Apr 18 4:23:14	80 s	1.2850	z	16.99 $\pm$ 0.07
Apr 18 4:24:43	80 s	1.3097	z	17.24 $\pm$ 0.08
Apr 18 4:26:35	80 s	1.3408	z	17.32 $\pm$ 0.11
Apr 18 4:29:37	80 s	1.3914	z	17.18 $\pm$ 0.11
Apr 18 4:31:05	80 s	1.4158	z	17.41 $\pm$ 0.07
Apr 18 4:32:34	80 s	1.4406	z	17.50 $\pm$ 0.09
Apr 18 4:34:02	80 s	1.4650	z	17.36 $\pm$ 0.12
Apr 18 4:35:31	80 s	1.4897	z	17.37 $\pm$ 0.11
Apr 18 4:38:46	80 s	1.5439	z	17.53 $\pm$ 0.15
Apr 18 4:40:15	80 s	1.5686	z	17.39 $\pm$ 0.11
Apr 18 4:43:13	80 s	1.6181	z	17.35 $\pm$ 0.18
Apr 18 4:46:10	80 s	1.6672	z	17.39 $\pm$ 0.14
Apr 18 4:48:02	80 s	1.6983	z	17.51 $\pm$ 0.14
Apr 18 4:49:31	80 s	1.7231	z	17.31 $\pm$ 0.10
Apr 18 4:50:59	80 s	1.7475	z	17.58 $\pm$ 0.14
Apr 18 4:52:28	80 s	1.7722	z	17.60 $\pm$ 0.11
Apr 18 4:53:57	80 s	1.7969	z	17.68 $\pm$ 0.14
Apr 18 4:58:55	80 s	1.8797	z	17.48 $\pm$ 0.20
Apr 18 5:00:23	80 s	1.9042	z	17.58 $\pm$ 0.15
Apr 18 5:03:22	80 s	1.9539	z	17.64 $\pm$ 0.15
Apr 18 5:04:51	80 s	1.9786	z	17.64 $\pm$ 0.15
Apr 18 5:09:50	240 s	2.0617	z	17.89 $\pm$ 0.14
Apr 18 5:15:21	240 s	2.1537	z	17.58 $\pm$ 0.14
Apr 18 5:21:54	240 s	2.2628	z	17.78 $\pm$ 0.14
Apr 18 5:27:22	240 s	2.3539	z	18.19 $\pm$ 0.18

Table 7.5 (continued)

Mean Time (UT)	Exp. Time	Mean Δt (hr)	Filter	Magnitude
Apr 18 5:34:36	320 s	2.4745	z	18.10 $\pm$ 0.16
Apr 18 5:41:57	400 s	2.5971	z	18.18 $\pm$ 0.15
Apr 18 5:55:42	480 s	2.8262	z	18.26 $\pm$ 0.16
Apr 18 6:12:45	640 s	3.1103	z	18.32 $\pm$ 0.15
Apr 18 6:28:12	640 s	3.3679	z	18.33 $\pm$ 0.13
Apr 18 7:01:11	800 s	3.9174	z	18.63 $\pm$ 0.23
Apr 18 7:27:51	1200 s	4.3619	z	18.85 $\pm$ 0.21
Apr 18 8:01:24	1600 s	4.9211	z	19.16 $\pm$ 0.33

without near-infrared observations it is difficult to constrain extinction through curvature. Using the relations between the spectral and temporal slopes for the four cases of wind or ISM density, and if ν_c is redward or blueward of the optical, we find no clearly preferred model. Any of the four models must have a large amount of extinction to account for the very steep spectral slope. Given the tight slope of $\alpha = -1.21 \pm 0.03$, the spectral slope, $\beta = -1.14$, -0.81, & -0.41 for the ISM/Wind-Red, ISM-Blue, and Wind-Blue cases respectively.

7.6 GRB 060428A

GRB 060428A was a burst that suffered from many magnitudes of extinction, although instead of host extinction, this burst was localized close to the Milky Way's Galactic plane. PROMPT responded in rapid time, 58 seconds after the trigger, but did not see evidence for a fading afterglow (Haislip et al. 2006a). A faint peculiar afterglow was later announced (Cobb 2006), and upon reanalysis of the PROMPT data set we find that the object is marginally detected in it. The afterglow is odd due to its shallow decay that confused both the PROMPT & UVOT (de Pasquale & Mangano 2006) follow-up teams into overlooking it as an afterglow candidate.

Observations

GRB 060428A was localized by the *Swift* BAT instrument at 03:22:48 UT on April 28^{th} 2006 (Mangano et al. 2006a). *Swift*'s XRT telescope swiftly slewed to the localization of the burst and observed a very bright x-ray afterglow that constrained the error circle to 4.7 arcseconds at 69 seconds after the initial trigger. The x-ray light curve shows an initial very rapid decay with slope of -6.3 ± 0.4 with a break at 144 ± 6 seconds where it flattens to a very shallow slope of -0.11 ± 0.03 (Mangano et al. 2006b). Beginning at 71 seconds, *Swift*'s UVOT took a 400 second V-band image that did not detect an optical afterglow to $V > 19.1$ mag (Mangano et al. 2006a).

Due to the burst's proximity to the Galactic plane (Galactic latitude = 1.4^{o}), we expect large line-of-sight Milky Way $UBVRI$ extinction of 5.9, 4.5, 3.6 and 2.6 magnitudes respectively (Schlegel et al. 1998). In an image beginning at 60s after the GRB trigger, de Pasquale & Mangano (2006) find a possible transient in a revised analysis of the UVOT data which, although it is faint and a weak detection ($V \approx 20$, S/N ≈ 4), does not appear in archive images. Haislip et al. (2006a) do not detect the candidate afterglow in Ugriz in a preliminary analysis, but Cobb (2006) find that the source faded in J & I between 20.9 and 68.4 hours, which both confirms the source as the afterglow and also implies a shallow decay slope of $\alpha > -0.8$ during the first day.

PROMPT Observations

Skynet observed the localization of GRB 060428A with three of the PROMPT telescopes beginning 58 sec after the burst (44 sec after notification) in Bessell U and Sloan $griz$. Taking into account the expected Galactic extinction, the U band does not yield constraining limits and are not included in the analysis. Upon reanalysis, we detect the afterglow in the riz filters and obtain the results listed in Table 7.6 that are plotted in Figure 7.4. Individual images were re-

duced using IRAF's CCDPROC, photometered using IRAF's APPHOT package and calibrated to field stars from the USNO-B1.0 & Tycho-2 catalogues whose magnitudes were transformed to *griz* using the equations of Smith et al. (2002). Later images were stacked to enhance the signal of the afterglow.

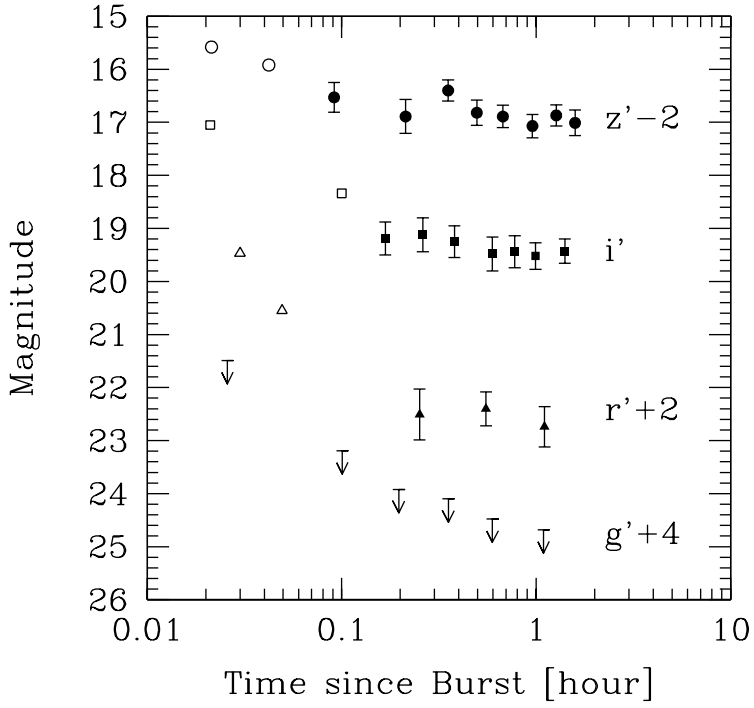

Figure 7.4: PROMPT *griz* observations of the unusual afterglow of GRB 060428 between one minute and 1.5 hours. Open data are upper limits, and note that there were no detections in the g filter.

Discussion

GRB 060428A was bright in x-rays, but was viewed through the plane of the Milky Way, so it was extinguished significantly at optical wavelengths. We expect *griz* to suffer from 4.7, 3.7, 3.0 and 1.9 magnitudes of extinction respectively (Schlegel et al. 1998; Smith et al. 2002). The near darkness of this burst (optical to x-ray $\beta = -0.54$) is caused by our own galaxy, but a similar situation, one

Table 7.6: PROMPT Observations of the Dim Afterglow of GRB 060428A

Mean Time (UT)	Exp. Time (s)	Mean Δt (hr)	Filter	Magnitude
Apr 28 3:24:21	10	0.0258	g	> 17.49
Apr 28 3:28:50	80	0.1006	g	> 19.19
Apr 28 3:34:35	160	0.1964	g	> 19.92
Apr 28 3:44:00	240	0.3533	g	> 20.10
Apr 28 3:58:32	480	0.5956	g	> 20.48
Apr 28 4:28:17	720	1.0913	g	> 20.68
Apr 28 3:24:36	10	0.0300	r	> 17.47
Apr 28 3:25:46	40	0.0494	r	> 18.55
Apr 28 3:37:54	280	0.2514	r	20.51 ± 0.48
Apr 28 3:55:55	520	0.5519	r	20.40 ± 0.32
Apr 28 4:29:02	560	1.1039	r	20.74 ± 0.38
Apr 28 3:24:04	10	0.0211	i	> 16.99
Apr 28 3:28:48	40	0.1000	i	> 18.28
Apr 28 3:32:51	160	0.1675	i	19.19 ± 0.31
Apr 28 3:38:30	120	0.2615	i	19.12 ± 0.32
Apr 28 3:45:35	200	0.3798	i	19.25 ± 0.30
Apr 28 3:58:31	240	0.5953	i	19.48 ± 0.32
Apr 28 4:09:18	240	0.7749	i	19.44 ± 0.30
Apr 28 4:22:16	400	0.9911	i	19.52 ± 0.25
Apr 28 4:47:01	400	1.4036	i	19.43 ± 0.23
Apr 28 3:24:05	20	0.0214	z	> 17.58
Apr 28 3:25:20	40	0.0422	z	> 17.92
Apr 28 3:28:17	160	0.0914	z	18.53 ± 0.28
Apr 28 3:35:35	280	0.2131	z	18.89 ± 0.32
Apr 28 3:43:57	360	0.3525	z	18.40 ± 0.20
Apr 28 3:52:31	440	0.4953	z	18.82 ± 0.24
Apr 28 4:03:14	480	0.6739	z	18.89 ± 0.21
Apr 28 4:20:12	640	0.9564	z	19.07 ± 0.22
Apr 28 4:38:52	640	1.2678	z	18.87 ± 0.20
Apr 28 4:57:53	640	1.5847	z	19.01 ± 0.24

Upper limits are 3σ.

where the burst is viewed through the plane of the host galaxy, is certainly a cause of a small percentage of dark bursts. In that situation, the burst suffers from extinction, but not the extinction expected from the circumburst giant molecular cloud environment.

8×60 second i band images taken with PROMPT on October 8^{th}, 2006 confirm the identification by Cobb (2006) of the afterglow. The source had faded below the detection limit of the stacked set of images that had a 3 σ limiting magnitude of $i > 20.2$. The source appears to fade with a rate of $\alpha \approx -0.15$ during the PROMPT detections from 0.1 to 1.5 hours, and images taken the second night by Cobb (2006) find a decay of $\alpha > -0.8$ from 1 to 3 days post-burst. The x-ray afterglow during this times was fading as only $\alpha_x = -0.11 \pm$ 0.03 (Mangano et al. 2006b), and so the optical light curve may be mimicking the shallow slope.

7.7 GRB 060607

PROMPT observed the bright afterglow of GRB 060607 and produced a highly sampled multi-color early-time light curve. The data span the time period beginning 47 seconds after the GRB trigger to 3.3 hours in the $UBgri$ filters. We see the forward shock synchrotron peak pass through the optical frequencies at approximately three minutes, followed by rebrightenings in the afterglow light curve peaking around 40 minutes and 66 minutes. Although our data overlap with the early *Swift* BAT and XRT data, we do not see any correlation between the light curves.

In many of the most highly-sampled light curves similar significant variations are seen super imposed upon the large-scale behavior. The variations seen in the afterglows of GRB 021004 and GRB 030329 are the most well-studied and have been test cases for the three main physical models that have been proposed to explain these features: (1) the "patchy shell" model (Kumar & Piran 2000a), (2)

delayed shocks or continuous energy injections (Rees & Meszaros 1998; Kumar & Piran 2000b; Sari & Mészáros 2000), and (3) variations in the external density (Wang & Loeb 2000; Dai & Lu 2002). Only with a data set of this quality are we able to ask detailed questions about the nature of the early afterglow and explore the possibility of significant chromatic variations.

In the "patchy shell" model, variations in the energy per unit angle in the outflow create the observed bumps in the light curve; the amplitude of these bumps is expected to decrease with time. For GRB 021004 de Ugarte Postigo et al. (2005a) find this to be an acceptable scenario, and Nakar et al. (2003) find this model to be preferred over the other two due to the inferred electron power-law index, p, that they find agrees with Chandra x-ray observations. For GRB 030329 Granot et al. (2003) ruled out this scenario because the variations occurred after the jet break, when the contribution from this effect should be negligible.

Additional energy injections, also described as delayed or refreshed shocks, are hypothesized to be due to slower moving shells emitted by the central source and impacting upon the bulk flow (Zhang & Mészáros 2002) and were first proposed for GRB 021004 by Fox et al. (2003b) and GRB 030329 by Granot et al. (2003). For GRB 021004, both Björnsson et al. (2004) and de Ugarte Postigo et al. (2005a) also find that the light curves, broad-band spectral evolution and polarization signature of GRB 021004 can be well-modeled with a series of energy injections. Due to the observation that the light curve of GRB 030329 retains its over-all behavior during rebrightening episodes that appear to be simple renormalizations, Granot et al. (2003) find refreshed shocks to be the most natural explanation in this case. Huang et al. (2006) agree with this analysis and also prefer refreshed shocks for GRB 030329. Jóhannesson et al. (2006) apply a discrete and continuous energy injection model to three bursts, GRB 990510, GRB 000301C and GRB 010222, to successfully model their broad-band behavior.

Shocks resulting from the fireball impacting onto density enhancements in the

surrounding medium can cause rebrightenings in the GRB afterglow below the cooling frequency, ν_c. When the shockwave hits a higher-density shell, the flux sharply increases before it asymptotically fades to match a light curve describing that of the higher density. Lazzati et al. (2002b) propose that the variations in the light curve of GRB 021004 are likely due to moderate density enhancements that only slightly modify the dynamics of the fireball, although they may not be able to explain the observed polarization (Björnsson et al. 2004). Many groups find that density enhancements can not account for the light curve of GRB 030329 due to the increase in flux normalization after each bump (Granot et al. 2003; Huang et al. 2006; Uemura et al. 2004).

Observations

The *Swift* Burst Alert Telescope (BAT) triggered the gamma-ray burst GRB 060607 at 05:12:13 UT on June 7^{th} 2006 (Ziaeepour et al. 2006). The afterglow duration is approximately $T_{90} = 100$ seconds (15 – 350 keV) and exhibits a triply-peaked structure (Tueller et al. 2006). Sixty-five seconds after the initial trigger, the *Swift*'s XRT found a fading x-ray afterglow (Page et al. 2006a), and at 75 seconds, UVOT began to observe the bright optical afterglow (Oates et al. 2006). Covino et al. (2006b) quickly reported a detection in the near-infrared made by the REM telescope, which began 1.5 minutes after the trigger. Nysewander & Haislip (2006) reported on the approximate r-band structure of the early optical afterglow. Ledoux et al. (2006), began imaging with VLT 7.5 minutes after the BAT trigger and found an afterglow redshift of z = 3.082. Tueller et al. (2006) find that using this redshift and standard cosmology ($\Omega_M = 0.3$, $\Omega_\Lambda = 0.7$, $H_0 = 65$) $E_{iso} = 1.1 \times 10^{53}$ ergs.

PROMPT Observations

Four 0.4-m PROMPT telescopes began observing the afterglow of GRB 060607 44 seconds after the initial satellite trigger and 25 seconds after the GCN noti-

fication in the UB Bessell and gri SDSS filters. Observations continued for 5.4 hours under the control of SkyNet. Images in the U filter and all images taken after 3.3 hours do not yield detections or limiting magnitudes deep or significant enough to be included in the analysis. Table 7.7 gives details of the observations, and these are plotted in Figure 7.5. The values listed in Table 1 supercede the preliminary analysis of Nysewander & Haislip (2006).

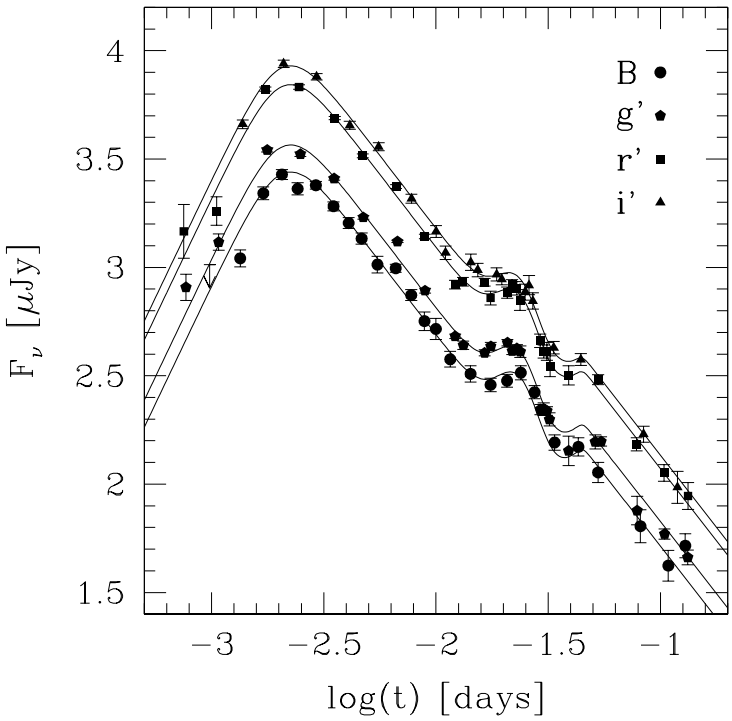

Figure 7.5: The PROMPT $Bgri$ afterglow of GRB 060607 beginning at 44 seconds and lasting until 3.2 hours. The solid lines show the general fit to the three variations that occur at 3, 42 and 64 minutes and are described in Table 7.8.

Zero, dark and flat-field calibration images were applied using IRAF's CCDPROC package, and, if appropriate, images were averaged in order to obtain better signal-to-noise. Point-spread function photometry was applied via IRAF's DAOPHOT package to obtain final magnitudes. Photometric zeropoints for each image were measured by comparing with calibration stars obtained with PROMPT on the night of June 12, 2006.

Table 7.7: PROMPT Observations of the Afterglow of GRB 060607

Mean Time (UT)	Exp. Time	Mean Δt (hr)	Filter	Magnitude
Jun 7 5:13:38	15 s	0.0235	B	>16.61
Jun 7 5:14:09	20 s	0.0322	B	16.44 $\pm$ 0.10
Jun 7 5:14:40	20 s	0.0408	B	15.69 $\pm$ 0.07
Jun 7 5:15:11	20 s	0.0494	B	15.47 $\pm$ 0.06
Jun 7 5:15:42	20 s	0.0581	B	15.63 $\pm$ 0.07
Jun 7 5:16:25	40 s	0.0700	B	15.59 $\pm$ 0.04
Jun 7 5:17:15	40 s	0.0839	B	15.84 $\pm$ 0.05
Jun 7 5:18:06	40 s	0.0981	B	16.03 $\pm$ 0.06
Jun 7 5:18:56	40 s	0.1119	B	16.21 $\pm$ 0.07
Jun 7 5:20:07	80 s	0.1317	B	16.51 $\pm$ 0.09
Jun 7 5:21:45	80 s	0.1589	B	16.55 $\pm$ 0.05
Jun 7 5:23:23	80 s	0.1861	B	16.86 $\pm$ 0.06
Jun 7 5:25:01	80 s	0.2133	B	17.16 $\pm$ 0.11
Jun 7 5:26:36	80 s	0.2397	B	17.25 $\pm$ 0.12
Jun 7 5:28:53	160 s	0.2778	B	17.60 $\pm$ 0.09
Jun 7 5:32:44	240 s	0.3420	B	17.77 $\pm$ 0.09
Jun 7 5:37:26	240 s	0.4203	B	17.89 $\pm$ 0.08
Jun 7 5:42:04	240 s	0.4974	B	17.85 $\pm$ 0.07
Jun 7 5:46:36	240 s	0.5730	B	17.75 $\pm$ 0.08
Jun 7 5:51:50	320 s	0.6601	B	17.98 $\pm$ 0.07
Jun 7 6:00:52	640 s	0.8110	B	18.56 $\pm$ 0.09
Jun 7 6:14:19	800 s	1.0350	B	18.61 $\pm$ 0.11
Jun 7 6:28:11	640 s	1.2662	B	18.91 $\pm$ 0.11
Jun 7 7:09:32	960 s	1.9553	B	19.53 $\pm$ 0.19
Jun 7 7:48:25	1200 s	2.6033	B	19.98 $\pm$ 0.18
Jun 7 8:18:06	1360 s	3.0981	B	19.75 $\pm$ 0.14
Jun 7 5:13:20	5 s	0.0185	g	16.63 $\pm$ 0.15
Jun 7 5:13:46	10 s	0.0258	g	16.11 $\pm$ 0.10
Jun 7 5:14:46	10 s	0.0425	g	15.04 $\pm$ 0.03

Upper limits are 3σ.

Table 7.7 (continued)

Mean Time (UT)	Exp. Time	Mean Δt (hr)	Filter	Magnitude
Jun 7 5:15:48	20 s	0.0597	g	15.09 $\pm$ 0.03
Jun 7 5:17:17	20 s	0.0844	g	15.37 $\pm$ 0.02
Jun 7 5:19:03	40 s	0.1139	g	15.82 $\pm$ 0.02
Jun 7 5:21:55	80 s	0.1617	g	16.10 $\pm$ 0.01
Jun 7 5:25:06	80 s	0.2147	g	16.67 $\pm$ 0.03
Jun 7 5:29:45	80 s	0.2922	g	17.20 $\pm$ 0.03
Jun 7 5:31:17	80 s	0.3178	g	17.30 $\pm$ 0.05
Jun 7 5:35:57	80 s	0.3956	g	17.38 $\pm$ 0.04
Jun 7 5:37:29	80 s	0.4211	g	17.31 $\pm$ 0.04
Jun 7 5:42:11	80 s	0.4994	g	17.27 $\pm$ 0.04
Jun 7 5:43:42	80 s	0.5247	g	17.36 $\pm$ 0.04
Jun 7 5:45:17	80 s	0.5511	g	17.33 $\pm$ 0.04
Jun 7 5:46:27	40 s	0.5706	g	17.37 $\pm$ 0.07
Jun 7 5:54:12	80 s	0.6997	g	18.04 $\pm$ 0.06
Jun 7 5:55:42	80 s	0.7247	g	18.04 $\pm$ 0.07
Jun 7 5:57:13	80 s	0.7500	g	18.05 $\pm$ 0.05
Jun 7 5:58:24	40 s	0.7697	g	18.15 $\pm$ 0.07
Jun 7 6:08:25	280 s	0.9367	g	18.52 $\pm$ 0.17
Jun 7 6:26:04	240 s	1.2307	g	18.41 $\pm$ 0.08
Jun 7 6:30:39	240 s	1.3071	g	18.41 $\pm$ 0.05
Jun 7 7:05:40	240 s	1.8907	g	19.20 $\pm$ 0.17
Jun 7 7:42:28	640 s	2.5042	g	19.48 $\pm$ 0.06
Jun 7 8:22:50	800 s	3.1768	g	19.74 $\pm$ 0.08
Jun 7 5:13:18	10 s	0.0181	r	15.98 $\pm$ 0.31
Jun 7 5:13:44	10 s	0.0253	r	15.75 $\pm$ 0.16
Jun 7 5:14:43	20 s	0.0417	r	14.34 $\pm$ 0.03
Jun 7 5:15:45	20 s	0.0589	r	14.32 $\pm$ 0.03
Jun 7 5:17:19	40 s	0.0850	r	14.68 $\pm$ 0.02
Jun 7 5:19:01	40 s	0.1133	r	15.11 $\pm$ 0.02

Table 7.7 (continued)

Mean Time (UT)	Exp. Time	Mean Δt (hr)	Filter	Magnitude
Jun 7 5:21:47	80 s	0.1594	r	15.47 $\pm$ 0.02
Jun 7 5:25:03	80 s	0.2139	r	16.04 $\pm$ 0.03
Jun 7 5:29:43	80 s	0.2917	r	16.60 $\pm$ 0.05
Jun 7 5:31:12	80 s	0.3164	r	16.57 $\pm$ 0.05
Jun 7 5:35:56	80 s	0.3953	r	16.57 $\pm$ 0.04
Jun 7 5:37:26	80 s	0.4203	r	16.75 $\pm$ 0.08
Jun 7 5:42:09	80 s	0.4989	r	16.69 $\pm$ 0.07
Jun 7 5:43:38	80 s	0.5236	r	16.60 $\pm$ 0.06
Jun 7 5:45:11	80 s	0.5494	r	16.64 $\pm$ 0.08
Jun 7 5:46:20	40 s	0.5686	r	16.78 $\pm$ 0.12
Jun 7 5:54:10	80 s	0.6992	r	17.25 $\pm$ 0.08
Jun 7 5:55:39	80 s	0.7239	r	17.37 $\pm$ 0.08
Jun 7 5:57:09	80 s	0.7489	r	17.37 $\pm$ 0.10
Jun 7 5:58:38	80 s	0.7736	r	17.54 $\pm$ 0.12
Jun 7 6:08:24	280 s	0.9365	r	17.65 $\pm$ 0.11
Jun 7 6:28:15	480 s	1.2672	r	17.69 $\pm$ 0.06
Jun 7 7:05:04	320 s	1.8810	r	18.44 $\pm$ 0.08
Jun 7 7:41:40	720 s	2.4909	r	18.77 $\pm$ 0.09
Jun 7 8:23:22	880 s	3.1859	r	19.04 $\pm$ 0.15
Jun 7 5:14:12	20 s	0.0331	i	14.75 $\pm$ 0.05
Jun 7 5:15:14	20 s	0.0503	i	14.05 $\pm$ 0.04
Jun 7 5:16:27	40 s	0.0706	i	14.20 $\pm$ 0.04
Jun 7 5:18:10	40 s	0.0992	i	14.76 $\pm$ 0.05
Jun 7 5:20:13	80 s	0.1333	i	15.01 $\pm$ 0.04
Jun 7 5:23:25	80 s	0.1867	i	15.61 $\pm$ 0.05
Jun 7 5:26:38	80 s	0.2403	i	15.99 $\pm$ 0.07
Jun 7 5:28:07	80 s	0.2650	i	16.23 $\pm$ 0.08
Jun 7 5:32:49	80 s	0.3433	i	16.34 $\pm$ 0.10
Jun 7 5:34:18	80 s	0.3681	i	16.43 $\pm$ 0.08

Table 7.7 (continued)

Mean Time (UT)	Exp. Time	Mean Δt (hr)	Filter	Magnitude
Jun 7 5:39:02	80 s	0.4469	i	16.48 $\pm$ 0.08
Jun 7 5:40:31	80 s	0.4717	i	16.53 $\pm$ 0.07
Jun 7 5:48:08	80 s	0.5986	i	16.68 $\pm$ 0.09
Jun 7 5:49:37	80 s	0.6233	i	16.60 $\pm$ 0.11
Jun 7 5:51:08	80 s	0.6486	i	16.79 $\pm$ 0.10
Jun 7 6:00:27	400 s	0.8038	i	17.33 $\pm$ 0.07
Jun 7 6:15:52	480 s	1.0609	i	17.46 $\pm$ 0.07
Jun 7 7:13:22	560 s	2.0190	i	18.32 $\pm$ 0.09
Jun 7 8:03:47	720 s	2.8594	i	18.94 $\pm$ 0.19

Analysis

Due to the speed of PROMPT's response, we were able to see the initial rise of the forward shock, a peak, and then a steep decline. Because of the four highly-sampled independent light curves, we are able to see at least two significant rebrightenings, although others may be suggested by the data. All magnitudes are converted to fluxes as prescribed by Bessell (1979) and Fukugita et al. (1995).

We model the afterglow as the sum of a series of three peaks consisting of a smoothly-broken rising and falling power law light curve and constant power law spectrum, where the spectrum is extinguished by both Milky Way and source frame dust and absorbed by hydrogen in the source frame and Lyα forest. Each of the three peaks is described by:

$$F_\nu(t) = e^{-\tau_\nu^{MW}} e^{-\tau_{\nu(1+z)}^{Ly\alpha}} e^{-\tau_{\nu(1+z)}^{source}} F_o \left(\frac{\nu}{\nu_o}\right)^{-\beta_n} \left[\left(\frac{t}{t_n}\right)^{-s_n\alpha_{1n}} + \left(\frac{t}{t_n}\right)^{-s_n\alpha_{2n}}\right]^{-1/s_n}. \quad (7.1)$$

τ_ν^{MW} is the Galactic extinction curve model of Cardelli et al. (1989), $\tau_{\nu(1+z)}^{Ly\alpha}$ is the Lyα forest absorption model of Reichart (2001a) taking into account the Lyα dampening wing using Eq 1 of Totani et al. (2006) and $\tau_{\nu(1+z)}^{source}$ is the source-frame

extinction curve and Lyman limit absorption model of Reichart (2001a). α_{1n} and α_{2n} are the two temporal indices of each peak, β_n is the spectral index, ν_o is the effective frequency of the r filter, t_n is the peak time of each component, F_n is the normalization of each component, and s_n is the smoothing parameter. We then integrate the sum of equation against the appropriate filter transmissivity curve before fitting it to the data.

Bayesian fits are performed similarly to the fits of GRB 021211 (§2.3), GRB 030115 (§3.1.3) and GRB 050408 (§3.2.3) and are described in detail in Section 2.3. Additional priors and the source-frame extinction curve model are detailed in Reichart (2001a) and are summarized in the same section. The Galactic extinction curve model (Cardelli et al. 1989) along this line of sight is a function of $E(B-V) = 0.029$ mag (Schlegel et al. 1998). Systematic calibration uncertainties are also added to the model and given a prior of ± 0.02 magnitudes.

Discussion

Using the definition of Jakobsson et al. (2004), GRB 060607 is a dark burst even though it has a bright optical afterglow. The optical to x-ray spectral index of GRB 060607 is -0.44 (limit is $\beta > -0.5$) because it has the brightest x-ray afterglow yet seen by *Swift* even though it lies at a redshift z = 3.082. Three peaks are evident in the γ-ray light curve, these consist of two overlapping FRED profiles from $t_0 - 5$ to $t_0 + 40$ seconds, and a third component at $\approx$100 seconds (Tueller et al. 2006). The PROMPT light curve overlaps this third γ-ray peak, and although it is sparsely sampled at this time, it does not exhibit corresponding morphology, neither are there parallel features between the optical and x-ray afterglow.

We fit the data to a general model and also for the standard model cases in both a wind and constant density medium, for ν_c above and below the optical, and modified for the various cases we consider for the two bumps in the light curve. Due to the lack of near-infrared data, we are unable to separate the

effects of extinction from the underlying spectral slope and so we set A_V to 0 mag for the fits, but we assume that the observed spectral slope is a combination of both. The results for the general case are summarized in Table 7.8. The observed temporal and spectral slope of the first peak are $\alpha = -1.35$ and $\beta = -1.38$. Neglecting extinction and using the observed temporal slope, the ISM & Wind Red ($\nu_c < \nu_{opt}$) imply $\beta = -1.24$ and hence is the most likely case, differing from the general model by only 0.9 σ. The ISM and Wind Blue cases predict $\beta = -0.92$ and -0.61, and differ at 2.9 σ and 4.9 σ respectively. But if we allow for extinction, as we ought to for a real physical model, then all cases are equally likely and differ only in the amount of extinction necessary to fit the observed spectral slope.

Table 7.8: GRB 060607: Best-Fit Parameter Values

	Variation		
	First	*Second*	*Third*
$\log F_0$ [μJy]	4.03	4.73	2.27
t [min]	3.01	41.53	64.32
α_1	2.17	9.29	3.28
α_2	-1.35	-24.82	-1.31
β	-1.38	-1.08	-0.82
s	1.73	0.12	9.75

The preliminary analysis of the x-ray observations found an exceptionally bright x-ray flux that is difficult to reconcile with the optical spectrum. Page et al. (2006a) report the x-ray afterglow to have $\alpha_x = -0.37$ and $\beta = -0.64$. This shallow x-ray spectral index implies $p = 1.28$ ($\nu_c < \nu_x$) or 2.28 ($\nu_c > \nu_x$). $p = 2.28$ implies α_x = -0.96 (ISM), -1.46 (Wind), but $p = 1.28$ implies α_x = -0.46 (ISM & Wind) that very closely matches the observed α_x. A value of $p = 1.28$ would require a complex electron energy distribution akin to that found for GRB 021211, for the shock to contain only a finite amount of energy (§2, Bhattacharya

2001; Nysewander et al. 2005b). Hence is it likely that ν_c lies below the x-ray, and may lie between optical and x-ray frequencies.

After we consider the general, free parameter case then we add constraints that test (1) the passage of breaks, (2) density enhancements, (3) a series of two energy injection episodes, and (4) one energy injection episode with a bright reverse shock preceding it. For the first scenario – the passage of spectral breaks – we test to see if there are any permanent changes in the spectral index before and after the bumps (null test: $\beta_1 = \beta_3$). If the bumps are due to density enhancements, then the spectral index will not change throughout the entire series of bumps ($\beta_1 = \beta_2 = \beta_3$). If the bumps are due to two episodes of energy injection, then the fading slope of each bump will be the same ($\alpha_1 = \alpha_2 = \alpha_3$) along with the spectral slope ($\beta_1 = \beta_2 = \beta_3$). For a single episode of energy injection with a bright, rapidly fading reverse shock, the first and last bumps will have the same temporal and spectral indices ($\alpha_1 = \alpha_3$; $\beta_1 = \beta_3$), and the middle bump will have a steep temporal index ($\alpha_2 \geq 2$).

Spectral breaks

β_1 = -1.38, β_2 = -1.08 and β_3 = -0.82. A model with $\beta_1 = \beta_3$ differs from the general model at the 2.3 σ level. If we treat the change in spectral slope as real and assume that the features in the light curve result from the movement of the cooling break from above to below the optical frequencies, then we find consistent values for p above and below the break (p = 1.76 & 1.64). However, assuming p = 1.7, we do not find values consistent with the observed temporal indices. For p = 1.7 the initial slope would be α = -0.53 (ISM) or -1.03 (Wind) that would change to α = -0.78 after passage of the break.

Density Variations

Density enhancements will increase the flux in the afterglow before it asymptotically returns to the extrapolation of the previous light curve. This behavior

seems to describe the morphology of the first superimposed variation, but not in the second one after which the light curve renormalizes with the same initial slope. In this scenario, we can impose each of the three variations to have the same spectral slope ($\beta_1 = \beta_2 = \beta_3$). We find that this condition rules out the model at only the 2.7 σ level, but because of the lack of asymptotic behavior, this scenario is unlikely.

Additionally, variations in the external density only produce variations in the light curve when ν_c is below the observed frequency (Nakar et al. 2003), hence we would be in the ISM or Wind Red scenario, which is the preferred model when neglecting any possible extinction. However, it is difficult for density models (Lazzati et al. 2002b) to produce sharp variations that may make this model less likely. A comparison with the unpublished x-ray afterglow would be useful to test this scenario.

Energy Injection

During an energy injection, the light curve chromatically rises momentarily, but then fades again at the same pace as it did before the variation. We impose this condition on the afterglow by setting $\alpha_1 = \alpha_2 = \alpha_3$ and $\beta_1 = \beta_2 = \beta_3$. This model is unable to find physical solutions because of the extremely steep slope needed to fit the second fading rate, and it is ruled out at the 6.2 σ level.

Instead, we find that the most likely scenario is that of an episode of energy injection that was preceded by a reverse shock. In this scenario, $\alpha_1 = \alpha_3$ and $\beta_1 = \beta_3$, and requires that α_2 be steep, to match the expected reverse shock slope. This scenario is consistent with the general model at the 2.3 σ level, but more importantly, it should be noted that the requirements on the latter temporal slope only slightly add to this significance. In the general model, $\alpha_1 \approx \alpha_3 \approx$ -1.35, and we find that $\alpha_2 <$ -3 at the 3 σ level. Because the initial forward shock of GRB optical afterglows is not typically seen also in the x-rays, it is unlikely that latter refreshed shocks would produce any corresponding x-ray features.

Again, comparison with the *Swift* XRT afterglow would be helpful.

Patchy Shell

The patchy shell model was outright rejected for GRB 030329 because the bumps occurred after the jet break time. In GRB 060607, clearly these are happening early on in the afterglow lifetime and hence occur well before the jet break. We impose the same constraints as that of the density enhancements ($\beta_1 = \beta_2 = \beta_3$) and find the same significance. The features in this model are very similar to those for density variations, and so a more detailed modeling effort is needed to determine the significance of this model, but a preliminary analysis finds it to be acceptable. However, unlike density variations, the patchy shell model produces variations both above and below ν_c.

Significant variations such as those we see in GRB 060607 are present in many of our most well-sampled afterglow light curves. Without these dense, multi-band light curves, it is likely that we will consistently underestimate the true temporal slope, which is one of the primary inputs to determining the properties of an afterglow. Rebrightenings or variable energy in the jet can also significantly change the total GRB energy. Without understanding these basic properties of the afterglow, it is difficult to produce correct results through modeling efforts.

7.8 GRB 060719

This burst would have been labeled a "dark burst" were it not for the efforts of groups with large telescopes (8.2-m VLT) following up at early times (23 minutes). The afterglow was highly reddened ($\beta = -2.2 \pm 0.2$; Malesani et al. 2006b), and illustrates the importance of the next phase of PROMPT: rapid-time NIR observations. Reports in the GCN Circulars (Fugazza et al. 2006) suggest that the afterglow may have been near $R \approx 24$ – 25^{th} magnitude within an hour after the burst, while brighter in the near-infrared, with $K \approx 19$ – 20^{th}

magnitude. PROMPT did not detect this afterglow, and because no magnitude has been reported, it is unclear whether or not the limits presented here are constraining, but with upcoming near-infrared coverage, PROMPT will certainly detect similar future highly-reddened afterglows.

Observations

The *Swift* BAT localized GRB 060719 on July 19^{th} 2006, at 06:50:36 UT and sent out a GCN alert 21 seconds after the trigger. XRT quickly slewed to the GRB site and found a bright, fading x-ray source with an initial flux of 2.7 $\times$ 10^{-9} erg cm^2 s^{-1} (0.2 – 10 keV) (Stamatikos et al. 2006). Both the gamma-ray and x-ray light curve exhibit two early flares (Sakamoto et al. 2006), and the x-ray light curve follows a shallow initial slope of $\alpha \approx$ -0.2 $\pm$ 0.1 breaking to a steeper slope of $\alpha \approx$ -1.3 $\pm$ 0.3 at 6.9 $\pm$ 1.7 ks (Conciatore et al. 2006).

No fading optical counterpart was found by the UVOT. Berger & Bonanos (2006) found a possible counterpart in deeper imaging, but spectroscopy confirmed it to be a regular foreground star (Fugazza et al. 2006). A second possible counterpart was found (Malesani et al. 2006b) that appeared very red (R – K $\approx$ 4.5 $\pm$ 0.2), and after comparing images taken on the second night, was confirmed to be the afterglow. The source faded by two magnitudes between 3.3 hours and 1.1 days (Malesani et al. 2006a), a rate of α = -0.9 $\pm$ 0.1.

PROMPT Observations

Under the control of SkyNet, three PROMPT telescopes observed the location of GRB 060719 beginning 36 seconds after the burst (15 seconds after the GCN trigger) in Bessell U and Sloan riz filters (Nysewander et al. 2006d). No optical counterpart to the afterglow was seen down to 3σ limiting magnitudes presented in Table 7.9. Later images were stacked to improve depth, but care was taken to create appropriate stacks of images within the GRB exposure sequence. Images were reduced using IRAF's CCDPROC, photometered using IRAF's DIGIPHOT

package and calibrated to the USNO-B1.0 and Tycho-2 catalogues. $BVRI$ magnitudes were transformed to Sloan riz using the transformation equations of Smith et al. (2002).

Table 7.9: PROMPT Observations of the Field of GRB 060719

Mean Time (UT)	Exp. Time	Mean Δt (hr)	Filter	Magnitude
Jul 19 6:51:15	5 s	0.0107	r	> 17.0
Jul 19 6:52:43	15 s	0.0353	r	> 18.0
Jul 19 6:55:34	70 s	0.0828	r	> 19.3
Jul 19 7:01:28	160 s	0.1811	r	> 20.0
Jul 19 7:09:55	320 s	0.3221	r	> 20.9
Jul 19 7:26:38	640 s	0.6006	r	> 21.2
Jul 19 6:51:36	10 s	0.0167	i	> 17.8
Jul 19 6:52:07	30 s	0.0254	i	> 18.5
Jul 19 6:54:06	60 s	0.0583	i	> 19.5
Jul 19 6:57:22	120 s	0.1129	i	> 20.3
Jul 19 7:03:01	160 s	0.2071	i	> 20.4
Jul 19 7:13:00	320 s	0.3733	i	> 21.0
Jul 19 7:35:10	480 s	0.7427	i	> 21.1
Jul 19 6:51:16	5 s	0.0113	z	> 16.8
Jul 19 6:51:43	15 s	0.0187	z	> 17.7
Jul 19 6:52:28	20 s	0.0313	z	> 18.3
Jul 19 6:53:33	50 s	0.0492	z	> 18.9
Jul 19 6:56:02	120 s	0.0906	z	> 19.7
Jul 19 7:00:24	240 s	0.1634	z	> 20.2
Jul 19 7:10:40	640 s	0.3344	z	> 21.0

Upper limits are 3σ.

Discussion

Because no absolute magnitude was given in the GCN Circular Archive, we are unable to extrapolate the slope of the light curve back to early times to in

order to determine if the limits presented in Table 7.9 are constraining. Given that this object is highly reddened (R – K = 4.5 ± 0.2; Malesani et al. 2006b), it is likely that the z-band would yield the most meaningful constraining limits, even though its set of limits is slightly shallower than i. Using $i > 19.5$ at 0.06 hours and the x-ray flux and decay rate reported by Conciatore et al. (2006), the optical to x-ray spectral slope at 11 hours is $\beta > -0.37$ assuming an optical temporal index of α = -1.0. For $z > 19.7$ at 0.16 hours, $\beta >$ -0.41. If the near-infrared afterglow had not been discovered, GRB 060719 would have been labelled a dark burst, although due to the afterglow discovery it is considered *dim*.

The color given in (Malesani et al. 2006b) translates to a spectral slope between the R & K bands of $\beta = -2.2 \pm 0.2$. An object this highly reddened is surely either at high-redshift or highly-extinguished. Although faint, the object was detected in the R-band in (Fugazza et al. 2006) with the VLT, so if it were faint due to redshift, the Lyman α drop out must cross into the R-band, which places a limit on the redshift of z $\simeq$ 4. Based on J-band observations, Malesani et al. (2006b) say that the object does not exhibit a steep break in spectral slope that suggests, which the reddening is instead due to extinction.

7.9 GRB 060908

Exactly one year after PROMPT had its first rapid-response of an afterglow, GRB 050908, it triggered on GRB 060908 and was able to slew all four telescopes to the field and begin observing after 63 seconds. Early morning clear skies allowed PROMPT to observe the incredibly bright optical afterglow ($r \approx 14.9$ at 85 s) for an hour before the sun rose in Chile. Instead of observing the peak of the forward shock as in GRB 060607 (§7.7) PROMPT caught a bright, fading optical flash. Variations in the afterglow seem chromatic and very similar to those found by Nysewander et al. (2005b) in the afterglow of GRB 021211.

Observations

At 08:57:22 UT on September 9^{th} 2006, *Swift* BAT triggered on the long (19 second) GRB 060908, which was a triply peaked, bright gamma-ray burst (Evans et al. 2006a; Palmer et al. 2006). At 72 seconds, the XRT observed the x-ray afterglow, which was found to be fading as a power-law with slope α = -1.11 $\pm$ 0.06 (Evans et al. 2006b), and further localized the burst to 4 arcseconds. UVOT observed the site and found a very bright fading optical counterpart with an unfiltered magnitude of $\approx$ 15.1.

Nysewander et al. (2006c) independently found the bright optical afterglow with PROMPT and reported the source soon after the *Swift* findings were distributed. Further optical measurements were made: seven minutes after the burst, REM began optical observations in VRI, and at 36 minutes, the Danish 1.5m began observations and reported a temporal slope of the afterglow of -1.06 $\pm$ 0.11 between 36 and 70 minutes. UVOT detected the burst in four of six filters, and was able to rapidly give a photometric redshift determination of 0.26 $<$ z $<$ 2.20 (Morgan et al. 2006). Rol et al. (2006b) later used Gemini North to obtain a spectroscopic redshift of z = 2.43 $\pm$ 0.05.

PROMPT Observations

An hour before dawn, PROMPT began observations with four telescopes in $Ugriz$ beginning at 63 seconds when the burst was at $g \approx 15.1$ and lasting for nearly an hour during which the afterglow had faded over four magnitudes to $g \approx$ 19.3. Although the burst was initially bright, it quickly faded below the detection threshold of individual $griz$ images, and hence later images are stacked to enhance signal-to-noise. Images were reduced using IRAF's CCDPROC package and psf photometered using IRAF's DAOPHOT package. Each filter was calibrated to the $griz$ magnitudes of field stars found in the SDSS. The observations are summarized in Table 7.10 and plotted in Figure 7.6.

Table 7.10: PROMPT Observations of the Afterglow of GRB 060908

Mean Time (UT)	Exp. Time	Mean Δt (hr)	Filter	Magnitude
Sept 08 8:58:31	10 s	0.0192	g	15.07 $\pm$ 0.03
Sept 08 8:58:57	10 s	0.0264	g	15.35 $\pm$ 0.04
Sept 08 8:59:18	10 s	0.0322	g	15.70 $\pm$ 0.03
Sept 08 8:59:45	20 s	0.0397	g	15.96 $\pm$ 0.04
Sept 08 9:00:19	20 s	0.0492	g	16.28 $\pm$ 0.04
Sept 08 9:00:45	10 s	0.0564	g	16.48 $\pm$ 0.10
Sept 08 9:01:22	40 s	0.0667	g	16.67 $\pm$ 0.03
Sept 08 9:02:12	40 s	0.0806	g	16.77 $\pm$ 0.04
Sept 08 9:03:04	40 s	0.0950	g	17.03 $\pm$ 0.06
Sept 08 9:03:55	40 s	0.1092	g	17.09 $\pm$ 0.09
Sept 08 9:05:06	80 s	0.1289	g	17.68 $\pm$ 0.12
Sept 08 9:06:42	80 s	0.1556	g	17.65 $\pm$ 0.09
Sept 08 9:08:16	80 s	0.1817	g	18.04 $\pm$ 0.07
Sept 08 9:09:50	80 s	0.2078	g	17.84 $\pm$ 0.04
Sept 08 9:11:23	80 s	0.2336	g	18.14 $\pm$ 0.05
Sept 08 9:12:57	80 s	0.2597	g	18.16 $\pm$ 0.04
Sept 08 9:14:28	80 s	0.2850	g	18.25 $\pm$ 0.07
Sept 08 9:16:01	80 s	0.3108	g	18.39 $\pm$ 0.17
Sept 08 9:17:32	80 s	0.3361	g	18.47 $\pm$ 0.12
Sept 08 9:19:04	80 s	0.3617	g	18.57 $\pm$ 0.17
Sept 08 9:20:34	80 s	0.3867	g	18.53 $\pm$ 0.17
Sept 08 9:22:06	80 s	0.4122	g	18.84 $\pm$ 0.12
Sept 08 9:23:36	80 s	0.4372	g	18.71 $\pm$ 0.17
Sept 08 9:25:10	80 s	0.4633	g	18.44 $\pm$ 0.10
Sept 08 9:26:40	80 s	0.4883	g	18.91 $\pm$ 0.13
Sept 08 9:29:39	200 s	0.5381	g	19.04 $\pm$ 0.15
Sept 08 9:33:30	160 s	0.6022	g	18.87 $\pm$ 0.11
Sept 08 9:36:33	80 s	0.6528	g	19.00 $\pm$ 0.15
Sept 08 9:40:15	240 s	0.7147	g	19.15 $\pm$ 0.11
Sept 08 9:44:17	240 s	0.7819	g	19.06 $\pm$ 0.09
Sept 08 9:48:51	240 s	0.8581	g	19.06 $\pm$ 0.12

Table 7.10 (continued)

Mean Time (UT)	Exp. Time	Mean Δt (hr)	Filter	Magnitude
Sept 08 9:54:11	320 s	0.9469	g	19.25 ± 0.20
Sept 08 8:58:47	10 s	0.0236	r	14.86 ± 0.05
Sept 08 8:59:17	20 s	0.0319	r	15.28 ± 0.05
Sept 08 9:00:17	10 s	0.0486	r	15.79 ± 0.11
Sept 08 9:01:27	40 s	0.0681	r	16.44 ± 0.10
Sept 08 9:03:04	40 s	0.0950	r	16.69 ± 0.12
Sept 08 9:05:10	80 s	0.1300	r	17.12 ± 0.07
Sept 08 9:08:18	80 s	0.1822	r	17.54 ± 0.14
Sept 08 9:11:25	80 s	0.2342	r	17.85 ± 0.18
Sept 08 9:16:48	160 s	0.3239	r	18.10 ± 0.15
Sept 08 9:22:49	80 s	0.4242	r	18.25 ± 0.18
Sept 08 9:32:01	160 s	0.5775	r	18.41 ± 0.17
Sept 08 9:34:54	160 s	0.6256	r	18.40 ± 0.19
Sept 08 9:45:05	320 s	0.7953	r	19.19 ± 0.15
Sept 08 8:59:49	20 s	0.0408	i	15.67 ± 0.05
Sept 08 9:00:45	20 s	0.0564	i	15.88 ± 0.08
Sept 08 9:02:10	20 s	0.0800	i	16.71 ± 0.26
Sept 08 9:03:57	40 s	0.1097	i	16.78 ± 0.06
Sept 08 9:06:44	80 s	0.1561	i	17.33 ± 0.10
Sept 08 9:09:52	80 s	0.2083	i	17.58 ± 0.11
Sept 08 9:12:59	80 s	0.2603	i	17.68 ± 0.16
Sept 08 9:14:30	80 s	0.2856	i	17.59 ± 0.16
Sept 08 9:19:09	80 s	0.3631	i	17.85 ± 0.15
Sept 08 9:25:12	80 s	0.4639	i	17.97 ± 0.13
Sept 08 9:26:43	80 s	0.4892	i	17.92 ± 0.24
Sept 08 9:28:50	160 s	0.5244	i	18.22 ± 0.22
Sept 08 9:39:31	320 s	0.7025	i	18.73 ± 0.19
Sept 08 8:58:27	5 s	0.0182	z	14.35 ± 0.09
Sept 08 8:58:45	10 s	0.0231	z	14.61 ± 0.09
Sept 08 8:59:17	20 s	0.0319	z	15.15 ± 0.06
Sept 08 8:59:47	20 s	0.0403	z	15.32 ± 0.07

Table 7.10 (continued)

Mean Time (UT)	Exp. Time	Mean Δt (hr)	Filter	Magnitude
Sept 08 9:00:18	20 s	0.0489	z	15.65 $\pm$ 0.07
Sept 08 9:00:44	10 s	0.0561	z	16.01 $\pm$ 0.21
Sept 08 9:01:21	40 s	0.0664	z	15.91 $\pm$ 0.10
Sept 08 9:02:12	40 s	0.0806	z	16.33 $\pm$ 0.09
Sept 08 9:03:02	40 s	0.0944	z	16.25 $\pm$ 0.14
Sept 08 9:03:54	40 s	0.1089	z	16.63 $\pm$ 0.15
Sept 08 9:06:41	160 s	0.1553	z	16.96 $\pm$ 0.17
Sept 08 9:10:37	160 s	0.2208	z	17.15 $\pm$ 0.14
Sept 08 9:19:49	400 s	0.3741	z	18.20 $\pm$ 0.21
Sept 08 9:33:29	640 s	0.6019	z	18.18 $\pm$ 0.19

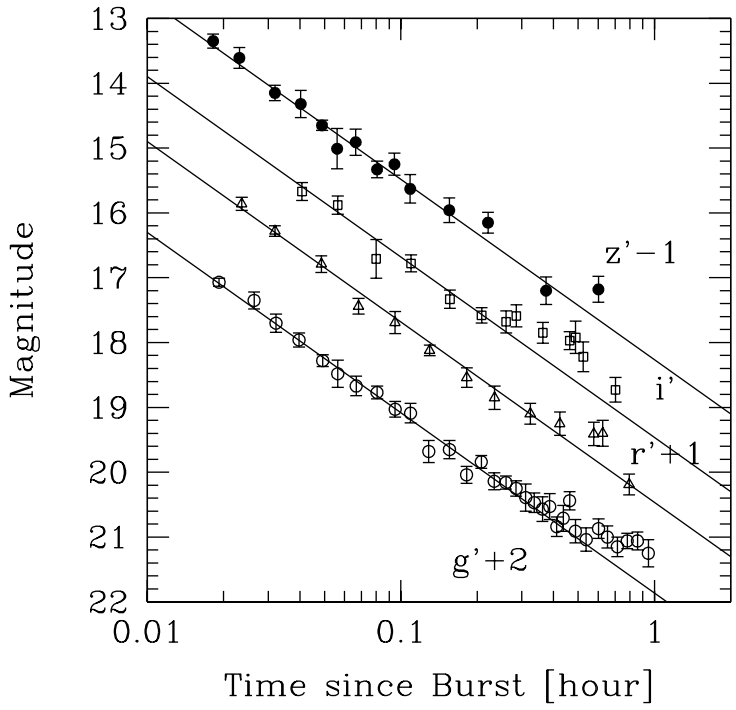

Figure 7.6: The *griz* afterglow of GRB 060908 from 63 seconds to almost 50 minutes after the burst. The lines show the underlying afterglow upon which the chromatic variations are superimposed.

Discussion

Although we did not witness the rise of the reverse shock, the lack of a rapidly fading initial slope (typical reverse shocks have $\alpha \approx -2$) suggests that we did not catch reverse shock emission. The light curve is difficult to model due to the fact that there is a shallowing of slope to $\alpha \approx$ -0.6 observed in the ri filters that is clearly not observed in the g filter. This behavior is similar to the chromatic variations observed by Nysewander et al. (2005b) in the light curve of GRB 021211, although in this case, it is much more highly sampled. Additional data at later times will be needed to test this possibility.

The spectral flux distribution of the afterglow has a power-law slope of $\beta \approx$ -0.8. Careful modeling must be done because at a redshift of z = 2.43 $\pm$ 0.05, the Lyman α break occurs within the g-band, so this slope will be steeper than the true slope. Given this and the early temporal slope α of -1.2, the most likely scenario is that of a constant density medium, with ν_c blueward of the optical. The wind-swept case with $\nu_c > \nu_{opt}$ is also viable if there is extinction within the host galaxy, which may be suggested by the slight curvature of the spectrum.

Chapter 8

Conclusions

The standard model has provided an acceptable fit to the broadband afterglow spectrum and light curve for long-duration GRBs. However, we often see glaring discrepancies at optical wavelengths - the optical afterglows of gamma-ray bursts vary over many magnitudes of brightness, and act seemingly indepedent of the γ-ray and x-ray emission. The large sample of GRB afterglows resulting from *Swift* triggers will allow astronomers to better study the statistics of the population. Here we have presented an exploratory study based on a number of example cases of dark and dim bursts from both the pre and post-*Swift* era. By examining the bursts within the context of the standard model, we can test its strengths and limitations.

Dark gamma-ray burst afterglows are commonly attributed to one or a combination of four reasons: (1) the burst lies at high redshift, (2) the burst is highly extinguished, (3) the burst exploded in a low-density region, and (4) the burst is intrinsically dim due to micro-physical properties of the progenitor or the isotropic-equivalent total energy of the explosion itself. In this work we have explored a number specific γ-ray bursts that are dark and dim due to these reasons. GRB 050904 was dark due to high-redshift – it had a bright afterglow that was absorbed at optical frequencies due to the Lyman α forest. GRB 030115 was dim due to a large amount of host galaxy extinction, presumably from the en-

vironment of the progenitor itself. GRB 050408 was dimmed by extinction, and although it is not a very dim burst, it illustrates the continuum of dark and dim optical afterglows caused by extinction. GRB 021211 is dim due most likely to a combination of reasons: (1) a low fraction of energetic electrons in the jet, (2) a low external density, (3) a wide jet, and perhaps (4) a small amount of source frame extinction. Furthermore, the jet seems magnetically dominated, $\epsilon_B \gg \epsilon_e$ and far from equipartition. GRB 051022 and GRB 060306 are truly dark bursts, with no detected optical afterglow although both had clearly observed x-ray afterglows and for GRB 051022, a radio afterglow. Both bursts show large values of neutral hydrogen in their x-ray spectra characteristic of giant molecular clouds, which suggests high optical extinction assuming typical dust to gas ratios.

Due to the success of *Swift* and as we, along with the GRB community, have improved our ground-based efforts, no longer are the majority of bursts considered dark. Instead, with deep rapid responses from facilities such as PROMPT, we are able to better differentiate between the *dim* and *dark* afterglows. Five years ago, the typical response time to a GRB was half a day, and then, only to moderate depths. Now, each GRB usually has one or more rapid response ground-based telescopes chasing it on the tens of seconds timescale, and large-aperture telescopes often chase bursts after only minutes or hours. PROMPT's unique design to observe γ-ray burst afterglows simultaneously in multiple filters allows us to study in fine detail early afterglows on a scale which has not yet been attempted. We can now ask and possibly answer very specific questions about chromatic variations of the early afterglow and the color and evolution of the reverse shock. We can reconstruct extinction curves of the early afterglow and obtain photometric redshifts through drop-out in the spectral flux distribution.

As proof of concept, I offer a summary of the initial successes of PROMPT in its first year of operations. PROMPT has responded to eight bursts on the rapid timescale and successfully began observations only tens of seconds after the initial flash of γ-ray emission. Five of these are likely extinguished: GRB 060428A was

clearly dark due to extinction located within the Galactic Plane, the dim GRBs 060719, 051109A and bright GRB 060418 all show curved, extinguished spectral distributions, and the dark GRB 060306 is likely dark due to a combination of moderate redshift and host galaxy extinction which was indicated by its x-ray spectrum. GRB 050908 does not show extinction, but instead has a clear break due to the Lyman α forest and Lyman limit that illustrates PROMPT's power to measure photometric redshifts. For GRB 060607, the rapid response allowed the optical light curve to overlap the GRB itself, and later, significant and possibly achromatic variations occur. GRB 060908 was an extremely bright afterglow that shows a clear achromatic bump during the first hour in its highly-sampled light curve. These two bursts have bright, fascinating afterglows that are not well described by the standard model alone, and have afterglows that we can use to test the physical properties of the progenitor and environment itself. For this work, we have presented dark and dim bursts that are not well described by the standard model merely due to their observed brightnesses. GRB 060607 and GRB 060908 challenge the model one step further by providing fluctations in their light curves for us to study which are not predicted by the simplest scenarios. With a rate of one rapid response every two months, PROMPT will surely continue to catch exciting, previously unobserved features of the early emission and expand the limits of γ-ray burst research.

REFERENCES

Abel, T., Bryan, G. L., & Norman, M. L. 2000, ApJ, 540, 39

—. 2002, Science, 295, 93

Akerlof, C. et al. 1999, Nature, 398, 400

Angelini, L. et al. 2006, GRB Coordinates Network, 4848, 1

Atteia, J. L., Boer, M., & Klotz, A. 2003, GRB Coordinates Network, 1810, 1

Barthelmy, S. D. et al. 2005, Nature, 438, 994

Beardmore, A. P., Godet, O., & Sakamoto, T. 2006, GRB Coordinates Network, 5209, 1

Becker, R. H. et al. 2001, AJ, 122, 2850

Beloborodov, A. M. 2000, ApJ, 539, L25

Berger, E., & Bonanos, A. 2006, GRB Coordinates Network, 5340, 1

Berger, E. et al. 2006, ArXiv Astrophysics e-prints

Berger, E., & Frail, D. A. 2003, GRB Coordinates Network, 1817, 1

Berger, E., Gladders, M., & Oemler, G. 2005a, GRB Coordinates Network, 3201, 1

Berger, E. et al. 2002, ApJ, 581, 981,147

—. 2005b, ApJ, 634, 501

—. 2003, Nature, 426, 154

—. 2005c, Nature, 438, 988

Bessell, M. S. 1979, PASP, 91, 589

Bessell, M. S., & Brett, J. M. 1988, PASP, 100, 1134

Bhattacharya, D. 2001, Bulletin of the Astronomical Society of India, 29, 107

Bikmaev, I. et al. 2005, GRB Coordinates Network, 3262, 1

Björnsson, C.-I., & Fransson, C. 2004, ApJ, 605, 823

Björnsson, G., Gudmundsson, E. H., & J´ohannesson, G. 2004, ApJ, 615, L77

Björnsson, G., Hjorth, J., Pedersen, K., & Fynbo, J. U. 2002, ApJ, 579, L59

Blake, C., Lamb, D. Q., Barentine, J., Dembicky, J., McCall, B., York, D. G., & McMillan, R. 2003, GRB Coordinates Network, 1808, 1

Bloom, J. S. 2005, GRB Coordinates Network, 4212, 1

Bloom, J. S., Frail, D. A., & Kulkarni, S. R. 2003, ApJ, 594, 674

Bloom, J. S. et al. 1999, Nature, 401, 453

Blustin, A. J. et al. 2006, ApJ, 637, 901

Böer, M., Atteia, J. L., Damerdji, Y., Gendre, B., Klotz, A., & Stratta, G. 2006, ApJ, 638, L71

Brainerd, J. J. 1992, ApJ, 355, 522

Briggs, M. S. et al. 1996, ApJ, 459, 40

Bromm, V., Coppi, P. S., & Larson, R. B. 1999, ApJ, 527, L5,148

—. 2002, ApJ, 564, 23

Bromm, V., & Loeb, A. 2002, ApJ, 575, 111

Butler, N. R., Ricker, G. R., Lamb, D. Q., Burrows, D. N., Racusin, J., & Gehrels, N. 2005a, GRB Coordinates Network, 4165, 1

—. 2005b, GRB Coordinates Network, 4170, 1

Calzetti, D., Kinney, A. L., & Storchi-Bergmann, T. 1994, ApJ, 429, 582

Calzoletti, L. et al. 2006, GRB Coordinates Network, 5356, 1

Cameron, P. B., & Frail, D. A. 2005, GRB Coordinates Network, 4154, 1

Campana, S., Mineo, T., Tagliaferri, G., Mangano, V., & Romano, P. 2005, GRB Coordinates Network, 4229, 1

Capalbi, M. et al. 2006, ArXiv Astrophysics e-prints

Cardelli, J. A., Clayton, G. C., & Mathis, J. S. 1989, ApJ, 345, 245

Castro-Tirado, A. J., Gorosabel, J., Casanova, V., Garcia-Lobo, E., Castro Cerón, J. M., de Ugarte, A., Fynbo, J., & Rol, E. 2003, GRB Coordinates Network, 1807, 1

Cenko, S. B., Fox, D. B., & Berger, E. 2005a, GRB Coordinates Network, 3944, 1

Cenko, S. B., Fox, D. B., McNaught, R., & Peterson, B. 2005b, GRB Coordinates Network, 4134, 1

Chandra, P., Ray, A., & Bhatnagar, S. 2004, ApJ, 612, 974

Chen, H.-W. et al. 2006, GRB Coordinates Network, 4861, 1

Chevalier, R. A., & Li, Z.-Y. 2000, ApJ, 536, 195

Chevalier, R. A., Li, Z.-Y., & Fransson, C. 2004, ApJ, 606, 369

Chincarini, G. et al. 2005, ArXiv Astrophysics e-prints

Chincharini, G. et al. 2005, GRB Coordinates Network, 3209, 1

Cobb, B. E. 2006, GRB Coordinates Network, 5111, 1

Coburn, W., & Boggs, S. E. 2003, Nature, 423, 415

Conciatore, M. L., Capalbi, M., Perri, M., Vetere, L., Burrows, D. N., & Stamatikos, M. 2006, GRB Coordinates Network, 5348, 1

Costa, E. et al. 1997, Nature, 387, 783

Covino, S. et al. 2006a, GRB Coordinates Network, 4967, 1

Covino, S., Capalbi, M., Perri, M., Mangano, V., & Burrows, D. N. 2005, GRB Coordinates Network, 3508, 1

Covino, S. et al. 2006b, GRB Coordinates Network, 5234, 1

Crew, G. et al. 2002, GRB Coordinates Network, 1734, 1

Crew, G. B. et al. 2003, ApJ, 599, 387

Cummings, J. et al. 2006, GRB Coordinates Network, 4975, 1

Curran, P. A., Kann, D. A., Ferrero, P., Rol, E., & Wijers, R. A. M. J. 2006, ArXiv Astrophysics e-prints

Dado, S., Dar, A., & De Rújula, A. 2003, ApJ, 593, 961

Dai, Z. G., & Lu, T. 2002, ApJ, 565, L87

Daigne, F., Rossi, E. M., & Mochkovitch, R. 2006, ArXiv Astrophysics e-prints

de Pasquale, M., & Angelini, L. 2006, GRB Coordinates Network, 4852, 1

de Pasquale, M., Goad, M., Blustin, A. J., Chester, M., Angelini, L., & Gehrels, N. 2005, GRB Coordinates Network, 3960, 1

de Pasquale, M., & Mangano, V. 2006, GRB Coordinates Network, 5024, 1

de Pasquale, M. et al. 2003, ApJ, 592, 1018

de Ugarte Postigo, A. et al. 2005a, Astronomy & Astrophysics, 443, 841

—. 2005b, GRB Coordinates Network, 3193, 1

Della Valle, M. et al. 2003, A&A, 406, L33

Dickey, J. M., & Lockman, F. J. 1990, ARAA, 28, 215

Djorgovski, S. G., Frail, D. A., Kulkarni, S. R., Bloom, J. S., Odewahn, S. C., &

Diercks, A. 2001, ApJ, 562, 654

Djorgovski, S. G. et al. 1997, Nature, 387, 876

Doty, J. et al. 2005, GRB Coordinates Network, 4145, 1

Dupree, A. K., Falco, E., Prochaska, J. X., Chen, H.-W., & Bloom, J. S. 2006, GRB Coordinates Network, 4969, 1

Evans, P. A. et al. 2006a, GRB Coordinates Network, 5544, 1

Evans, P. A., Beardmore, A. P., Godet, O., & Page, K. L. 2006b, GRB Coordinates Network, 5554, 1

Falcone, A. D., Barthelmy, S. D., Burrows, D. N., Cummings, J. R., Gehrels, N.,

Hunsberger, S. D., Kennea, J. A., & Palmer, D. M. 2006a, GRB Coordinates Network, 4966, 1

Falcone, A. D., Burrows, D. N., & Kennea, J. 2006b, GRB Coordinates Network, 4973, 1

Fenimore, E. et al. 2005, GRB Coordinates Network, 4217, 1

Fitzpatrick, E. L., & Massa, D. 1988, ApJ, 328, 734

Flaccomio, E., Garnavich, P., & Stanek, K. 2003, GRB Coordinates Network, 1806, 1

Foley, R. J., Chen, H.-W., Bloom, J. S., & Prochaska, J. X. 2005, GRB Coordinates Network, 3949, 1

Foley, R. J. et al. 2006, ApJ, 645, 450

Fox, D., & Cenko, B. 2006, GRB Coordinates Network, 3912, 1

Fox, D. W., & Price, P. A. 2002, GRB Coordinates Network, 1731, 1

Fox, D. W. et al. 2003a, ApJ, 586, L5

—. 2003b, Nature, 422, 284

Frail, D. A., & Berger, E. 2003, GRB Coordinates Network, 1827, 1

Frail, D. A. et al. 2001, ApJ, 562, L55

Frail, D. A., Kulkarni, S. R., Shepherd, D. S., & Waxman, E. 1998, ApJ, 502, L119+

Fruchter, A., Krolik, J. H., & Rhoads, J. E. 2001, ApJ, 563, 597

Fruchter, A., Levan, A., Vreeswijk, P., Holland, S. T., & Kouveliotou, C. 2002, GRB Coordinates Network, 1781, 1

Fruchter, A. S. et al. 2006, Nature, 441, 463

Fryer, C. L. 1999, ApJ, 522, 413

Fugazza, D. et al. 2005, GRB Coordinates Network, 3948, 1

Fugazza, D., Malesani, D., & Covino, S. 2006, GRB Coordinates Network, 5347, 1

Fukugita, M., Ichikawa, T., Gunn, J. E., Doi, M., Shimasaku, K., & Schneider, D. P. 1996, AJ, 111, 1748

Fukugita, M., Shimasaku, K., & Ichikawa, T. 1995, PASP, 107, 945

Fynbo, J. U. et al. 2001, A&A, 369, 373

Gal-Yam, A., Berger, E., Fox, D. B., Soderberg, A. M., Cenko, S. B., Cameron, P. B., & Frail, D. A. 2005, GRB Coordinates Network, 4156, 1

Galama, T. J. et al. 2003, ApJ, 587, 135

—. 1998, Nature, 395, 670

Galama, T. J., & Wijers, R. A. M. J. 2001, ApJ, 549, L209

Gehrels, N. et al. 2005, Nature, 437, 851

Gnedin, N. Y., & Ostriker, J. P. 1997, ApJ, 486, 581

Goad, M. et al. 2005a, GRB Coordinates Network, 3942, 1

Goad, M., Pagani, C., Page, K., & Burrows, D. 2005b, GRB Coordinates Network, 3946, 1

Goad, M., Page, K., & Burrows, D. 2005c, GRB Coordinates Network, 3952, 1

Golenetskii, S., Aptekar, R., Mazets, E., Pal'Shin, V., Frederiks, D., Ulanov, M., & Cline, T. 2006, GRB Coordinates Network, 4989, 1

Gordon, K. D., & Clayton, G. C. 1998, ApJ, 500, 816

Granot, J., Nakar, E., & Piran, T. 2003, Nature, 426, 138

Granot, J., & Sari, R. 2002, ApJ, 568, 820

Groot, P. J. et al. 1998a, ApJ, 493, L27+

—. 1998b, ApJ, 502, L123+

Gunn, J. E. et al. 1998, AJ, 116, 3040

Haislip, J., Nysewander, M., Bayliss, M., Lacluyze, A., Reichart, D., Crain, J. A., & Foster, A. 2005a, GRB Coordinates Network, 4220, 1

Haislip, J. et al. 2006a, GRB Coordinates Network, 5033, 1

—. 2005b, GRB Coordinates Network, 3919, 1

Haislip, J., Reichart, D., Cypriano, E., Pizzaro, S., Lacluyze, A., Rhoads, J., & Figueredo, E. 2005c, GRB Coordinates Network, 3914, 1

—. 2005d, GRB Coordinates Network, 3913, 1

Haislip, J. B. et al. 2006b, Nature, 440, 181

Halpern, J. P., Kemp, J., Piran, T., & Bershady, M. A. 1999, ApJ, 517, L105

Hartmann, D. H., Greiner, J., & Briggs, M. S. 1995, A&A, 303, L65+

Henden, A. 2002, GRB Coordinates Network, 1753, 1

Hillenbrand, L. A., Foster, J. B., Persson, S. E., & Matthews, K. 2002, PASP, 114, 708

Hjorth, J. et al. 1999, GRB Coordinates Network, 219, 1

—. 2003, Nature, 423, 847

—. 2005, Nature, 437, 859

Holland, S. T. et al. 2004, AJ, 128, 1955

Huang, K. Y., Ip, W. H., Kinoshita, D., Urata, Y., Tamagawa, T., Qiu, Y., & Lou, Y. Q. 2005, GRB Coordinates Network, 3196, 1

Huang, Y. F., Cheng, K. S., & Gao, T. T. 2006, ApJ, 637, 873

Hurley, K. et al. 2005, GRB Coordinates Network, 4139, 1

in't Zand, J. J. M. et al. 2001, ApJ, 559, 710

Jakobsson, P., Hjorth, J., Fynbo, J. P. U., Watson, D., Pedersen, K., Björnsson, G., & Gorosabel, J. 2004, ApJ, 617, L21

Jelinek, M. et al. 2005, GRB Coordinates Network, 4227, 1

Jelinek, M., Kubanek, P., & Prouza, M. 2006, GRB Coordinates Network, 4976, 1

Jóhannesson, G., Björnsson, G., & Gudmundsson, E. H. 2006, ApJ, 647, 1238

Kahharov, B., Ibrahimov, M., Sharapov, D., Pozanenko, A., Rumyantsev, V., & Beskin, G. 2005, GRB Coordinates Network, 3261, 1

Kato, D., Nagata, T., & Kawai, N. 2003, GRB Coordinates Network, 1830, 1

Katz, J. I. 1994, ApJ, 422, 248

Katz, J. I., & Piran, T. 1997, ApJ, 490, 772

Kawai, N. et al. 2006, Nature, 440, 184

Kawai, N., Yamada, T., Kosugi, G., Hattori, T., & Aoki, K. 2005, GRB Coordinates Network, 3937, 1

Kinugasa, K., Kato, T., Yamaoka, H., & Torii, K. 2002, GRB Coordinates Network, 1749, 1

Kirschbrown, J., MacLeod, C., Reichart, D., Nysewander, M., Crain, A., Foster, A., & Lacluyze, A. 2005, GRB Coordinates Network, 3947, 1

Klebesadel, R. W., Strong, I. B., & Olson, R. A. 1973, ApJ, 182, L85+

Klose, S., Eisloeffel, J., Froebrich, D., Zeh, A., Richter, S., Hoegner, C., & Voss, H. 2002, GRB Coordinates Network, 1739, 1

Klotz, A., Boer, M., & Atteia, J. L. 2005a, GRB Coordinates Network, 3911, 1

—. 2005b, GRB Coordinates Network, 3917, 1

Kouveliotou, C., Meegan, C. A., Fishman, G. J., Bhat, N. P., Briggs, M. S.,

Koshut, T. M., Paciesas, W. S., & Pendleton, G. N. 1993, ApJ, 413, L101

Kulkarni, S. R. et al. 1998, Nature, 395, 663

Kumar, P., & Panaitescu, A. 2003, MNRAS, 346, 905

Kumar, P., & Piran, T. 2000a, ApJ, 535, 152

—. 2000b, ApJ, 532, 286

Lamb, D. Q., Barentine, J. C., Nysewander, M. C., Reichart, D. E., Schwartz, M.,

Laws, C., York, D. G., & McMillan, R. J. 2002a, GRB Coordinates Network, 1744, 1

Lamb, D. Q., Nysewander, M., Hearty, F., Chen, H.-W., & Reichart, D. E. 2006, GRB Coordinates Network, 5079, 1

Lamb, D. Q., Nysewander, M. C., Reichart, D. E., Barentine, J. C., Laws, C., York, D. G., & McMillan, R. J. 2002b, GRB Coordinates Network, 1765, 1

Lamb, D. Q., & Reichart, D. E. 2000, ApJ, 536, 1

Lamb, D. Q. et al. 2004, New Astronomy Review, 48, 423

Lazzati, D., Covino, S., & Ghisellini, G. 2002a, MNRAS, 330, 583

Lazzati, D., Rossi, E., Covino, S., Ghisellini, G., & Malesani, D. 2002b, Astronomy & Astrophysics, 396, L5

Ledoux, C., Vreeswijk, P., Smette, A., Jaunsen, A., & Kaufer, A. 2006, GRB Coordinates Network, 5237, 1

Lee, B. C. et al. 2001, ApJ, 561, 183

Levan, A. et al. 2006, ApJ, 647, 471

Levan, A., Merrill, M., Rol, E., dell'Antonio, I., Rhoads, J., & Fruchter, A. 2003, GRB Coordinates Network, 1818, 1

Li, W., Filippenko, A. V., Chornock, R., & Jha, S. 2002, GRB Coordinates Network, 1737, 1

—. 2003, ApJ, 586, L9

L´opez-Morales, M., & Clemens, J. C. 2004, PASP, 116, 22

Malesani, D., Fynbo, J., D'Avanzo, P., Covino, S., Fugazza, D., Jakobsson, P., & Vreeswijk, P. M. 2006a, GRB Coordinates Network, 5354, 1

Malesani, D., Jakobsson, P., Fynbo, J., Stritzinger, M., & Covino, S. 2006b, GRB Coordinates Network, 5350, 1

Mangano, V. et al. 2006a, GRB Coordinates Network, 5014, 1

Mangano, V., Troja, E., & Burrows, D. N. 2006b, GRB Coordinates Network, 5018, 1

Mao, S., & Paczynski, B. 1992, ApJ, 389, L13

Masetti, N., Palazzi, E., Pian, E., Covino, S., & Antonelli, L. A. 2003a, GRB Coordinates Network, 1823, 1

Masetti, N., Palazzi, E., Pian, E., Giro, E., Ortolani, S., Covino, S., & Antonelli, L. A. 2003b, GRB Coordinates Network, 1811, 1

Masetti, N. et al. 2001, Astronomy & Astrophysics, 374, 382

McLeod, B., Caldwell, N., Grav, T., Luhman, K., Garnavich, P., & Stanek, K. Z. 2002, GRB Coordinates Network, 1750, 1

Medvedev, M. V. 2006, ArXiv Astrophycs e-prints

Meegan, C. A., Fishman, G. J., Wilson, R. B., Horack, J. M., Brock, M. N., Paciesas, W. S., Pendleton, G. N., & Kouveliotou, C. 1992, Nature, 355, 143

Melandri, A. et al. 2006, GRB Coordinates Network, 4968, 1

Meszaros, P., & Rees, M. J. 1993, ApJ, 405, 278

Metzger, M. R., Cohen, J. G., Chaffee, F. H., Keck Observatory, W. M., & Blandford, R. D. 1997, IAU Circ., 6676, 3

Milne, P. A., Williams, G. G., Park, H. S., & Barthelmy, S. 2005, GRB Coordinates Network, 4218, 1

Mirabal, N., Halpern, J. P., & Tonnesen, S. 2005, GRB Coordinates Network, 4215, 1

Misra, K., Pandey, S. B., & Kamble, A. P. 2005, GRB Coordinates Network, 3202, 1

Misselt, K. A., Clayton, G. C., & Gordon, K. D. 1999, ApJ, 515, 128

Mizuno, T., Arai, Y., Yamagishi, H., Soyano, T., Urata, Y., Tamagawa, T., &

Huang, K. Y. 2005, GRB Coordinates Network, 3207, 1

Morgan, A. N., vanden Berk, D. E., Brown, P., & Evans, P. A. 2006, GRB Coordinates Network, 5553, 1

Morrison, R., & McCammon, D. 1983, ApJ, 270, 119

Nakagawa, Y. E. et al. 2006, PASJ, 58, L35

Nakar, E., Piran, T., & Granot, J. 2003, New Astronomy, 8, 495

Nemiroff, R. J. 1994, Comments on Astrophysics, 17, 189

Nysewander, M., Cypriano, E., Lacluyze, A., Bayliss, M., Reichart, D., Alvarez, A., & Ugarte, P. 2005a, GRB Coordinates Network, 4152, 1

Nysewander, M. et al. 2006a, GRB Coordinates Network, 4849, 1

Nysewander, M., & Haislip, J. 2006, GRB Coordinates Network, 5236, 1

Nysewander, M. et al. 2006b, GRB Coordinates Network, 4971, 1

Nysewander, M., Reichart, D., Ivarsen, K., Foster, A., Lacluyze, A., & Crain, J. A. 2006c, GRB Coordinates Network, 5545, 1

Nysewander, M. et al. 2006d, GRB Coordinates Network, 5344, 1

Nysewander, M., Reichart, D., Oliveira, A., Ugarte, P., & Alvarez, A. 2006e, GRB Coordinates Network, 4857, 1

Nysewander, M. C. et al. 2005b, ArXiv Astrophysics e-prints

Oates, S. R., Blustin, A. J., & Ziaeepour, H. Z. 2006, GRB Coordinates Network, 5243, 1

Odewahn, S. C. et al. 1997, IAUC Circ., 6735, 1

Ostriker, J. P., & Gnedin, N. Y. 1996, ApJ, 472, L63+

Paczynski, B. 1986, ApJ, 308, L43

Pagani, C., Morris, D., Racusin, J., Kennea, J., & Burrows, D. N. 2006, GRB Coordinates Network, 4959, 1

Page, K., Goad, M., & Beardmore, A. 2006a, GRB Coordinates Network, 5240, 1

Page, K. L., Goad, M. R., & Angelini, L. 2006b, GRB Coordinates Network, 4850, 1

Palmer, D. et al. 2006, GRB Coordinates Network, 5551, 1

Panaitescu, A., & Kumar, P. 2000, ApJ, 543, 66

—. 2004, MNRAS, 353, 511

Panaitescu, A., Mészáros, P., Gehrels, N., Burrows, D., & Nousek, J. 2006, MNRAS, 366, 1357

Pandey, S. B., Anupama, G. C., Sagar, R., Bhattacharya, D., Castro-Tirado, A. J., Sahu, D. K., Parihar, P., & Prabhu, T. P. 2003, A&A, 408, L21

Park, H. S., Williams, G., & Barthelmy, S. 2002, GRB Coordinates Network, 1736, 1

Patel, S., Kouveliotou, C., & Rol, E. 2005, GRB Coordinates Network, 4163, 1

Paciesas, W. S. 2004, Baltic Astronomy, 13, 187

Pei, Y. C. 1992, ApJ, 395, 130

Pellizza, L. J. et al. 2006, ArXiv Astrophysics e-prints

Perna, R., Lazzati, D., & Fiore, F. 2003, ApJ, 585, 775

Piranomonte, S. et al. 2005, GRB Coordinates Network, 3953, 1

Piro, L. et al. 2002, ApJ, 577, 680

Pravdo, S. H. et al. 1999, AJ, 117, 1616

Predehl, P., & Schmitt, J. H. M. M. 1995, A&A, 293, 889

Price, P. A. et al. 2002, ApJ, 572, L51

Price, P. A., Minezaki, T., Cowie, L. L., Kakazu, Y., & Yoshii, Y. 2006, GRB Coordinates Network, 4854, 1

Prilutskii, O. F., & Usov, V. V. 1975, Ap&SS, 34, 395

Prochaska, J. X., Bloom, J. S., Chen, H.-W., Foley, R. J., & Roth, K. 2005, GRB Coordinates Network, 3204, 1

Quimby, R., Fox, D., Hoeflich, P., Roman, B., & Wheeler, J. C. 2005, GRB Coordinates Network, 4221, 1

Racusin, J., Burrows, D., & Gehrels, N. 2005a, GRB Coordinates Network, 4141, 1

Racusin, J. et al. 2005b, GRB Coordinates Network, 4169, 1

Rees, M. J., & Meszaros, P. 1998, ApJ, 496, L1+

Reichart, D. 2005, GRB Coordinates Network, 3915, 1

Reichart, D. E. 1999, ApJ, 521, L111

—. 2001a, ApJ, 553, 235

—. 2001b, ArXiv Astrophysics e-prints

Reichart, D. E., & Price, P. A. 2002, ApJ, 565, 174

Reichart, D. E., & Yost, S. A. 2001, ArXiv Astrophysics e-prints

Rol, E. et al. 2006a, in American Institute of Physics Conference Series, ed. S. S. Holt, N. Gehrels, & J. A. Nousek, 1–1

Rol, E., Jakobsson, P., Tanvir, N., & Levan, A. 2006b, GRB Coordinates Network, 5555, 1

Rol, E., & Wijers, R. 2003, GRB Coordinates Network, 1864, 1

Rol, E., Wijers, R. A. M. J., Kouveliotou, C., Kaper, L., & Kaneko, Y. 2005, ApJ, 624, 868

Rutledge, R. E., & Fox, D. B. 2004, MNRAS, 350, 1288

Rykoff, E. S., Schaefer, B., Rujopakarn, W., Yuan, F., & Quimby, R. 2005, GRB Coordinates Network, 4211, 1

Sakamoto, T. et al. 2006, GRB Coordinates Network, 5349, 1

—. 2005, GRB Coordinates Network, 3189, 1

Sari, R., & Mészáros, P. 2000, ApJ, 535, L33

Sari, R., Piran, T., & Halpern, J. P. 1999, ApJ, 519, L17

Sari, R., Piran, T., & Narayan, R. 1998, ApJ, 497, L17+

Sato, G. et al. 2005, GRB Coordinates Network, 3951, 1

Schaefer, B. E. 2005, GRB Coordinates Network, 4132, 1

Schaefer, B. E., Rykoff, E. S., Rujopakarn, W., Yuan, F., Quimby, R., Alatalo, K., McKay, T. A., & Akerlof, C. 2005, GRB Coordinates Network, 4214, 1

Schlegel, D. J., Finkbeiner, D. P., & Davis, M. 1998, ApJ, 500, 525

Smith, D. A., Yost, S. A., & Rykoff, E. S. 2005a, GRB Coordinates Network, 3190, 1

Smith, I. A. et al. 2005b, Astronomy & Astrophysics, 439, 987

Smith, J. A. et al. 2002, AJ, 123, 2121

Soderberg, A. M. 2005, GRB Coordinates Network, 3234, 1

Sonoda, E., Maeno, S., Tokunaga, Y., & Yamauchi, M. 2005, GRB Coordinates Network, 4133, 1

Spergel, D. N. et al. 2003, ApJS, 148, 175

Stamatikos, M. et al. 2006, GRB Coordinates Network, 5339, 1

Stanek, K. Z. et al. 2003, ApJ, 591, L17

Stratta, G., Fiore, F., Antonelli, L. A., Piro, L., & De Pasquale, M. 2004, ApJ, 608, 846

Tagliaferri, G. et al. 2005, GRB Coordinates Network, 4213, 1

Tanaka, K. et al. 2005, GRB Coordinates Network, 4137, 1

Taylor, G. B., Bloom, J. S., Frail, D. A., Kulkarni, S. R., Djorgovski, S. G., & Jacoby, B. A. 2000, ApJ, 537, L17

Taylor, G. B., Frail, D. A., Kulkarni, S. R., Shepherd, D. S., Feroci, M., & Frontera, F. 1998, ApJ, 502, L115+

Torii, K. 2005a, GRB Coordinates Network, 3232, 1

—. 2005b, GRB Coordinates Network, 3943, 1

—. 2005c, GRB Coordinates Network, 4130, 1

Totani, T., Kawai, N., Kosugi, G., Aoki, K., Yamada, T., Iye, M., Ohta, K., & Hattori, T. 2006, Publications of the ASJ, 58, 485

Tueller, J. et al. 2006, GRB Coordinates Network, 5242, 1

Uemura, M. et al. 2004, PASJ, 56, 77

Valageas, P., & Silk, J. 1999, A&A, 347, 1

Valle, M. D. et al. 2003, GRB Coordinates Network, 1809, 1

van Paradijs, J. et al. 1997, Nature, 386, 686

Vrba, F., Luginbuhl, C., & Henden, A. 2003, GRB Coordinates Network, 1822, 1

Vreeswijk, P., Fruchter, A., Hjorth, J., & Kouveliotou, C. 2003, GRB Coordinates Network, 1785, 1

Vreeswijk, P., & Jaunsen, A. 2006, GRB Coordinates Network, 4974, 1

Wang, X., & Loeb, A. 2000, ApJ, 535, 788

Waxman, E. 1997, ApJ, 489, L33+

Waxman, E., & Draine, B. T. 2000, ApJ, 537, 796

Wei, D. M. 2003, Astronomy & Astrophysics, 402, L9

Wells, A. A. et al. 2005, GRB Coordinates Network, 3191, 1

White, R. S. 1993, Ap&SS, 208, 301

Wiersema, K. et al. 2005, GRB Coordinates Network, 3200, 1

Woosley, S. E. 1993, ApJ, 405, 273

Woosley, S. E., MacFadyen, A. I., & Heger, A. 2001, in Supernovae and Gamma-Ray Bursts: the Greatest Explosions since the Big Bang, ed. M. Livio, N. Panagia, & K. Sahu, 171–183

Wozniak, P. et al. 2002, GRB Coordinates Network, 1757, 1

Wozniak, P. R., Vestrand, W. T., Wren, J., White, R., & Evans, S. 2005, GRB Coordinates Network, 4239, 1

Wo´zniak, P. R., Vestrand, W. T., Wren, J. A., White, R. R., Evans, S. M., & Casperson, D. 2005, ApJ, 627, L13

York, D. G. et al. 2000, AJ, 120, 1579

Zhang, B., & M´esz´aros, P. 2002, ApJ, 566, 712

Ziaeepour, H. Z. et al. 2006, GRB Coordinates Network, 5233, 1